University of California

Santa Barbara

Structural Effects and Compositional Tuning in Magnetocalorics and Kagome Superconductors

A dissertation submitted in partial satisfaction

of the requirements for the degree

Doctor of Philosophy

in

Materials

by

Yuzki Mizutani Oey

Committee in charge:

Professor Ram Seshadri, Chair
Professor Stephen D. Wilson
Professor John Harter
Professor Trevor Hayton

December 2022

The Dissertation of Yuzki Mizutani Oey is approved.

Professor Stephen D. Wilson

Professor John Harter

Professor Trevor Hayton

Professor Ram Seshadri, Committee Chair

November 2022

Structural Effects and Compositional Tuning in Magnetocalorics and Kagome Superconductors

by

Yuzki Mizutani Oey

Acknowledgements

I would first like to thank my advisor, Ram Seshadri, for his support throughout my time at UC Santa Barbara. His door was always open to talk about the problems I was having (and I had many). I would also like to thank Stephen Wilson for taking me under his wing for the kagome project, as well as the rest of my committee. I am grateful to the staff of the MRL and CNSI for keeping everything running so smoothly and their help with various instruments.

I would like to thank the Seshadri group, both current and former members, and the Wilson group, whose labs and equipment I heavily used. My work presented here was made possible by my project mentors, Joshua Bocarsly, Joya Cooley, and Brenden Ortiz; as well as my wonderful collaborators from various institutions. The DFT needed for my projects were done by Daniil Kitchaev and Farnaz Kaboudvand and I am grateful for their expertise.

My time here would not have been nearly the same without Emily Morgan. From being roommates and doing everything together (including commuting, running, climbing), to being neighbors and office mates but still excessively exercising together, she was there to help me through our required classes, reminisce about New Jersey, listen to all of my complaints, give me advise, and gossip. We baked yummy pies and swooned over all of the cute fluffy pups we saw, and I will miss spending time with her.

Finally, I am grateful to everyone who provided me with emotional support, including Julia Zuo and Emily Foley; my wonderful friends from undergrad: Mimi, Lindy, and Avery; and all of my silly pups that I watched in the past couple of years.

Curriculum Vitæ

Yuzki Mizutani Oey

Education

2022	Ph.D. in Materials (expected) University of California, Santa Barbara
2019	A.B. in Chemistry Princeton University

Publications

12. L. Kautzsch, Y. M. Oey, H. Li, Z. Ren, B. R. Ortiz, R. Seshadri, J. Ruff, Z. Wang, I. Zeljkovic, and S. D. Wilson, "Incommensurate charge-stripe correlations in the kagome superconductor $CsV_3Sb_{5-x}Sn_x$," *submitted*.
11. H. Li, H. Zhao, B. R. Ortiz, **Y. M. Oey**, Z. Wang, S. D. Wilson, and I. Zeljkovic, "Emergence of unidirectional coherent quasiparticles from high-temperature rotational symmetry broken phase of AV_3Sb_5 kagome superconductors," *submitted*.
10. M. Kang, S. Fang, J. Yoo, B. R. Ortiz, **Y. M. Oey**, J. Choi, S. H. Ryu, J. Kim, C. Jozwiak, A. Bostwick, E. Rotenberg, E. Kaxiras, J. G. Checkelsky, S. D. Wilson, J. Park, and R. Comin, "Charge order landscape and competition with superconductivity in kagome metals," *accepted to Nature Materials*.
9. **Y. M. Oey**, F. Kaboudvand, B. R. Ortiz, R. Seshadri, and S. D. Wilson, "Tuning charge-density wave order and superconductivity in the kagome metals $KV_3Sb_{5-x}Sn_x$ and $RbV_3Sb_{5-x}Sn_x$," *Phys. Rev. Mater.* **6** (2022) 074802. DOI: 10.1103/PhysRevMaterials.6.074802
8. **Y. M. Oey**, B. R. Ortiz, F. Kaboudvand, J. Frassineti, E. Garcia, R. Cong, S. Sanna, V. Mitrovic, R. Seshadri, and S. D. Wilson, "Fermi level tuning and double-dome superconductivity in the kagome metals $CsV_3Sb_{5-x}Sn_x$," *Phys. Rev. Mater.* **6** (2022) L041801. DOI: 10.1103/PhysRevMaterials.6.L041801
7. R. Singha, F. Yuan, G. Cheng, T. H. Salters, **Y. M. Oey**, G. V. Villalpando, M. Jovanovic, N. Yao, and L. M. Schoop, "$TaCo_2Te_2$: An air-stable, high mobility Van der Waals material with probable magnetic order," *Adv. Funct. Mater.* (2021) 2108920. DOI: 10.1002/adfm.202108920
6. E. C. Schueller, **Y. M. Oey**, K. D. Miller, K. E. Wyckoff, R. Zhang, W. Zhang, S. D. Wilson, J. M. Rodinelli, and R. Seshadri, "AB_2X_6 compounds and the stabilization of trirutile oxides," *Inorg. Chem.* **60** (2021) 9224–9232. DOI: 10.1021/acs.inorgchem.1c01366
5. **Y. M. Oey**, D. A. Kitchaev, J. D. Bocarsly, E. C. Schueller, J. A. Cooley, and R. Seshadri, "Magnetocaloric behavior and magnetic ordering in MnPdGa," *Phys. Rev. Mater.* **5** (2021) 014414. DOI: 10.1103/PhysRevMaterials.5.014414

4. **Y. M. Oey**, J. D. Bocarsly, D. Mann, E. E. Levin, M. Shatruk, and R. Seshadri, "Structural changes upon magnetic ordering in magnetocaloric $AlFe_2B_2$," *Appl. Phys. Lett.* **116** (2020) 212403. DOI: 10.1063/5.0007266

3. **Y. M. Oey** and R. J. Cava, "The effective magnetic moments of Co^{2+} and Co^{3+} in $SrTiO_3$ investigated by temperature-dependent magnetic susceptibility," *MRS Bull.* **122** (2020) 110667. DOI: 10.1016/j.materresbull.2019.110667

2. W. Wang, K. Sun, **Y. M. Oey**, R. J. Cava, L. Wu, Y. Zhu, R. Yu, and J. Tao, "Smectic and nematic phase modulations and transitions under electron beam in $Tb_2Cu_{0.83}Pd_{0.17}O_4$," *Phys. Rev. Mat.* **3** (2019) 093601. DOI: 10.1103/PhysRevMaterials.3.093601

1. **Y. M. Oey**, J. E. Park, J. Tao, E. M. Carnicom, T. Kong, M. B. Sanders, and R. J. Cava, "Stabilizing the Tb-based 214 cuprate by partial Pd substitution," *J. Mater. Res.* **33** (2018) 1690–1697. DOI: 10.1557/jmr.2018.102

Abstract

Structural Effects and Compositional Tuning in Magnetocalorics and Kagome Superconductors

by

Yuzki Mizutani Oey

Understanding the impact of structure on observable magnetic and electronic properties is an important aspect in materials chemistry. These insights can be used to develop theoretical models and predict new compounds that may be of interest in a wide range of applications. To study these structure–property relationships, many techniques are typically used, including X–ray diffraction, energy–dispersive X–ray spectroscopy, microscopy, magnetization and transport measurements, and density functional theory calculations. A combination of these measurements and computations can give a clearer picture of the underlying mechanisms that link structure and property so closely.

Some materials exhibit a structural change concurrent with its magnetic ordering, and this magnetostructural coupling is proposed to enhance certain magnetic effects. This phenomenon has been explored as a potential route to discovering new materials that exhibit desirable effects, such as in magnetocaloric materials with applications in solid state refrigeration. One such material is $AlFe_2B_2$, which exhibits a large magnetocaloric effect that was previously not linked to its structure. Chapter 2 of this dissertation reports an in–depth variable temperature synchrotron X–ray diffraction study that establishes the importance of magnetostructural coupling in the magnetocaloric effect observed in $AlFe_2B_2$.

In other systems, substituting an element with an isovalent, similar sized element can have pronounced changes on the magnetic and electronic properties. Chapter 3 explores the newly established magnetocaloric MnPdGa and the differences between MnPdGa and MnPtGa. While MnPtGa is also a magnetocaloric that adopts the same crystal structure and is isovalent to MnPdGa, DFT calculations elucidate electronic differences in the two compounds, which may cause their different magnetocaloric performances.

Lastly, chapter 4 and appendix B contains a hole–doping study of the AV$_3$Sb$_5$ (A = K, Rb, and Cs) kagome superconductors which have a competing charge density wave order. With very careful and systematic Sn substitution on the Sb site, the superconducting and charge ordering critical temperatures are tuned, and the effects of hole–doping on A = K, Rb *vs.* A = Cs suggest that the different A site kagomes have subtle but important differences in their electronic structures. DFT calculations support this idea, and while the exact interaction mechanisms between the superconducting and charge density wave ordering phases in AV$_3$Sb$_5$ require further study, the results presented here show a strong structure–property dependence in AV$_3$Sb$_5$.

Contents

List of Figures

List of Tables

Chapter 1

Introduction

Magnetic materials have been of interest for thousands of years, and recently have gained popularity for their vast applications such as in medical and electronic devices and energy production and storage. For example, skyrmions are stable topological spin vortices and are attractive candidates for race–track memory technology.[1] Superconductors, which are perfect diamagnets that conduct electricity without energy loss, have been pursued and commercialized for decades as powerful electromagnets, sensitive particle detectors, and zero energy loss power cables. The list of magnetic materials and their applications goes on. Despite these promising materials that show extremely desirable properties, many phenomena like superconductivity are not fully utilized because their known materials are not within a reasonable working temperature or contain nonabundant and toxic elements.

The close relationship between the crystal structure of a material and its observable properties is well known. Different allotropes of carbon, such as graphite and diamond, show dramatically different physical properties. While it is sometimes easier and more obvious to track changes that correlate with large structural modifications, studying the

effects of subtle crystal structure changes is also crucial. Magnetostructural coupling describes the concurrent change in magnetic and structure phases and is an example of a tangible, measurable change in structure and property. This coupling has been suggested as the driving force in determining the magnitude of the magnetocaloric effect, a phenomenon that could be a more efficient and environmentally friendly refrigeration method than vapor compression. In other materials, carefully adjusting the composition or electron/hole content can have dramatic effects on electronic and magnetic properties, such as superconducting critical temperature or the loss of an electronic ordering phase. Understanding these relations between structure and property can allow us to engineering materials to achieve certain properties.

In this dissertation, two characterization techniques are heavily used: X–ray diffraction and magnetic measurements. Powder X–ray diffraction is performed on both the in–house X–ray diffractometer with CuKα radiation as well as at a synchrotron source. Magnetic measurements are performed on the Quantum Design Magnetic Property Measurement System (MPMS) and the Physical Property Measurement System (PPMS). The next sections will give a broad overview of X–ray diffraction and magnetism.

1.1 A broad introduction to X–ray diffraction

X–ray diffraction (XRD) is commonly used to gain structural information about a material, such as their space group, lattice parameters, and phase purity. It replies on the crystallinity of a material and can be done on a single crystal or a polycrystalline sample. In powder X–ray diffraction (pXRD), the average bulk structure is studied. The wavelengths of X–rays are similar to the atomic spacing of crystals, allowing the beam

to diffract in a meaningful way.

The main components of an X–ray diffractometer include the X–ray tube (filament, target, collimator), sample holder, and detector. A filament (often tungsten) is heated to produce electrons, which are then accelerated towards a target (often copper or molybdenum). The electrons must have energies that are higher than the energy of the desired X–rays. When the electrons hit the target, they get slowed down and lose energy. This energy is the background X–ray, or the braking radiation (Bremsstrahlung). In addition, characteristic X–rays are formed because the electrons are able to excite the inner shell electrons of the target material into another atomic shell. CuKα radiation is produced when an s–electron from the K-shell from copper is knocked out. This process leaves a hole in a low energy shell, and to compensate a conduction electron drops down and releases energy in the form of the characteristic X–ray. Heavier elements have higher characteristic X–rays; for example, molybdenum has a higher energy than copper. Copper is a common target material because it produces an X–ray with desirable wavelength of $\lambda = 1.54\,\text{Å}$.

When the X–ray beam hits the sample, constructive interference occurs when Bragg's law is satisfied: $n\lambda = 2d\sin\theta$. Here, the incident wavelength λ in n integer multiples is related to the angle θ between the incident rays and crystal surface for a certain spacing of atomic layers d. By moving two out of three of the incident beam, sample, or detector, a full range of 2θ angles can be scanned and visualized in a 2D plot of scattering intensity *vs* 2θ. In a polycrystalline sample, all orientations of the sample should be represented due to its random nature.

While Bragg's law determines the 2θ peak positions, the peak intensities are proportional to the square of the structure factor. The structure factor F_{hkl} takes into account the amplitude and phase of the diffracted beams and is defined as $F_{hkl} =$

$\sum_{n=1}^{N} f_n e^{-2\pi i(hx_n+ky_n+lz_n)}$ where the sum is over all n atoms in the unit cell, f_n is the scattering factor and x_n, y_n, and z_n are the coordinates of the nth atom.[2]

To obtain higher quality data, diffraction measurements can be obtained at synchrotron sources. Synchrotron X–rays are superior to laboratory sources due to their high intensity, collimation, and continuous spectral distribution. Electrons are accelerated to high energies and then injected into a circular storage ring (made up of many short straight sections), where they pass through various magnets. When the direction of the electrons is changed, energy is emitted in the form of X–rays. Insertion devices, or undulators, are located in the straight sections of the ring and consist of several small magnets. They force the electrons into an undulating path. The radiation produced from these devices is very focused, and the emitted photons are within a small energy range. The wavelength of the produced X–rays can be tuned by changing the distances between the magnets. Bending magnets are placed at the corners and help the electrons stay in their orbit around the storage ring, but as the straight path of electrons are bent by these magnets, X–rays are emitted at a wide and continuous range of wavelengths. This emission is much less focused than the X–rays produced by the insertion devices.

The X–rays produced by synchrotron sources have smaller wavelengths than Cu or Mo radiation, and this allows for much higher quality scattering measurements over a wider Q range, where $Q = \frac{4\pi sin(\theta)}{\lambda} = \frac{2\pi}{d}$. In addition, the shorter synchrotron wavelengths often eliminate fluorescence problems encountered when using laboratory X–ray diffractometers. The high flux and resolution of the beam additionally allows for more peaks to be seen and consequently indexed, including weaker background or secondary phase peaks that cannot be resolved using other sources. The high energy of a synchrotron beam can also reduce sample absorption, and other common problems

that arise from laboratory instruments are generally eliminated, including preferred orientation, surface absorption, and sample height discrepancies. Synchrotron X–ray studies are additionally useful in identifying secondary phases, temperature–dependent phase transitions, and oxidation states.[3, 4]

XRD data discussed here was analyzed using either Rietveld or Pawley fitting. The Rietveld method uses a least squares approach to fit a theoretical line profile to the measured profile. A starting model with crystallographic parameters such as elements in the material, unit cell size and atom positions is used. The calculations refine these crystallographic parameters as well as other variables, including background corrections, scale factors, and profile parameters to account for peak shapes and widths. Peak intensities are calculated from the structure factors (that are calculated from the model structure parameters).[5] Pawley refinements do not rely on the crystal structure and can be used as a starting point of a more sophisticated refinement. Every reflection in a Pawley fit is assumed to have a peak position dictated by the unit cell metric tensor parameters, peak widths determined by the peak width resolution function parameters, and a peak intensity parameter.[6]

1.2 A broad introduction to magnetism

Unpaired electrons on an ordered lattice can lead to various types of magnetic ordering. An electron has some total angular momentum, J, which is the sum of its total orbital angular momentum, L, and its total spin angular momentum, S: $J = L + S$. Spin-orbit coupling arises from the coupling of L and S and is typically much stronger in f electrons (such as lanthanides) than in $3d$ electrons (transition metals). For unpaired d electrons, a theoretical spin-only effective magnetic moment can be calculated

as $\mu_{eff} = \sqrt{n(n+2)}\mu_B = 2\sqrt{2S+1}\mu_B$.[7] Here, n is the number of unpaired d electrons and μ_B is the Bohr magneton. The Bohr magneton is the spin magnetic moment of a single electron and is defined as $\mu_B = \frac{eh}{4m_e\pi}$.[8] If there is an orbital contribution to the magnetic moment, as there is in lanthanides and some transition metals, the effective magnetic moment is calculated as

$$\mu_{eff} = g\sqrt{J(J+1)}\mu_B, \tag{1.1}$$

where g is the magnetomechanical ratio, or the Landé splitting factor, and is defined as $g = 1 + \frac{J(J+1)+S(S+1)-L(L-1)}{2J(J+1)}$. In many atoms, the external applied field can quench the orbital angular momentum and L goes to zero, so $g \approx 2$.

Neighboring moments interact with each other, and nearest neighbor interactions affect a spin's orientation. Dipolar and exchange interactions are responsible for magnetic long range order. Exchange interactions can be expressed through the following Hamiltonian:

$$H_i = -2\sum_j J_{ij} S_i \cdot S_j, \tag{1.2}$$

where S is the vector spin operator and J_{ij} is the exchange constant between spins i and j.[9] Electrons on neighboring atoms interact via direct exchange, but oftentimes the orbital overlap between adjacent atoms is inadequate and direct exchange is not the main factor for magnetic ordering. Indirect exchange, or superexchange, takes place between non-nearest neighbors and is mediated by a non-magnetic atom between the magnetic atoms. Finally, dipolar exchanges are usually too weak to detect at room temperature, but are sometimes important to consider at milliKelvin temperatures, especially in the $4f$ electron containing lanthanides and actinides.

The response of a material to an applied magnetic field is known as the magnetic

susceptibility, χ. It is a physically measurable quantity by sweeping temperature under a constant applied field, and is defined as the magnetization of a material, M, divided by the applied field strength, H: $\chi = \frac{M}{H}$. Diamagnetism, paramagnetism, ferromagnetism, antiferromagnetism, and ferrimagnetism are the five main types of magnetism and are distinguishable by their susceptibility behavior. All materials have paired core electrons and exhibit some level of diamagnetism, a type of weak magnetism that arises from unpaired electrons that do not have a net spin. Usually, diamagnetism can be ignored in materials that have some unpaired electrons because the magnetism from the unpaired electrons is much stronger. Paramagnetism originates from unpaired electrons that have spins pointing in random directions, and is characterized by a positive susceptibility. An external applied magnetic field can often induce the spins to align parallel to the field. At high temperatures the thermal energy contributes to the entropy of the spins, so even in the presence of a magnetic field, the spins are able to fluctuate, leading to a net zero moment. However, when the material is cooled in the presence of an applied field, its spins may line up with the magnetic field, depending on the temperature and field. The susceptibility increases in accordance with the Curie law, $\chi = \frac{C}{T}$, where C is the Curie constant defined as:

$$C = \frac{N_A \mu_B^2 p_{eff}^2}{3k_B} = \frac{p_{eff}^2}{8}, \tag{1.3}$$

where N_A is Avogadro's number, k_B is the Boltzmann constant, p_{eff} is the effective moment, and μ_B is the Bohr magneton.

As a paramagnetic material is cooled in the presence of a magnetic field, its spins may eventually order. The temperature at which this happens is known as either the Curie temperature (T_C) for ferromagnetic materials, or the Néel temperature (T_N) for antiferromagnetic and ferrimagnetic materials. Ferromagnetism occurs when the ex-

change constant J is positive, and all of the magnetic moments align in the same direction parallel to the applied field. The large coupling between spins leads to a positive moment proportional to the number of unpaired electrons in the material, and the susceptibility increases rapidly. In an antiferromagnet, the exchange constant J is negative, and the magnetic moments align antiparallel to one nearest neighbors. This alignment of spins causes the susceptibility to suddenly drop at T_{N}. Lastly, in a ferrimagnet, the spins are antiparallel much like in an antiferromagnet, but one direction is much more prominent than the other.

The collective interactions of magnetic moments cause deviations from the Curie law and can be modeled by the Curie-Weiss law,

$$\chi = \frac{C}{T - \theta_{CW}} + \chi_0, \tag{1.4}$$

where χ_0 is a magnetic correction factor that accounts for the diamagnetic and Pauli contributions and θ_{CW} is the Curie-Weiss temperature, an approximation of the ordering temperature. For paramagnetic materials, $\theta_{CW} = 0$, for ferromagnetic materials, $\theta_{CW} > 0$, and for antiferromagnetic materials, $\theta_{CW} < 0$. From the values obtained through fitting the Curie-Weiss law, the effective magnetic moment can be estimated via $\mu_{eff} \propto \sqrt{8C}$. Metals contain itinerant or delocalized electrons, so they exhibit Pauli paramagnetism in which the susceptibility is much smaller than the paramagnetism of a nonmetal. The susceptibility of a Pauli paramagnet cannot be completely described by the Curie-Weiss law and is instead dependent on the Fermi energy and the Fermi temperature. Although the contribution of Pauli paramagnetism to the susceptibility is difficult to determine, it is most effectively found by comparing susceptibilities extracted from electron spin resonance (ESR) and nuclear magnetic resonance (NMR).[10] This will not be discussed here.

Heat capacity measurements (C) are used to experimentally determine the changes in entropy and heat transfer when a material undergoes a magnetic ordering transition. Heat capacity is calculated as:

$$C = \left(\frac{dQ}{dT}\right) = T\left(\frac{\partial S}{\partial T}\right), \tag{1.5}$$

where dQ is the amount of heat given to the sample, and dT is the increase in temperature of the sample. The total entropy released over a temperature range can be calculated by integrating the heat capacity over temperature:

$$S(T) = \int_0^T \frac{C_P}{T} dT \tag{1.6}$$

As a material is cooled to zero Kelvin, its entropy reaches a constant value and is dependent on the number of available ground states. Entropy can be calculated from the number of microstates in a system in thermodynamic equilibrium using Boltzmann's principle as $S = R\ln(\Omega)$, where R is the ideal gas constant and Ω is the total number of microstates. Thus, when a pure crystalline material only has one ground state in which all of the magnetic spins assume a configuration so that the system has the lowest energy, the entropy at zero Kelvin is zero. Not all materials, however, have a singular ground state, and these materials are modeled using statistical mechanics. In a Heisenberg system, spins are treated as quantum particles and can point in three dimensions. As a result, $\Omega = J(J+1)$. The Heisenberg model is used for one, two, and three–dimensional systems, and accounts for nearest neighbor interactions. Additional interaction terms can be added to account for next-nearest neighbor interactions as well.[11] Conversely, the Ising model is used for one and two–dimensional systems. The moments are restricted to one of two possible spin states, up or down ($+1$ or -1)

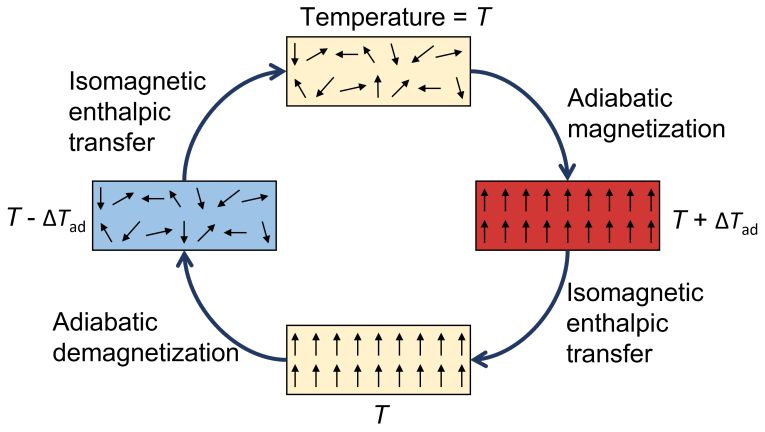

Figure 1.1: The magnetocaloric effect is analogous to vapor compression and cycles through adiabatic and isothermal magnetization and demagnetization to achieve a heat pump.

and only accounts for nearest neighbor interactions.[12]

1.3 The magnetocaloric effect as an environmentally friendly alternative to vapor compression

Magnetocalorics have recently gained popularity as environmentally safe and efficient refrigerants compared to materials used in traditional vapor compression.[13–15] The magnetocaloric effect was first observed by Emil Warburg in 1881, and in 1933 gadolinium sulfate was used to achieve temperatures below 1 K.[16] Gadolinium metal was discovered to be a room temperature magnetocaloric in 1976,[13, 17] allowing magnetic refrigeration to be feasible in practical settings, such as in refrigerators, air conditioners, and freezers. By using solid state magnetic refrigeration, better efficiency can be achieved while avoiding environmentally harmful liquid refrigerants such as CFCs. Recently, some progress to commercialize solid state refrigeration has been made,[18] but there is still a push to discover and understand more efficient

magnetocalorics composed of earth abundant and safe materials.

In a typical ferromagnet, application of a magnetic field near the Curie temperature causes the moments to partially align. If this magnetization is performed adiabatically, the lattice entropy increases to compensate the decreased entropy of the spins, raising the temperature of the material. Conversely, when the field is removed, the temperature decreases. This cycle is schematically represented in Figure 1.1. By alternating adiabatic and isothermal magnetization and demagnetization steps, a magnetic heat pump can be built in direct analogy to a conventional vapor-compression heat pump. The most common metric used to characterize the strength of a magnetocaloric is $\Delta S_M(T, H)$, which is given by

$$\Delta S_M(T, H) = \int_0^H (\partial M/\partial T)_{H'} dH' \tag{1.7}$$

and is the isothermal entropy change at temperature T with an applied magnetic field H. Generally, magnetocalorics are evaluated by the peak value of ΔS_M for a given applied field in gravimetric units $\mathrm{J\,kg^{-1}\,K^{-1}}$; however, for applications where weight is not as important, the volumetric units $\mathrm{mJ\,cm^{-3}\,K^{-1}}$ are perhaps of more interest.

ΔS_M, the isothermal magnetic entropy change, and ΔT_{ad}, the adiabatic temperature change upon magnetization, are two metrics that are important to consider when studying a magnetocaloric candidate. The maximum magnetocaloric effect in a ferromagnetic material is observed near the Curie temperature, and a working temperature further from T_C has a decreased effect. Therefore, materials such as gadolinium metal with a Curie temperature of 293 K are naively good candidates for room–temperature applications.

For practical use, a magnetocaloric should ideally function in a wide temperature

range, but this temperature range is not considered in the ΔS_M figure of merit.[19] Refrigerant capacity (RC) is often considered in addition to ΔS_M when comparing magnetocalorics with a second order magnetic transition near room temperature. RC is a measure of how much heat is transferred between hot and cold reservoirs, and is calculated as the area under the ΔS_M curve truncated at the full width at half maximum (FWHM).[15]

A computational proxy based on density functional theory-based electronic structure calculations (DFT), the magnetic deformation (Σ_M), has shown promise in predicting magnetocaloric performance in ferromagnets.[20, 21] Σ_M estimates the strength of magnetostructural coupling in a material by quantifying the amount of unit cell deformation between DFT-relaxed structures calculated with and without spin polarization. This metric correlates well with ΔS_M in a broad range of materials, including those with first-order magnetostructural transitions and those with continuous transitions.[20–23] Compounds with Σ_M greater than 1.5% indicate a promising candidate, meriting experimental study.

Chapter 2 will focus on $AlFe_2B_2$, a magnetocaloric with earth abundant materials that shows a second order phase transition and a large magnetocaloric effect. The origin of the large MCE in $AlFe_2B_2$ has been debated, as the MCE in continuous phase transition magnetocalorics is often attributed to saturation magnetization and $AlFe_2B_2$ does not necessarily have a large saturation magnetization. We show through careful temperature dependent synchrotron X–ray diffraction data that the large MCE in $AlFe_2B_2$ arises from magnetostructural coupling.[22]

Chapter 3 will focus on MnPdGa, a newly discovered magnetocaloric that magnetically orders right above room temperature. DFT predicts MnPdGa to be a good magnetocaloric with strong magnetostructural coupling. While we do not explore mag-

netostructural coupling in MnPdGa, we confirm its magnetocaloric properties and additionally compare its electronic structure to MnPtGa, another magnetocaloric with the same crystal structure.[24]

1.4 Superconductivity and charge density waves

In some materials, as one electron moves through a crystal (phonon) lattice, the lattice distorts and pulls another electron through, forming a Cooper pair. These pair of electrons have a lower energy than the Fermi energy and are therefore paired (or bound). According to the Bardeen–Cooper–Schrieffer (BCS) theory formulated in 1957, superconductivity is an ordering phase in which electrons pair up in Cooper pairs to reduce the energy of the system. Superconductivity can be detected in magnetism *vs.* temperature, resistivity (transport), and heat capacity measurements.

Superconductors are commonly characterized by being perfect diamagnets and showing the Meissner effect. When an external magnetic field is applied to a superconductor, circulating currents within the material oppose the applied magnetic field. This phenomenon is known as Lenz's law and leads to zero electrical resistance. This is measured in temperature dependent resistivity, where upon cooling, the material behaves as a conventional metal above T_C but at T_C the resistivity drops sharply to zero. The Meissner effect is the exclusion of an applied magnetic field in a superconductor but is distinct from perfect diamagnetism, since perfect diamagnetism arises from zero electrical resistance. Above T_C, the superconductor allows the externally applied field to penetrate and has a diamagnetic susceptibility, but below T_C the magnetic field is excluded from the sample. This leads to a sharp drop in susceptibility. T_C can be taken as the point at which the susceptibility diverges from ≈ 0, or the midpoint of

the drop in susceptibility. To understand how much of a sample is superconducting, the susceptibility can be plotted in volumetric units and a fully superconducting sample should show a minimum superconducting volume fraction (Meissner fraction) of $4\pi\chi_v \approx -1$. A superconducting fraction of $-1 < 4\pi\chi_v < 0$ indicates that the sample has a non-superconducting phase.

Charge density waves, in the most simple and conventional cases, can be explained with a 1-dimensional Peierls-like distortion, which can lower the energy of the system, similar to superconducting phases. In a 1D Peierls distortion, a lattice with evenly spaced atoms a with an unpaired electron forms a superstructure with lattice spacing $2a$. Creating a modulation in the lattice that leads to such a superstructure can open up an energy gap at E_F, and depending on the electron filling, electrons may spill down across the energy gap into the lower energy state. Similar phenomena occur in both symmetry breaking phases; the reorganization of electrons is strongly coupled to another degree of freedom, such as lattice vibrations.[25]

Magnetic susceptibility, temperature dependent resistivity, and heat capacity measurements can detect a charge ordering transition but cannot be used to specify the transition as a charge density wave (CDW) transition. Since CDWs involve the formation of a superstructure, additional structural studies such as scanning tunneling microscopy (STM) and single crystal diffraction can confirm the formation of a superstructure and differentiate the charge ordering transition as a CDW.

1.5 The kagome net as a structural motif in AV_3Sb_5

Crystal structures with a triangular motif often host interesting states. The kagome net as shown in Figure 1.2, comprised of triangles and hexagons, has been a pop-

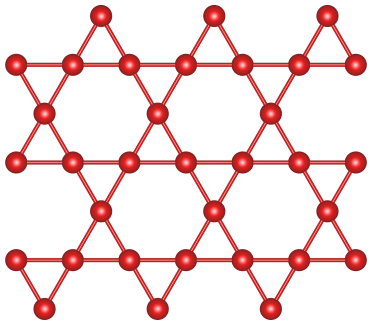

Figure 1.2: The kagome structure consists of corner shared hexagons and triangles, leading to a triangular motif.

ular structure of study since its discovery, with kagome insulators hosting magnetic frustration and uncommon ground states.[26, 27] Recent work in the kagome metals has focused on their inherently complex electronic structures, potential topologically nontrivial states, and exotic electronic transport. By nature, a kagome metal naturally supports an electronic structure that combines Dirac points and flat bands, increasing the possibility for substantial electronic instabilities and correlation effects. A wide array of instabilities have been predicted, ranging from bond density wave order,[28, 29] charge fractionalization,[30, 31] spin liquid states,[32] charge density waves (CDW),[33] and superconductivity.[28, 34]

Many of the unique electronic properties of the kagome metals can be distilled down to the intrinsic arrangement of van Hove singularities predicted within the essential framework of a kagome metal's electronic structure. For example, band fillings near $5/4$ electrons per band[28, 35–38] can lead to CDW order, and, in some limits, unconventional superconductivity. The recently discovered class of AV_3Sb_5 (A: K, Rb Cs) kagome metals [39] are potential realizations of this physical mechanism with each member exhibiting thermodynamic anomalies associated with CDW order [40–45] followed by the onset of superconductivity at lower temperatures.[42, 43, 46] This family of materials is nonmagnetic, which makes it an excellent candidate to study unconven-

tional superconductivity, and since its vanadium kagome layer is octahedrally coordinated and separated by antimony atoms, the kagome layers behave as a 2D structure. The CsV_3Sb_5 compound is currently the most well studied, due in part to the higher T_C, but also for the potentially more complex CDW.[47]

The CDW transition in AV_3Sb_5 was first detected by susceptibility, resistivity, and heat capacity measurements[39] and later confirmed via single crystal and STM data as well as DFT calculations.[48, 49] In CsV_3Sb_5, the structure exhibits a "breathing" mode below its CDW transition (94 K) between "Star of David" (SoD) or "Tri-Hexagonal" (TrH) distortions,[48] while similar results were confirmed in KV_3Sb_5.[49] Despite this similarity, the CsV_3Sb_5 CDW transition causes a structural distortion into a $2 \times 2 \times \times 4$ enlarged unit cell while A = K and Rb show a $2 \times 2 \times \times 2$ distortion.[48] These superstructures contain layers of kagome nets distorted into both star-of-David and tri-hexagonal structures and these layers are shown in Figure 1.3.[50] Therefore, it is suggested that the CDW transition in CsV_3Sb_5 is distinct from the transition in KV_3Sb_5 and RbV_3Sb_5.

While there are no local moments or magnetic correlations in AV_3Sb_5,[51] a large anomalous Hall effect emerges with the CDW order.[52, 53] Below the CDW transition, scanning tunneling microscopy [40] and calculations [38] have suggested that the CDW order parameter is chiral, which may break time–reversal symmetry and lead to a large Berry curvature. Recent quantum oscillation measurements have explored the reconstruction of the Fermi surface below the CDW order and have shown that the vanadium orbitals within the kagome planes in CsV_3Sb_5 play a crucial role in this reconstruction.[48]

The CDW instability in AV_3Sb_5 compounds seems to compete with superconductivity.[54, 55] The exact relationship between superconducting and

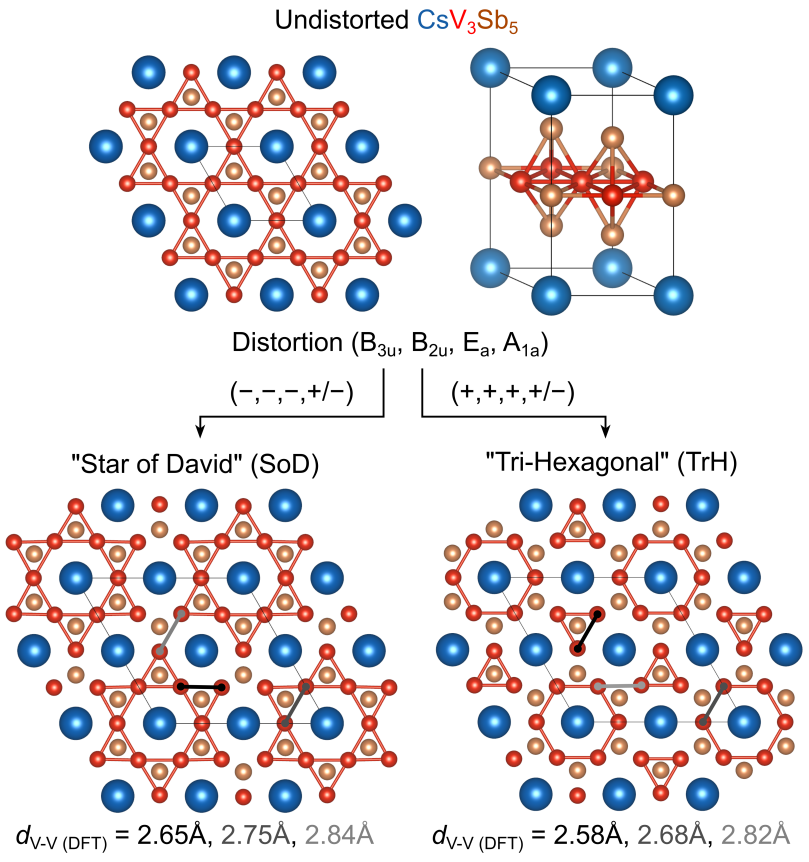

Figure 1.3: Figure reproduced from [48]. As CsV_3Sb_5 undergoes its CDW ordering transition, a superstructure comprising of alternating "Star of David" and "Tri-Hexagonal" layers form.

charge density wave states in many systems is still debated. In systems with CDW phases, unconventional superconductivity is often also observed. Pressure studies of CsV_3Sb_5 have shown interesting changes in T_C and T^*, where suppression of the CDW can lead to an enhancement of the T_C.[55] Similar results in pressure studies of the $NbSe_2$ family suggest a competition between superconducting and CDW states, and as pressure is increased, T_C increases as T^* decreases and eventually disappears.[56] However, sometimes superconductivity and CDW seem to cooperate or coexist, as observed by Freitas *et al.* in $2H-TaS_2$ and $2H-TaSe_2$.[57] Unlike the strongly reminiscent case of 2H-$NbSe_2$, CsV_3Sb_5 shows a complex phase diagram with a double dome of T_C with increasing pressure, with $T_C = 7\,\text{K}$ at $P_{c1} \approx 0.9\,\text{GPa}$ and $T_C = 8\,\text{K}$ at $P_{c2} \approx 2\,\text{GPa}$.[55]

Doping is another degree of freedom that is commonly applied to tune the relative stability of electronic instabilities. The electronic structure of the AV_3Sb_5 metals is rich, and with the multiple van Hove singularities within close proximity to the Fermi energy, doping is a feasible means to explore the instabilities intrinsic to each singularity. A recent study on oxidized thin flakes of CsV_3Sb_5 suggests that hole doping on the Sb site can enhance T_C while suppressing CDW order.[58] This effect of doping has been seen in other systems such as Cu_xTiSe_2, in which adding Cu to $TiSe_2$ creates a superconducting state while suppressing the CDW phase.[59]

In chapter 4, the effects of hole doping in AV_3Sb_5 for A = K, Rb, and Cs *via* partial substitution of Sn for Sb will be discussed. The solubility limit of Sn is dependent on A size, with $KV_3Sb_{5-x}Sn_x$ only accommodating $x = 0.25$ but $CsV_3Sb_{5-x}Sn_x$ allowing one Sb site to be substituted for Sn ($x = 1$). By analyzing the evolution of superconducting T_C and CDW T^* as a function of Sn-doping, the impacts of subtle band structure differences in K and Rb *vs.* Cs is clear.

1.6 Permissions and Attributions

1. The content of chapter 2 is reproduced from Y. M. Oey, J. D. Bocarsly, D. Mann, E. E. Levin, M. Shatruk, and R. Seshadri, "Structural changes upon magnetic ordering in magnetocaloric $AlFe_2B_2$", *Appl. Phys. Lett.* **116** (2020) 212403(1–5), with the permission of AIP Publishing.

2. The content of chapter 3 is reprinted with permission from Y. M. Oey, D. A. Kitchaev, J. D. Bocarsly, E. C. Schueller, J. A. Cooley, and R. Seshadri, "Magnetocaloric behavior and magnetic ordering in MnPdGa", *Phys. Rev. Mater.* **5** (2021) 014414(1–6). Copyright 2021 by the American Physical Society.

3. The content of chapter 4 is reprinted with permission from Y. M. Oey, B. R. Ortiz, F. Kaboudvand, J. Frassineti, E. Garcia, S. Sanna, V. Mitrovic, R. Seshadri, and S. D. Wilson, "Fermi level tuning and double-dome superconductivity in the kagome metals $CsV_3Sb_{5-x}Sn_x$", *Phys. Rev. Mater.* **6** (2022) L041801, copyright 2022 by the American Physical Society and Y. M. Oey, F. Kaboudvand, B. R. Ortiz, R. Seshadri, and S. D. Wilson, "Tuning charge-density wave order and superconductivity in the kagome metals $KV_3Sb_{5-x}Sn_x$ and $RbV_3Sb_{5-x}Sn_x$", *Phys. Rev. Mater.* **6** (2022) 074802, copyright 2022 by the American Physical Society.

Chapter 2

Structural changes upon magnetic ordering in magnetocaloric $AlFe_2B_2$

[1] With a Curie temperature just above room temperature, $AlFe_2B_2$ is a useful magnetocaloric material composed of earth-abundant elements. We employ temperature-dependent high resolution synchrotron X–ray diffraction to establish with high certainly that the paramagnetic to ferromagnetic transition in $AlFe_2B_2$ is second order, showing no discontinuity in lattice parameters or cell volume. Nevertheless, the lattice parameters undergo anisotropic changes across the transition with distinct differences in the thermal expansion coefficients. While the a and b lattice parameters show positive thermal expansion, c shows negative thermal expansion. We link these changes to the respective interatomic distances to determine the contribution of magnetism to the anisotropic structural evolution. The work underpins the possible role of magnetostructural coupling in driving the magnetocaloric effect in $AlFe_2B_2$.

[1] Reproduced from Y. M. Oey, J. D. Bocarsly, D. Mann, E. E. Levin, M. Shatruk, and R. Seshadri, "Structural changes upon magnetic ordering in magnetocaloric $AlFe_2B_2$", *Appl. Phys. Lett.* **116** (2020) 212403(1–5), with the permission of AIP Publishing.

2.1 Introduction

Gadolinium is often considered the prototypical magnetocaloric material (peak $\Delta S_M = 8\,\mathrm{J\,kg^{-1}\,K^{-1}}$; $\Delta T_{ad} = 7\,\mathrm{K}$) with its large spin moment and Curie temperature near room temperature.[13] To achieve these large ΔS_M values for gadolinium, however, a significant field of around 5 T must be applied, which is not practical for real household refrigerators and air conditioners. Gadolinium has a second–order continuous phase transition at its magnetic transition, but soon after the discovery of Gd as a magnetocaloric, it was realized that magnetocalorics with first–order discontinuous transitions can show a much larger MCE. Magnetostructural coupling can lead to a giant MCE in materials with first-order magnetostructural phase transitions, such as transition seen in $Gd_5Si_2Ge_2$ and FeRh, which involves a change in magnetic state accompanied by a simultaneous change in crystal structure.[14, 60, 61] In FeRh, a peak $\Delta S_M = 20\,\mathrm{J\,kg^{-1}\,K^{-1}}$ with $\Delta T_{ad} = 13\,\mathrm{K}$ can be achieved with an applied field of 2 T, but the magnetic transition is accompanied by such a large structural transition that the transition is irreversible.[61] On the other hand, while $Gd_5Si_2Ge_2$ (peak $\Delta S_M = 17\,\mathrm{J\,kg^{-1}\,K^{-1}}$; $\Delta T_{ad} = 15\,\mathrm{K}$ with applied field $H = 5\,\mathrm{T}$) also exhibits a first–order transition between an orthorhombic ferromagnetic state and a monoclinic paramagnetic state, the transition is reversible.[14, 60]

With the discovery of compounds such as $Gd_5Si_2Ge_2$ that exhibit large entropy and temperature changes, first–order transition magnetocaloric materials with magnetostructural coupling became a popular area of study. However, such transitions present challenges for use in practical devices. First–order transitions show hysteresis, resulting in losses, and discontinuous structural transitions may lead to mechanical degradation and rate limitations while cycling. Therefore, it is of great interest to find materials with second-order phase transitions that nevertheless show a large

MCE. In addition, a lot of these compounds contained rare earth elements, so the search for more environmentally-friendly and earth-abundant materials for large–scale applications started. Magnetically soft materials made with earth abundant elements with magnetic transitions near room temperature are therefore an attractive target in the search for practical magnetic refrigerants. While binary borides have high Curie temperatures,[23] more magnetically dilute borides can have transition temperatures closer to room temperature.[62, 63] Because the transition temperatures of these materials directly affect their practicality, many studies have investigated how the Curie temperature can be tuned in intermetallic compounds.[64–69]

It is often assumed that the magnitude of the MCE observed at a continuous phase transition is only controlled by the saturation magnetization, while the role of magnetostructural coupling in these materials has frequently been overlooked. However, the Bean and Rodbell model,[70] which is frequently used to understand giant MCE materials, shows that magnetostructural coupling can also greatly enhance the MCE in materials with second-order transitions.[71] This model is supported by experimental results from systems such as $LaFe_{13-x}Si_x$[72] and $Mn_xFe_{1.95-x}P_{0.5}Si_{0.5}$,[73] where chemical tuning controls the strength of magnetostructural coupling within both first– and second–order regimes. Similarly, it was found that MnB displays much larger magnetoelastic coupling than FeB, and consequently shows a peak value of $-\Delta S_M$ that is three times larger.[23]

A survey of magnetocalorics based on density functional theory calculations has established a broad correlation between magnetostructural coupling (approximated using magnetic deformation calculations) and MCE in materials with both first–order and continuous transitions.[20, 21, 68, 69] That is, strong magnetostructural coupling often indicates a first–order transition with large ΔS_M and thermal hysteresis.

As the magnetostructural coupling becomes weaker, ΔS_M also decreases and the corresponding material becomes less first–order, until eventually the predicted material is no longer first–order and instead has a continuous transition. This point at which the transition changes is the tricritical point, and materials with compositions near the tricritical point have continuous, hysteresis–free transitions but still have a reasonably large magnetocaloric effect.[74] $AlFe_2B_2$, among some other materials with strong magnetocaloric effects observed at continuous magnetic transitions, was predicted to display strong magnetostructural coupling when investigated experimentally.[20]

$AlFe_2B_2$ was first isolated and its crystal structure solved by Jeitschko in 1969.[75] Much more recently the compound has been identified as a strong magnetocaloric comprising earth-abundant elements with a paramagnetic to ferromagnetic transition at 285 K.[62] This transition temperature increases to 308 K when $AlFe_2B_2$ is grown using Ga flux, possibly due to an off stoichiometry of Al:Fe,[76] and the maximum $-\Delta S_M$ for $H = 5\,\mathrm{T}$ is around $8.0\,\mathrm{J\,kg^{-1}\,K^{-1}}$.[62, 77] For comparison, Gd also shows peak $-\Delta S_M$ of around $8\,\mathrm{J\,kg^{-1}\,K^{-1}}$ at $H = 5\,\mathrm{T}$. The large MCE in Gd is generally attributed to its high saturation magnetization of $254\,\mathrm{A\,m^2\,kg^{-1}}$.[78] $AlFe_2B_2$, on the other hand, displays a saturation magnetization of just $80.6\,\mathrm{A\,m^2\,kg^{-1}}$. Although there was initial confusion about the nature of the transition in $AlFe_2B_2$ with a report of a first order transition,[79] more recent studies utilizing neutron diffraction and temperature– and field–dependent magnetization have suggested that $AlFe_2B_2$ actually undergoes a continuous transition.[80–83] Therefore, it is of interest to understand how $AlFe_2B_2$ achieves such a large MCE comparable to that of Gd despite its modest saturation magnetization.

Here we show that a close look at the structural evolution of $AlFe_2B_2$ using high–resolution synchrotron X–ray diffraction data acquired at temperatures spanning the

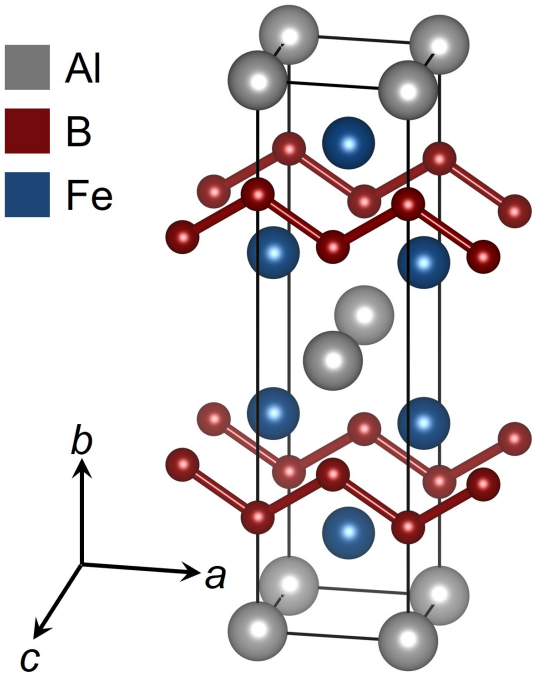

Figure 2.1: The crystal structure of $AlFe_2B_2$ consists of 1-D chains of B atoms running along the a axis separating Fe atoms. Al are at the corners and are C-centered. The $Cmmm$ structure of $AlFe_2B_2$ at 350 K as determined via high–resolution synchrotron X–ray diffraction has a = 2.93392(1) Å; b = 11.05318(2) Å; c = 2.87466(1) Å. Al at 2a, (0,0,0); Fe at 4j, (0,0.35397(1),0.5), and B at 4i, (0,0.2066(1),0). Parentheses on the last significant figure indicate calculated uncertainty.

Curie temperature reveals that while $AlFe_2B_2$ does not exhibit any discontinuities or structure-type changes across its magnetic transition temperature, it does display pronounced magnetoelastic effects. The magnetic transition is accompanied by anisotropic evolution of the a, b, and c lattice parameters as well as the atomic positions. Our findings for $AlFe_2B_2$ are supported by DFT calculations that show that magnetostructural coupling, and not just saturation magnetization, plays a key role in inducing a large MCE at second-order magnetic transitions. Other promising magnetocalorics displaying second–order phase transitions may also show magnetostructural coupling if they are studied more carefully using high–resolution synchrotron or neutron diffraction.

2.2 Methods

Samples of $AlFe_2B_2$ were prepared using Ga flux as previously reported.[62] A Quantum Design Physical Property Measurement System (PPMS) Dynacool with a vibrating sample magnetometer (VSM) was used to take temperature–dependent magnetization data at $H = 0.2\,\mathrm{T}$ between 5 K and 375 K. Field–dependent magnetization data were acquired at a temperature of 5 K in a field between $H = -5\,\mathrm{T}$ and 5 T. To determine the magnetic entropy change as a function of applied field, $\Delta S_M(H,T)$ was obtained from the appropriate Maxwell relation, using M *vs.* T measurements taken by sweeping temperature at fixed magnetic fields between $H = 0.1\,\mathrm{T}$ and 5 T and data were analyzed using the `magentro.py` code. [84] High–resolution synchrotron powder X–ray diffraction data were acquired at the Argonne National Laboratory, Advanced Photon Source (APS) on beamline 11–BM with an average wavelength of $\lambda = 0.414581\,\text{Å}$. Data at 200 K and 350 K were collected between $Q = 0.1\,\text{Å}^{-1}$ to $12\,\text{Å}^{-1}$. Temperature-dependent diffraction patterns were collected in the range $Q = 1.00\,\text{Å}^{-1}$

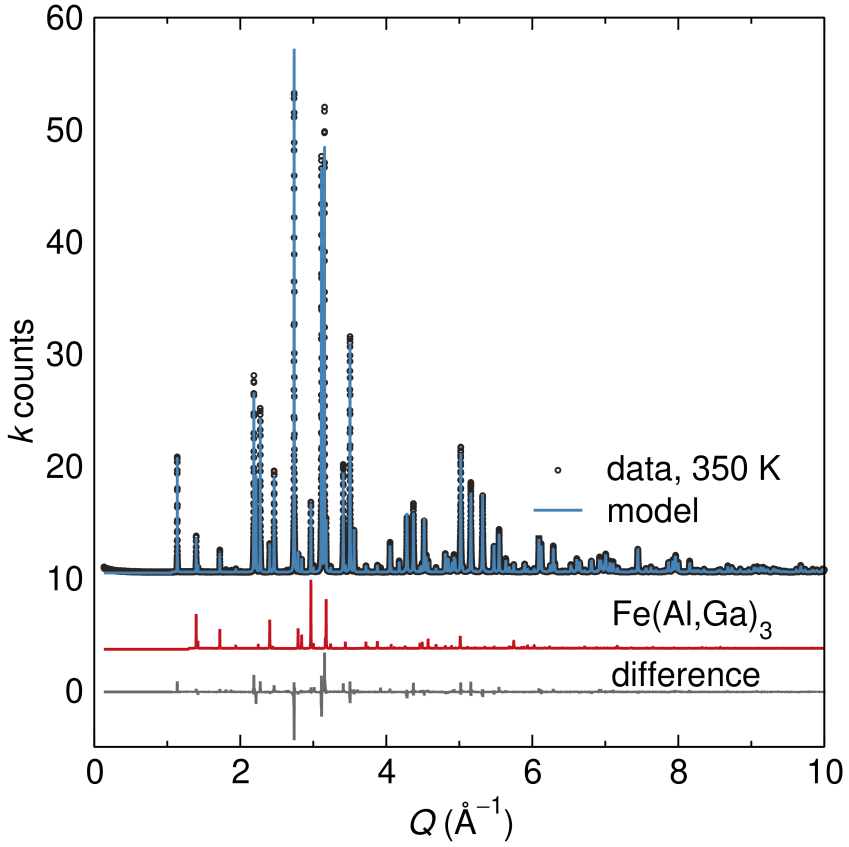

Figure 2.2: High–resolution synchrotron X–ray diffraction data acquired at $T = 350\,\mathrm{K}$ fit using Rietveld refinement with the two phases $AlFe_2B_2$ (space group $Cmmm$, #65) and $Fe(Al, Ga)_3$ (6.20(3) wt.%, space group $P4_2/mnm$, #136).

to $4.75\,\text{Å}^{-1}$ every 2.3 K as the sample was cooled from 336 K to 282 K, and every 0.5 K between 312 K and 300 K through the magnetic transition. Topas Academic[85] was used to refine the patterns using both sequential and parametric refinements.[86] Crystal structures were visualized using VESTA.[87]

2.3 Results and discussion

The $AlFe_2B_2$ structure shown in Figure 2.1 consists of B atoms spaced 1.75 Å apart arranged in 1-D zigzag chains along the a axis, with Fe atoms between these chains. Ri-

etveld refinement of the synchrotron data acquired at 350 K is shown in Fig. 2.2. Resulting refinement parameters and other information about data collection conditions are included in Appendix A. Due to the anisotropic nature of $AlFe_2B_2$,[88] the patterns were fit using the Stephens peak-shape function for an orthorhombic phase.[89] The main phase is orthorhombic $Cmmm$ $AlFe_2B_2$ as expected.[62] A tetragonal $P4_2/mnm$ secondary phase $Fe(Ga,Al)_3$[90] that was not detected on a laboratory X–ray diffractometer is observed in this synchrotron pattern as 6.20(3) wt.% of the sample, with Ga being incorporated from the flux. The refined composition of this phase is $FeGa_{1.828(8)}Al_{1.172(8)}$ with lattice parameters $a = b = 6.25621(2)$ Å and $c = 6.48051(4)$ Å. Because this secondary phase exists as a constant weight percent through all of the scans, we assume that it does not affect the structural transition that we observe in the main phase $AlFe_2B_2$. Moreover, $Fe(Ga,Al)_3$ is not magnetic,[90] so it does not contribute to the magnetism observed for this sample. The caption of Fig. 2.1 lists key structural details from the refinement of the $T = 350$ K data.

Figure 2.3(a) displays M *vs.* T under a constant field $H = 0.1$ T and confirms the reported ferromagnetic ordering at $T_C = 308$ K.[62] The inset of this figure shows M *vs.* H at $T = 5$ K. The saturation moment is 75.6 A m^{2}kg^{-1} for the sample, and with 6.20(3) wt.% non-magnetic secondary phase, the saturation moment for $AlFe_2B_2$ is 80.6 A m^2 kg^{-1} (2.31 μ_B f.u.$^{-1}$). This yields a magnetic moment of 1.16 μ_B Fe^{-1}, comparable to reported DFT calculated moments of 1.25 μ_B Fe^{-1} to 1.32 μ_B Fe^{-1}.[20, 62] Figure 2.3(b) displays the evolution of the magnetic entropy change under different applied maximum magnetic fields. A large $-\Delta S_M$ value of 8.0 J kg^{-1} K^{-1} was observed under $H = 5$ T, thereby confirming the previously reported magnetocaloric properties of $AlFe_2B_2$.[62] The relatively low saturation magnetization and yet significant ΔS_M indicate that saturation magnetization is not the only driving factor for the MCE in

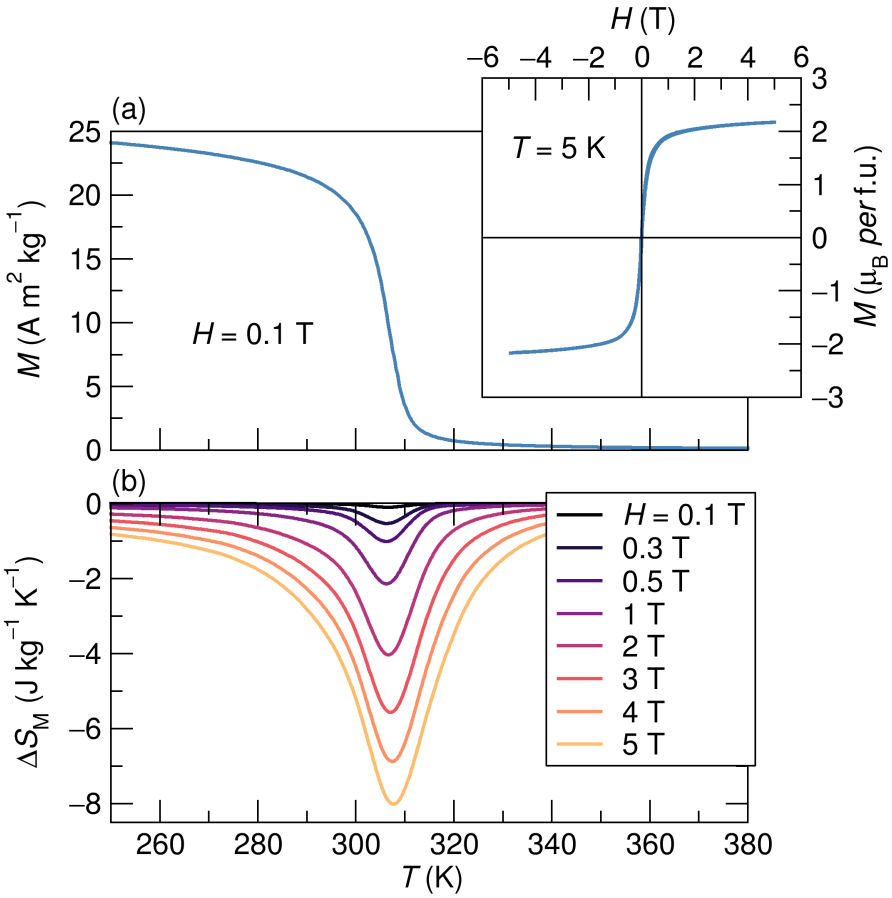

Figure 2.3: (a) Temperature dependent magnetization of $AlFe_2B_2$ acquired under a field of $H = 0.1\,\mathrm{T}$. Field dependent magnetization taken at $T = 5\,\mathrm{K}$ is shown in the inset. The adjusted saturation magnetization value for only $AlFe_2B_2$ at $T = 5\,\mathrm{K}$ and $H = 5\,\mathrm{T}$ is $80.6\,\mathrm{A\,m^2\,kg^{-1}}$ (emu $\mathrm{g^{-1}}$). (b) At a field of $H = 5\,\mathrm{T}$, $-\Delta S_M$ has a maximum value of $8.0\,\mathrm{J\,kg^{-1}\,K^{-1}}$.

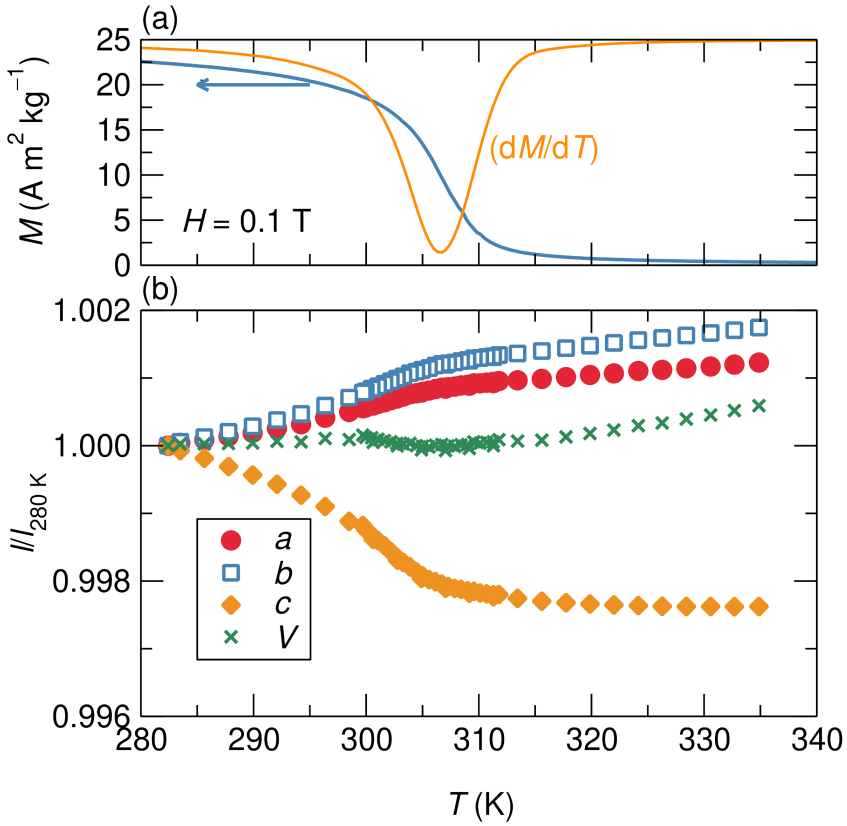

Figure 2.4: (a) Temperature–dependent magnetization taken at $H = 0.1\,\mathrm{T}$ with its respective derivative (peaking at 308 K) is compared with the (b) evolution of scaled lattice parameters a, b, and c, and unit cell volume as a function of temperature. The values in (b) are normalized by their respective values at $T = 280\,\mathrm{K}$. a and b display positive thermal expansion in the temperature range displayed, while c displays large negative thermal expansion.

$AlFe_2B_2$.

To investigate how structure evolves as a function of temperature, parametric Rietveld refinements were performed on variable–temperature synchrotron X–ray diffraction data. Fig. 2.4(b) displays normalized lattice parameters as a function of temperature, and a and b show positive thermal expansion while c shows considerable negative thermal expansion. All three lattice parameters show non-linear changes without any discontinuities, indicative of a second order phase transition. The sharpest change in these parameters occurs at the magnetic transition temperature, where the lattice pa-

rameters either increase or decrease by about 0.1% to 0.2% between 310 K and 280 K. The unit cell volume shows overall slight thermal expansion, but right below the T_C between 300 K and 308 K there is a slight contraction, leading to very little overall change. This is reminiscent of the Invar effect in which there is almost zero volume change with temperature after the onset of magnetization.[91] Although a 0.1% to 0.2% change in lattice parameter may seem small, these changes are many times stronger than the magnetostriction commonly observed in ferromagnetic materials,[92] including Gd.[93] These changes are, however, comparable to those seen in MnB, which has been found to derive a strong MCE from its magnetostructural coupling.[23]

It is interesting to compare these lattice parameter changes to the results of the DFT magnetic deformation study reported previously.[20] In the previous study, DFT structural optimizations with and without spin polarization were performed to estimate the effect that magnetism plays on the structure. For $AlFe_2B_2$, upon the introduction of spin polarization, the a, b, and c lattice parameters changed by –0.8%, –2.6%, and 5.6%, respectively. The changes upon magnetic ordering in the experimental lattice parameters are far smaller (as usual), but mirror these signs and relative magnitudes remarkably well, with the largest increase in lattice parameter seen in the c axis and smaller negative changes seen in the b and a axes. This is interesting because non spin–polarized DFT is not, in general, a good approximation for the high–temperature paramagnetic state as it does not consider the effect of local magnetic moments. The strong correspondence between experiment and calculation seen here may be due to the fact that the magnetism in $AlFe_2B_2$ shows substantially itinerant character.[81]

Interatomic distances (Fig. 2.5) show concomitant anisotropic evolution with temperature due to a combination of the lattice parameters and internal atomic coordinates. Most notably, the Fe–Fe distance along the b axis between adjacent unit cells

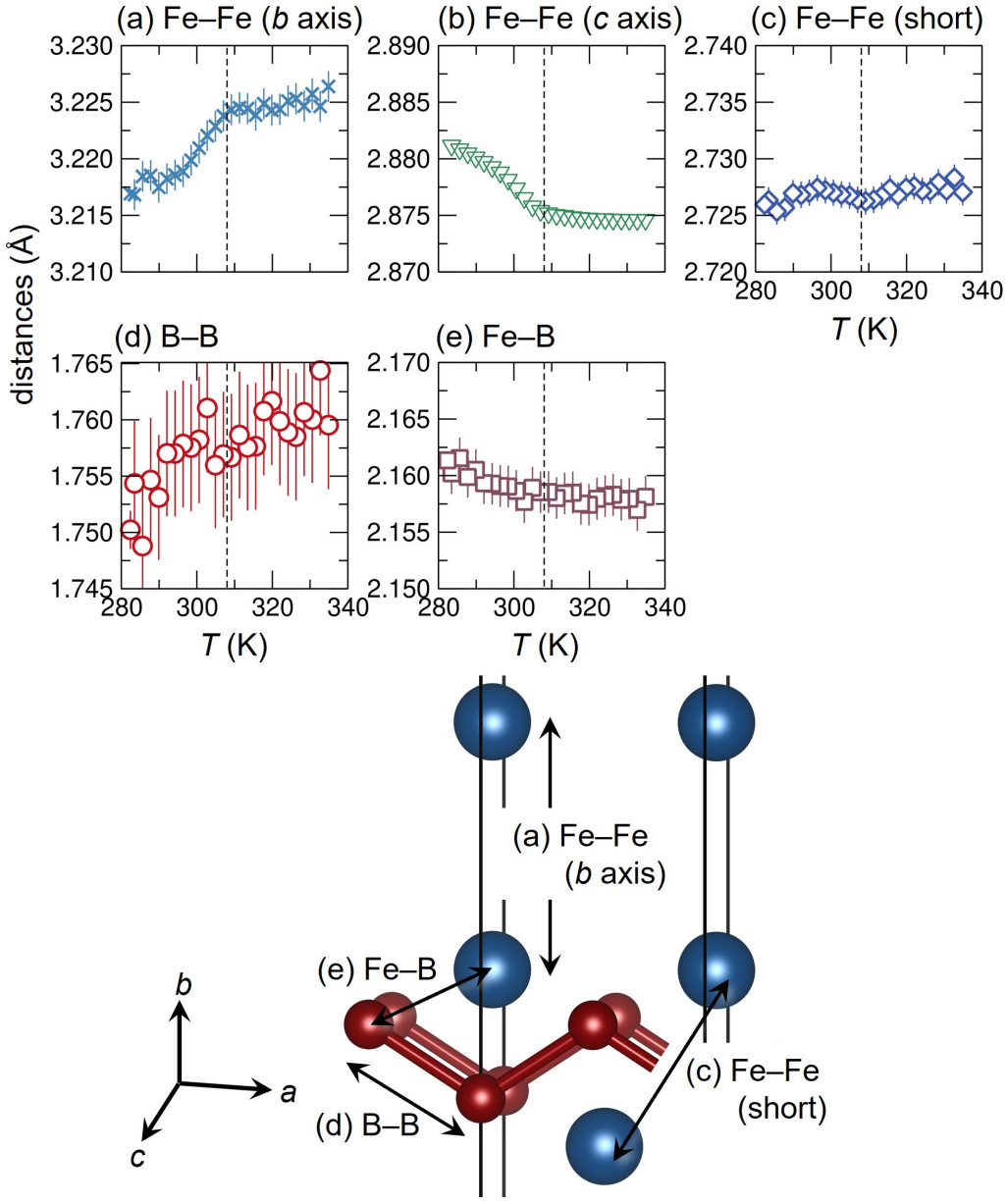

Figure 2.5: Evolution of atom–atom distances across the Curie temperature of T_C = 308 K (indicated as a dashed vertical line). (a) The Fe–Fe distances along the b axis show positive thermal expansion until the transition temperature, whereupon the rate of expansion displays a distinct decrease. (b) Between unit cells along the c direction, Fe atoms are bonded and show the greatest change in the slope. (c) The shortest Fe–Fe distance remains largely constant over this temperature range, suggesting that the competing lattice expansion in the b direction and contraction in the c direction almost balance out for these pairs of atoms. Neither the (d) B–B bonds nor the (e) closest Fe–B distances change very much. For clarity, all of the panels (a) through (e) have the same ordinate range of 0.02 Å; the distances discussed in the panels are related to the crystal structure on the right.

has pronounced positive thermal expansion from about 3.217 Å to 3.226 Å (Fig. 2.5a). However, this expansion is not as smooth as the b parameter shown in Fig. 2.4, suggesting that the cell may not be uniformly expanding. Meanwhile, the Fe–Fe distance along the c axis, which is equivalent to the c lattice parameter, shows the opposite effect (Fig. 2.5b). The shortest Fe–Fe contact, which lies in the ab plane, shows only very small changes, but an anomaly at the magnetic transition temperature can be clearly resolved (Fig. 2.5c). The B–B bonds connecting adjacent B atoms show the largest fractional change across the Curie temperature, with positive thermal expansion from about 1.75 Å to 1.76 Å (around 0.5%) between 280 K and 340 K (Fig. 2.5d), while the shortest Fe–B interaction shows slight negative thermal expansion, indicative of the competing forces of the a parameter positive expansion and c parameter negative expansion (Fig. 2.5e). Based on these results, we can conclude that magnetic order is accompanied by a strengthening of the B–B bonding and the Fe–Fe bonding along the b axis at the expense of weakening Fe–Fe bonding along the c axis and the Fe–B bonding.

2.4 Conclusion

Despite the modest saturation magnetization in $AlFe_2B_2$, the material shows a significant magnetocaloric effect comparable to that of Gd metal. Here, we propose that this effect is driven by magnetostructural coupling, which we observe through high–resolution temperature-dependent synchrotron studies. Given that $AlFe_2B_2$ has quite a large $-\Delta S_M$ and pronounced magnetostructural coupling, but shows no hysteresis, it may sit close to a tricritical point between first- and second-order magnetic transitions.[74] In this way, $AlFe_2B_2$ derives enhanced magnetocaloric properties from magnetostructural interaction without the practical downsides associated with first-

order transitions. Our results suggest that the large MCE seen in other materials with continuous transitions may also be attributed to magnetostructural coupling instead of purely to saturation magnetization. Furthermore, strategies to control the strength of magnetostructural coupling in materials with continuous transitions, such as by chemical substitutions, are expected to be powerful tools to optimize the magnetocaloric effect.

Chapter 3

Magnetocaloric behavior and magnetic ordering in MnPdGa

3.1 Abstract

[1] MnPdGa, a compound crystallizing in the Ni_2In structure, is a material displaying magnetic ordering near room temperature and is a potential ambient-temperature magnetocaloric. Screening based on electronic structure calculations suggest that MnPdGa may exhibit a high magnetocaloric figure of merit due to its strong magnetostructural coupling. Here we report the preparation of MnPdGa and employ high–resolution synchrotron X–ray diffraction to confirm its hexagonal Ni_2In–type structure. The zero-field ground state is shown to be a conical spin-wave state, defined by a long-range modulation of the conventional conical antiferromagnet structure. Near the Curie temperature, the measurements carried out here coupled with electronic structure cal-

[1] Reprinted with permission from Y. M. Oey, D. A. Kitchaev, J. D. Bocarsly, E. C. Schueller, J. A. Cooley, and R. Seshadri, "Magnetocaloric behavior and magnetic ordering in MnPdGa", *Phys. Rev. Mater.* **5** (2021) 014414(1–-6).

culations suggest that a fully ferromagnetic state can form at elevated temperatures under an applied field. A peak magnetocaloric entropy change $\Delta S_M = -3.54\,\mathrm{J\,kg^{-1}\,K^{-1}}$ ($30.1\,\mathrm{mJ\,cm^{-3}\,K^{-1}}$) is measured at $T_C = 315\,\mathrm{K}$ at an applied field $H = 5\,\mathrm{T}$. The exchange-driven, non-trivial magnetic structure found in MnPdGa is compared with the somewhat better studied MnPtGa on the basis of electronic structure calculations.

3.2 Introduction

MnPdGa was first reported in 2003 by Shiraishi and Hori and crystallizes in the Ni_2In–type hexagonal crystal structure, with Mn occupying the $2a$, Pd occupying $2d$, and Ga occupying $2c$ sites.[94] Neutron diffraction determined that MnPdGa is a ferromagnet with the moments pointing along the c axis.[94] The Curie temperature was found to be around 325 K, but at around 150 K, a second magnetic transition is observed, in which the ferromagnetic (FM) moments tilt away from the c axis to form a canted antiferromagnetic (AFM) structure with a reduced net moment. A more recent study from 2019 using Lorentz TEM and magnetic measurements suggested that this material may also host biskyrmion phases up to fields of 1.2 T.[95]

However, MnPdGa has not been very well investigated, and has limited magnetic and electronic data reported. An isostructural compound, MnPtGa, has recently been shown to be a magnetocaloric with interesting noncollinear magnetism.[92] MnPtGa has a DFT calculated $\Sigma_M = 2.4\%$ while MnPdGa has a $\Sigma_M = 2.8\%$, suggesting that MnPdGa could be expected to display significant magnetostructural coupling and may be promising for study as a magnetocaloric.

Here we explore the magnetocaloric response in MnPdGa prepared by arc–melting and characterized using high–resolution synchrotron data to confirm the Ni_2In–type

hexagonal crystal structure, previously proposed on the basis of powder X–ray and neutron diffraction. We find a magnetocaloric response of $\Delta S_M = -3.54\,\mathrm{J\,kg^{-1}\,K^{-1}}$ ($-30.1\,\mathrm{mJ\,cm^{-3}\,K^{-1}}$) for an applied field $H = 5\,\mathrm{T}$ near $T_C = 315\,\mathrm{K}$. While these values are somewhat smaller than anticipated from the computed Σ_M proxy, a significant refrigerant capacity of $224.6\,\mathrm{J\,kg^{-1}}$ was observed. We show that the origin of the reduced magnetocaloric effect as compared to the prediction from ΔS_M is non–collinear magnetic order which has an AFM component in addition to the FM moment. This effect is analogous to the behavior seen in MnPtGa,[92] although the size of the AFM component and reduction in magnetocaloric response is less pronounced in MnPdGa. Finally, we use electronic structure calculations to show that despite the similarities between MnPdGa and MnPtGa, subtle differences in the Mn spin-spin exchange interactions driven by the Pd/Pt substitution lead to substantial differences in the macroscopic magnetic moment, long-range magnetic order, and ultimately magnetocaloric performance.

3.3 Methods

Polycrystalline ingots of MnPdGa were prepared by arc–melting and furnace annealing elemental Mn (Alfa Aesar, 99.95%), Pd powder (Alfa Aesar, 99.95%), and Ga buttons (Alfa Aesar, 99.9999%) in 0.5 g batches. Pieces of Mn were cleaned by sealing in an evacuated fused silica tube and annealing at 1273 K overnight before use. About 0.010 g excess Mn was used to account for Mn loss *via* vaporization during arc melting. Cleaned Mn chips were ground into a powder and mixed thoroughly with a stoichiometric quantity of Pd powder, and the mixture was pressed into a 6 mm diameter pellet at 2 metric tons *per* $0.317\,\mathrm{cm^2}$. This pellet was arc–melted with Ga in an

Ar atmosphere, and the ingot was flipped over and re–melted twice to ensure homogeneity. The resulting ingot was sealed in an evacuated fused silica tube (7 mm inner diameter) backfilled with 10 psi of Ar and annealed at 1073 K for 5 days. The sample was quenched in water.

High–resolution synchrotron powder X–ray data were acquired through the mail–in program at the Argonne National Laboratory, Advanced Photon Source (APS) on beamline 11–BM with an average wavelength of $\lambda = 0.457913$ Å. The ingots of sample were crushed into powder and packed in a kapton capillary (inner diameter 0.8 mm). Data at room temperature (295 K) were acquired between $Q = 1.0$ Å^{-1} to 11.4 Å^{-1} with a sample acquisition time of 42 minutes. Topas Academic[85] was used to refine the patterns,[86] and crystal structures were visualized using VESTA.[87] For composition analysis, 50 mg of powder sample was pressed into a 6 mm diameter pellet and three 0.5 mm diameter points on the pellet surface were analyzed using a Rigaku ZSX Primus VI wavelength dispersive X–ray fluorescence (XRF) instrument.

A Quantum Design Superconducting Quantum Interface Device (SQUID) Magnetic Property Measurement System (MPMS) with a vibrating sample magnetometer (VSM) was used to take magnetization data on a 5.31 mg piece of sample that was placed into a plastic sample holder and loaded into a brass rod sample holder. Temperature–dependent magnetization data were acquired under a field of $H = 0.1$ T between 10 K and 350 K, under both zero–field cooled and field–cooled conditions. A magnetization *vs.* field hysteresis loop was acquired at 10 K in a field between 5 T and -5 T. To determine the magnetic entropy change as a function of applied field, $\Delta S_M(H,T)$ was obtained using the Maxwell relation $(\partial M/\partial T)_H = (\partial S/\partial H)_T$, using M *vs.* T measurements taken by sweeping temperature at 8 fixed magnetic fields between $H = 0.1$ T and 5 T. The data were analyzed using the `magentro.py` code.[84]

Electronic structure calculations on MnPdGa and MnPtGa were performed using density functional theory, as implemented in the Vienna *Ab initio* Simulation Package (VASP)[96] with projector augmented wave (PAW) pseudopotentials[97, 98] within the Perdew–Burke–Ernzerhof (PBE) generalized gradient approximation (GGA).[99] The hexagonal unit cell of MnPdGa was first relaxed in a non spin–polarized and spin–polarized FM calculations with force convergence of 0.001 eV Å^{-1} without spin–orbit coupling. Electronic densities of states (DOS) for each case were calculated for k–point grids of 10×10×8 and energy convergence criteria of 10^{-5} eV per cell. Calculations for the canted magnetic structures of MnPdGa and MnPtGa were performed within the orthohexagonal cell, increasing the convergence threshold to 10^{-7} eV per cell. In these calculations, the moment directions were constrained to various canting angles between 0° (collinear ferromagnetism) and 90° (collinear antiferromagnetism). No constraints were placed on the moment magnitudes. Spin–wave calculations were performed using the generalized Bloch's theorem approach to implicitly represent the incommensurate spin structure. Because this implicit representation is not applicable for spin–orbit coupling, we report all energies without including spin-orbit effects. However, we confirm that spin–orbit coupling leads to negligible changes in energy compared to the scale of the energy profile of the canted AFM phase or the spin-wave dispersion relation.

3.4 Results and discussion

Compositional analysis on the sample using XRF revealed an average composition of $Mn_{1.02(2)}Pd_{1.01(2)}Ga_{0.963(3)}$ (standard deviations denoted in parentheses), confirming that the sample is very near its stoichiometric formula. MnPdGa has been previously

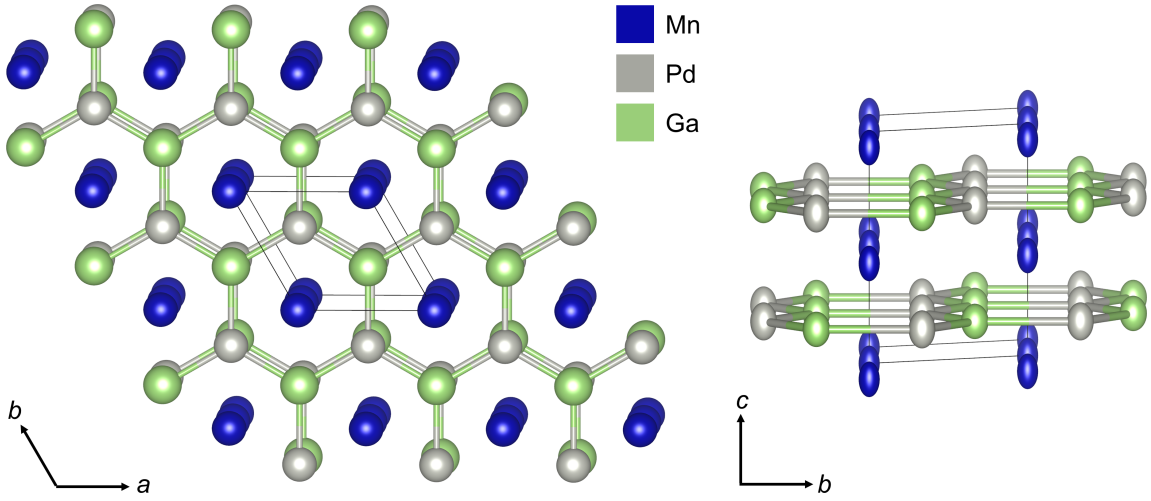

Figure 3.1: MnPdGa crystallizes in the hexagonal $P6_3/mmc$ (no. 194) space group. Looking down the c axis, the Pd and Ga make honeycomb net layers in the ab plane, with Mn atoms centered between the honeycomb layers. As seen looking down the a axis, the honeycomb layers alternate with layers of Mn on a triangular net. The atoms in this view are represented with displacement ellipsoids refined from the synchrotron diffraction data shown at 95% probability.

reported to form a Ni_2In-type hexagonal $P6_3/mmc$ (no. 194) structure as shown in Figure 3.1.[94, 95] Pd (Wyckoff site 2d) and Ga (Wyckoff site 2c) form honeycomb layers in the ab plane that are offset by $1/3$ of the unit cell. The view down the a axis shows that the Pd–Ga substructure alternate with layers of Mn (Wyckoff site 2a) in the c direction.

Figure 3.2 shows synchrotron diffraction pattern acquired at 295 K, along with a Rietveld fit to the Ni_2In structure type (space group $P6_3/mmc$). The pattern was fit using the Stephens peak-shape function,[89] indicating some anisotropic stain broadening, which is resolvable due to the very high resolution of the synchrotron diffractometer. In addition, some of the peaks show hkl–dependent asymmetry, which was addressed by refining the appropriate asymmetry parameters based on spherical harmonics with three nonzero terms. From the obtained fit, it is clear that all of the peaks in MnPdGa match with the reported Ni_2In structure ($P6_3/mmc$), with no evidence of space group

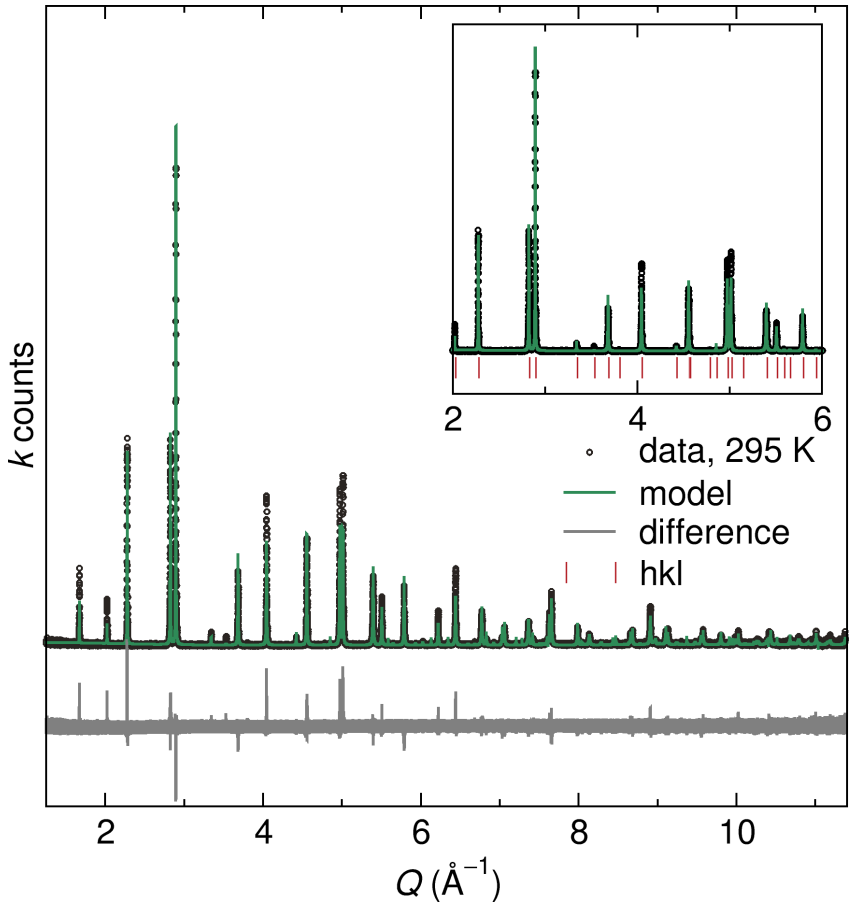

Figure 3.2: High–resolution synchrotron X–ray diffraction data acquired at $T = 295\,\mathrm{K}$ fit using Rietveld refinement between $Q = 1.25\,\text{Å}^{-1}$ to $11.4\,\text{Å}^{-1}$. MnPdGa crystallizes in the hexagonal $P6_3/mmc$ (No. 194) space group with cell parameters $a = b = 4.34263(3)\,\text{Å}$ and $c = 5.51951(5)\,\text{Å}$ and a volume of $90.147(1)\,\text{Å}^3$. The inset shows hkl positions calculated from $P6_3/mmc$, which line up with all observed peaks.

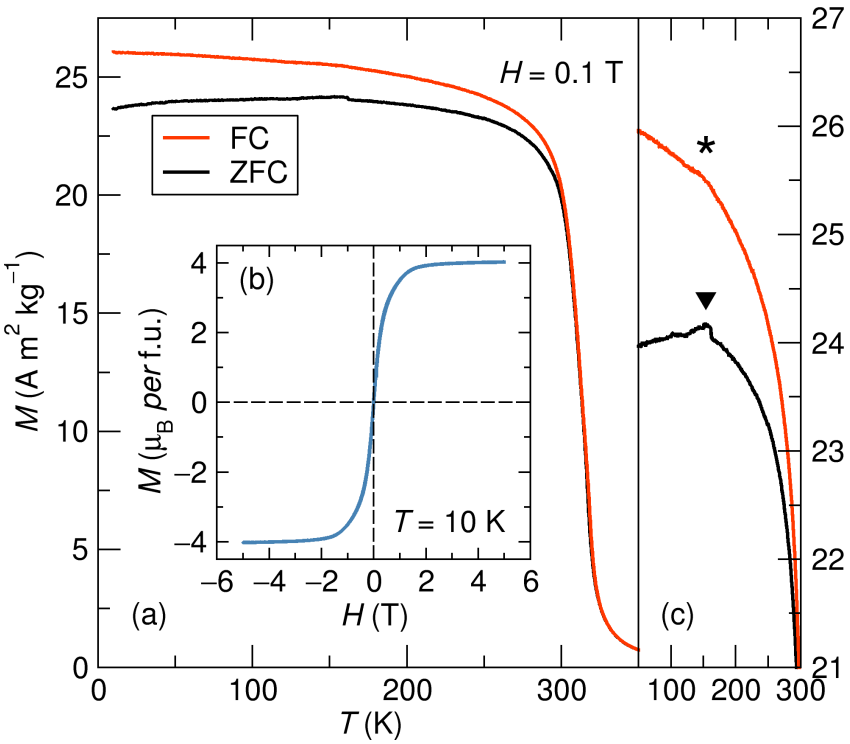

Figure 3.3: (a) ZFC and FC temperature–dependent magnetization of MnPdGa taken under a constant field of $H = 0.1$ T. The sample ferromagnetically orders at $T_C = 315$ K and there is an AFM component at around $T_N = 160$ K. (b) Field–dependent magnetization taken at $T = 10$ K between $H = -5$ T and 5 T. (c) Temperature–dependent magnetization around 150 K to 300 K is shown to highlight the AFM component.

violations or secondary phases in the sample. In particular, we do not find any evidence of inversion-symmetry breaking as proposed in a recent report on MnPtGa.[100] The small discrepancies that the model has with the data are potentially due to strong absorption of the X–ray beam by the sample.

Temperature– and field–dependent magnetization data are shown in Figure 3.3. The M *vs.* T data taken under a constant field of $H = 0.1$ T reveals that MnPdGa develops FM order at $T_C = 316$ K. This T_C agrees with previous studies of MnPdGa.[94, 95] In addition, these studies find a second transition associated with canting of the magnetic moments into a canted AFM state around 140 K,[94, 95] which we see here at around 160 K in both the ZFC and FC data. The transition is small in the M *vs.* T

because it is into a canted state rather than a full AFM state, but agrees with these previous reports which also saw very small inflection changes in the M *vs.* T data. The inset (Fig. 3.3(b)) shows M *vs.* H at $T = 10$ K, and the saturation moment at 2 T is 94.6 A m^2 kg^{-1} (3.91 μ_B *per* f.u.). This moment is much larger than that observed in the MnPtGa under similar conditions (2.6 μ_B[92] to 3.15 μ_B[101] *per* f.u.). The shape of this M *vs.* H curve is characteristic of a ferromagnetic material. Canted antiferromagnets also show a similar shape since they have a net moment, so the M *vs.* H data does not discount the canted AFM transition at 160 K. However, the high saturated moment at high field for MnPdGa suggests that the canted AFM moments are aligned back into a FM structure.

To characterize the magnetic entropy change of MnPdGa, M *vs.* T data were taken at 8 fields between $H = 0.1$ T and 5 T (Figure 3.4(a)). The derivatives of these data were taken and then integrated to give the ΔS_M curves in Figure 3.4(b) according to the formula $\Delta S_M(T, H) = \int_0^H (\partial M)/(\partial T)_{H'} dH'$. The maximum ΔS_M at $H = 5$ T is -3.54 J kg^{-1} K^{-1}. This value is somewhat lower than expected based on the $\Sigma_M = 2.8\%$ prediction. For comparison, MnCoP, with $\Sigma_M = 3.0\%$, shows $\Delta S_M = -6.0$ J kg^{-1} K^{-1}.[68] Some of this discrepancy is due to the high density of MnPdGa (8.5 g cm^{-3}) which leads to poor gravimetric performance. In the case of MnPdGa, it may be more useful to compare the volumetric entropy change rather than the gravimetric entropy change with other magnetocalorics. When expressed volumetrically, the ΔS_M of MnPdGa and MnCoP are 30.1 mJ cm^{-3} K^{-1} and 41 mJ cm^{-3} K^{-1}, respectively.

In addition, the RC was calculated for MnPdGa using full–width and half–maximum. The ΔS_M curves are rather broad, with FWHM temperature span between 266.0 K and 354.5 K for an applied field of 5 T. This results in a large RC of 224.6 J

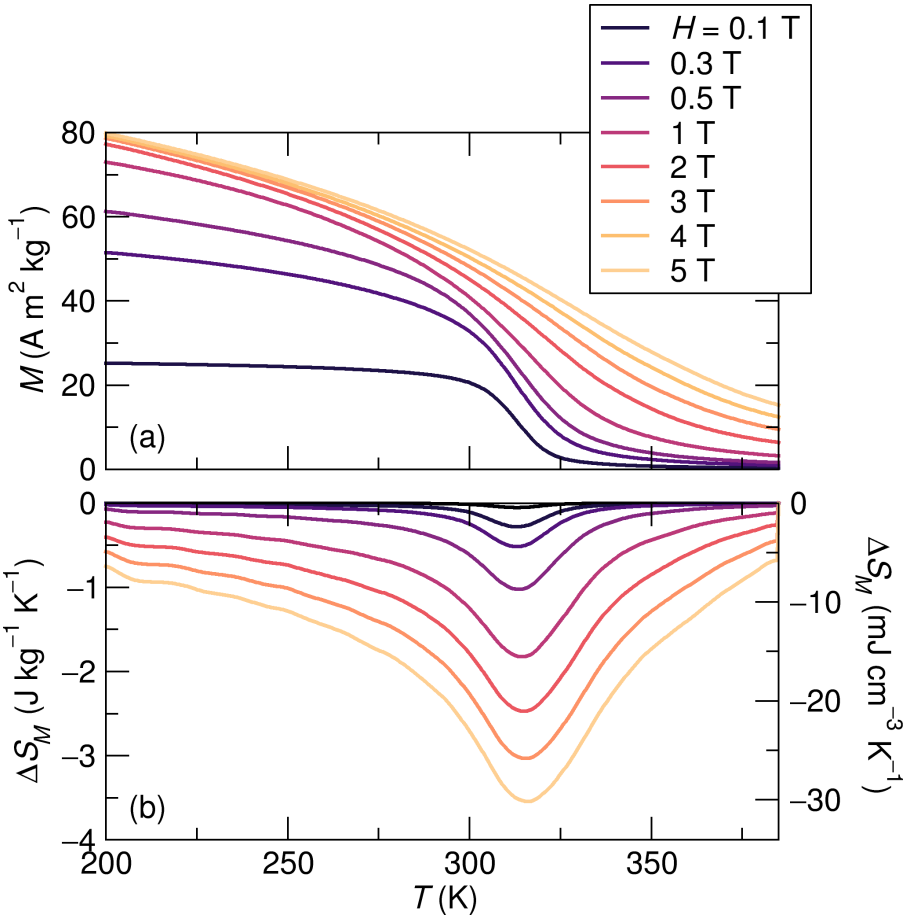

Figure 3.4: (a) Temperature–dependent magnetization data were taken at various fields. (b) Derivatives of each curve were taken and integrated to yield ΔS_M. The maximum $-\Delta S_M$ is 3.54 J kg^{-1} K^{-1}.

kg^{-1} for an applied field of 5 T. Under a field of $H = 2$ T, the FWHM falls between 279.0 K and 338.7 K, with a RC of 85.1 J kg^{-1}. These values are in line for the RC values for many good magnetocalorics, which may be found previously tabulated.[15] Therefore, despite the fairly low gravimetric ΔS_M, the RC calculation suggests that MnPdGa nevertheless may be an interesting magnetocaloric near room temperature.

In MnPtGa, the calculated Σ_M is 2.4%, similar to that of MnPdGa (2.8%). However, a much smaller gravimetric entropy change is observed, with a peak ΔS_M of –1.9 J kg^{-1} K^{-1} under an applied field $H = 5$ T. The heavy Pt again contributes to this low gravimetric entropy change, and the corresponding volumetric entropy change is -22.3 mJ cm^{-3} K^{-1}, more comparable to that of MnPdGa.[92]

From these experimental results, it is clear that the magnetocaloric effect in MnPdGa and especially MnPtGa is not as impressive as predicted by Σ_M. The thermodynamic origin of this behavior is that the magnetic structure of both compounds is not purely FM, but includes an AFM component which accounts for a fraction of the ordering energy. To resolve the precise difference in the magnetic ordering energies of these two compounds, we turn to density functional theory (DFT) calculations.[2]

We first characterize the local magnetic structure of both materials by computing the energy profile of possible canted AFM configurations, from the pure FM to the AFM limits. This energy profile is shown in Figure 3.5(a) and 3.5(b) for spin directions alternating along the c and a crystal axes respectively. The spin–spin interactions along the c–direction are highly non–linear, reflecting a large contribution of direct exchange within the chain of Mn atoms lying along the c–axis. The optimal local spin configuration is a 1D chain of canted moments alternating their angle to the c–axis, consistent with the previously proposed canted AFM structure. In both materials, the spins favor

[2]The DFT calculations included here were performed by Dr. Daniil A. Kitchaev.

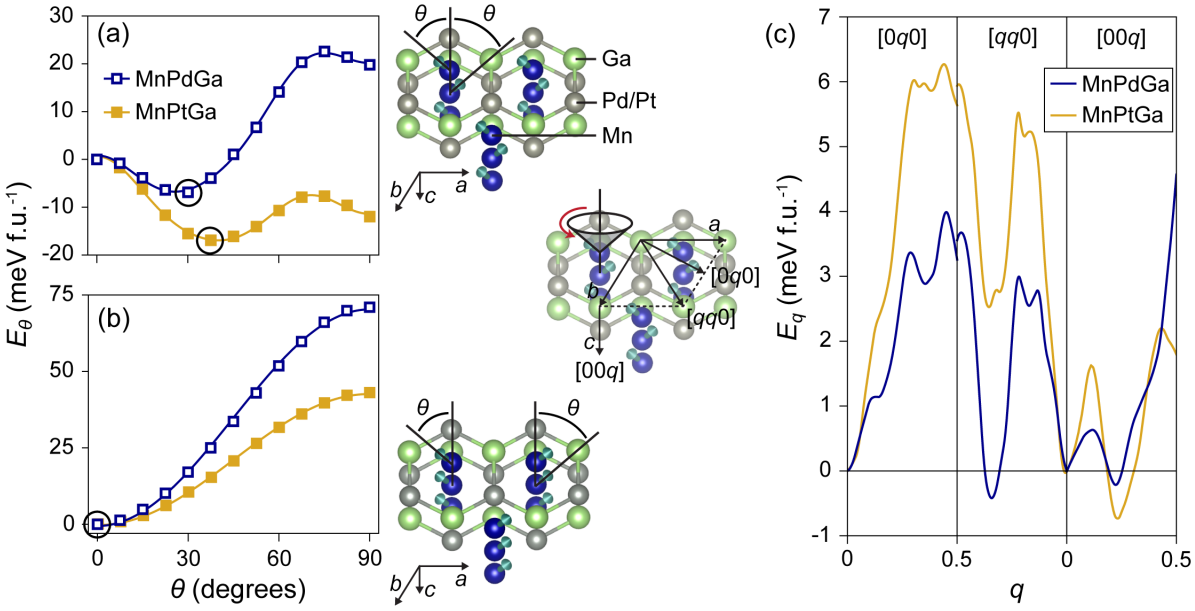

Figure 3.5: Computational comparison of the short– and long–range magnetic structures in MnPdGa and MnPtGa. (a), (b) Energy of the canted AFM phase as a function of canting angle θ, where the spins alternate canting directions along the (a) c–direction or the (b) a–direction. (c) Energy of conical spin waves defined by a rotation of the locally-optimal canted AFM phase (panel (a)) around the c–axis, with propagation wavevector q.

a local FM alignment within the (ab)–plane, with an energy profile consistent with a bilinear Heisenberg model. These magnetic energy profiles are negligibly affected by spin–orbit coupling, indicating that this non–collinear itinerant magnetic state arises solely from exchange effects.

Having established the canted AFM structure as the local magnetic ground state, we search for long-range instabilities with respect to the formation of spin waves. While the formation of conventional spin helices is not favorable for any wavevector, we find that conical spin waves can have lower energy than the local canted AFM structure. As shown in Figure 3.5(c), these low-energy conical spin waves are defined by a rotation of the canted AFM structure around the crystal c–axis with a propagation wavevector q. The dispersion relation shown in Figure 3.5(c) maps the energies of these spin waves for high-symmetry wavevectors. MnPtGa has a single energy minimum corresponding to a spin density wave propagating along the c–axis, consistent with the neutron refinement reported by Cooley *et al.*[92] MnPdGa exhibits two weaker minima, favoring spin waves along the [110] direction in addition to [001]. As with the local canted AFM state, the conical spin wave ground states arise from itinerant exchange effects rather than spin–orbit coupling.

The formation of the canted AFM structure in MnPtGa was previously explained by an instability in the electronic density of states of the FM structure.[92] We find that a similar instability exists in MnPdGa. Figure 3.6(a) shows the non-spin-polarized DOS, which features a strong peak in the Mn states at the Fermi level, characteristic of a Stoner instability. As in conventional ferromagnets, this instability can be relieved by the introduction of spin–polarization into the electronic structure, as shown in Figure 3.6(b). In the FM state, the large peak in Mn states at the Fermi level is split into an occupied peak in the majority spin states below the Fermi level, and an unoccu-

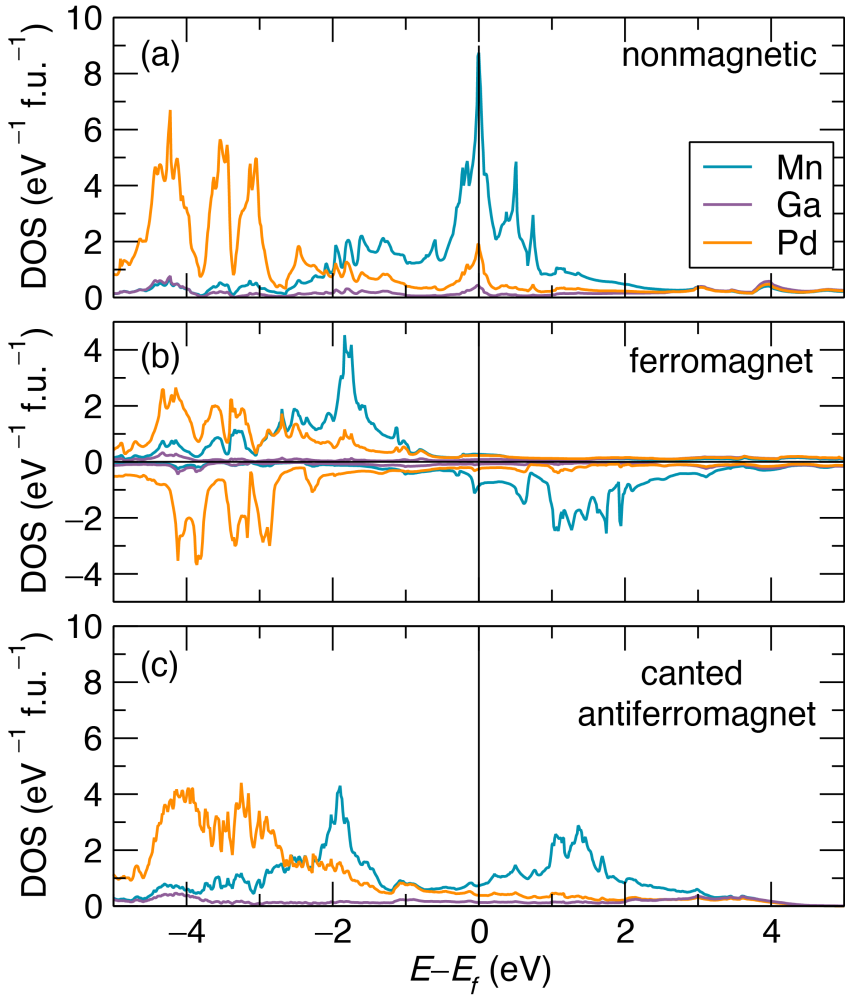

Figure 3.6: Electronic density of states (DOS) for MnPdGa with different magnetic structures: (a) The DOS with no spin-polarization. (b) Collinear FM state. States are split into majority spin states (shown as positive DOS) and minority spin states (shown as negative DOS). (c) The lowest energy calculated canted magnetic state (see Fig. 3.5 for a depiction of the structure). All states are shown in the same spin channel.

pied peak in the minority spin states above the Fermi level, lowering the energy of the system. However, a small peak at the Fermi level persists in the minority spin states of the FM DOS. Formation of the lower symmetry non-collinear canted magnetic state eliminates the peak at the Fermi level and further lowers the energy of the system (Fig. 3.6(c)).

The results of our DFT analysis compare favorably with the experimental picture of MnPdGa and MnPtGa and suggest several explanations for the difference in their behaviors. Previous neutron studies of these materials have proposed that upon cooling through T_C, both materials form a FM phase, which transforms into a canted AFM phase at $T_N < T_C$. Cooley *et al.*[92] have shown that upon further cooling the canted AFM phase in MnPtGa develops a long–wavelength modulation along the c–axis, forming a low-T spin–density wave consistent with the conical spin–wave structure shown in Figure 3.5(c). An analogous phase has not been observed so far in MnPdGa.[94] Our DFT results indicate that while the formation of conical spin waves is favorable in both chemistries, there is a single strong minimum in the MnPtGa dispersion relation, as compared to four weak minima for MnPdGa. Thus, MnPtGa is more likely than MnPdGa to form coherent spin waves with a single q–vector, and retain this order at elevated temperatures. Note that none of these spin–wave structures explain the possible formation of biskyrmion magnetic textures in MnPdGa, which have much larger wavelength and are more likely to be caused by structural symmetry breaking and an associated emergence of Dzyaloshinskii–Moriya interactions.[100, 102, 103]

In relation to magnetocaloric behavior, the critical distinction between these two materials is the greatly diminished saturation moment in MnPtGa as compared to MnPdGa. At low T, the energy scale of the canted AFM phase shown in Fig. 3.5(a) is large enough that at all experimentally relevant fields, both materials will locally maintain

the canted AFM structure and resist field–polarization. However, the fully AFM state is a low–energy local minimum in MnPtGa, and nearly a global maximum in MnPdGa. This energy profile means that AFM domain walls are metastable in MnPtGa, resistant to annealing or elimination under applied field. We speculate that this stability of domain walls is responsible for the diminished macroscopic moment seen in MnPtGa at low–T,[104] rather than a substantial difference in the partially AFM local spin structure. At temperatures approaching T_C, an additional relevant feature of the energy profile in Fig 3.5(a) is the relative energy of the FM state ($\theta = 0$) as compared to other spin configurations. In MnPdGa, the FM state is substantially lower in energy than in MnPtGa, suggesting that this material is more susceptible to polarization by applied field, once again yielding an enhanced macroscopic magnetization.

3.5 Conclusion

High–resolution synchrotron data confirms that MnPdGa crystallizes in the hexagonal $P6_3/mmc$ Ni_2In–type structure. Despite a significant DFT–predicted Σ_M, the magnetocaloric properties of MnPdGa have thus far not been reported. MnPdGa displays a modest ΔS_M but a significant volumetric entropy change, and the RC calculated at FWHM shows that it may be a promising magnetocaloric material. The broad transition that we see may be improved by annealing the sample at a different temperature, and other work on MnPdGa suggest that varying the Mn to Pd ratio could have interesting effects on the FM transition.[94] Furthermore, although magnetostructural coupling was not confirmed in this study, the low saturation magnetization yet significant RC indicates that magnetostructural coupling may contribute to the magnetocaloric effect in MnPdGa. DFT calculations reveal that canted and conical spin-wave spin structures

are favorable in MnPdGa, but less so than in MnPtGa, explaining the improvement in the magnetocaloric figure of merit between MnPtGa and magnetocaloric performance in MnPdGa.

Chapter 4

Tuning the superconducting and charge density wave transition temperatures in AV$_3$Sb$_5$ *via* partial substitution

4.1 Abstract

The recently reported AV$_3$Sb$_5$ (A = K, Rb, Cs) family of kagome metals are candidates for unconventional superconductivity and chiral charge density wave (CDW) order. Recent studies have proposed the importance of band structure saddle points proximal to the Fermi energy in governing these two transitions. Here we use chemical substitution to introduce holes into AV$_3$Sb$_5$ and unveil an unconventional coupling of the CDW and superconducting states. Specifically, we generate phase diagrams for AV$_3$Sb$_{5-x}$Sn$_x$ that illustrate the impact of hole doping the three systems and lifting the

nearest vHs toward E_F. In $CsV_3Sb_{5-x}Sn_x$, superconductivity exhibits a non-monotonic evolution with the introduction of holes, resulting in two "domes" peaked at 3.6 K and 4.1 K and the rapid suppression of three–dimensional CDW order. Conversely in A = K and Rb, hole–doping causes the superconducting T_C to increase to about 4.5 K while rapidly suppressing the CDW state. The evolution of CDW and superconducting order is compared with the evolution of the electronic band structures of $AV_3Sb_{5-x}Sn_x$, where the complete suppression of superconductivity seemingly coincides with an electron-like band comprised of Sb p_z orbitals pushed above E_F.

4.2 Introduction

The recently discovered class of AV_3Sb_5 (A = K, Rb, Cs) kagome metals [39] exhibit CDW order followed by the low temperature onset and coexistence of superconductivity.[42, 43, 46] Upon applying hydrostatic pressure, the CDW instability in AV_3Sb_5 is coupled to superconductivity in a seemingly unconventional fashion,[54, 55] and the impact of the pressure–modified band structure on the interplay between the two states remains an open area of study. In particular, understanding the relative roles of the vHs comprised of V d-orbital states near the M–points and the electron–like band comprised of Sb–states at the Γ–point within the CDW and SC mechanisms is essential to developing a microscopic picture of how the two transitions are coupled.

Carrier doping is an appealing means of tuning these features relative to the Fermi level and probing the coupling of the CDW and SC states. Shifting the relative positions of the vHs and Γ pocket relative to E_F and probing the evolution and interplay of the CDW and SC phase transitions can provide insights into the origins of each state. A

recent study on oxidized thin flakes of CsV_3Sb_5, for instance, shows that hole doping on the Cs site can enhance T_C while also suppressing CDW order.[58] In addition, DFT calculations show that hole doping drives the vHs in the opposite direction relative to E_F than that expected *via* external hydrostatic pressure.[105] Given that an unusual coupling between SC and CDW states was observed under variable pressure,[55] a systematic study of hole–doping effects stands to provide an important experimental window into understanding this unconventional coupling.

The electron pocket comprising Sb p_z orbitals at Γ and saddle points arising from V d–orbitals at M–points are regarded as playing important roles within the SC and CDW states. Consequently, resolving their behaviors when subject to external perturbations such as pressure and chemical doping is important to understand. Here, we report the effect of hole doping in CsV_3Sb_5 with Sn substituting Sb, and a double superconducting dome is observed under light hole substitution. The termination of the second dome is attributed to the lifting of the Γ pocket above E_F and the removal of the Sb p_z orbitals from the Fermi surface; however the formation of the first dome remains anomalous. Within the first SC dome, CDW order rapidly vanishes at doping levels corresponding to only slight movement of the van Hove singularities (vHs) at the M point toward E_F.[106] Curiously, while applied external pressure moves the M saddle points away from E_F, it achieves a similar phase diagram suggesting a delicate balance of energy scales within the unperturbed parent structure [55, 105] and the dominance of removing the CDW state in governing the formation of the first SC dome.

In contrast to the above, pressure studies of KV_3Sb_5 and RbV_3Sb_5 have reported only a single superconducting dome coinciding with the suppression of CDW order; [54, 107] however studies of carrier–induced perturbations of these variants remain unexplored. To further explore similarities between pressure–induced and carrier–

induced perturbations of the interplay between CDW and SC orders, the effect of hole doping AV_3Sb_5 with in solid solutions with A = K, Rb is also presented. In both systems, only one superconducting dome is observed in contrast with $CsV_3Sb_{5-x}Sn_x$, although a similar, rapid CDW suppression is observed. The solubility limit of Sn in KV_3Sb_5 is the lowest in the family, with phase separation observed by $x = 0.30$. In contrast RbV_3Sb_5 supports up to $x = 0.70$ of Sn replacing Sb. While the differences in solubility can be explained by A cation size effects, the difference between the single dome hole doping phase diagrams of KV_3Sb_5 and RbV_3Sb_5 relative to double dome phase diagram of CsV_3Sb_5 suggests a difference in the parent CDW state between the three materials. The potential origins of these differences are discussed.

4.3 Methods

Stoichiometric quantities of elemental Cs (liquid, Alfa 99.98%), V (powder, Sigma 99.9%), Sb (shot, Alfa 99.999%), and Sn (shot, Alfa 99.9999%) were weighed in an argon glove box with oxygen and water levels of < 0.5 ppm. Vanadium powder was cleaned prior to the synthesis using EtOH and concentrated HCl to remove residual oxides. The elements were loaded in a tungsten carbide ball mill vial and milled for 60 min in a SPEX 8000D high-energy ball mill. Resulting powders were ground in agate, sieved through a 106 micron sieve, sealed in fused silica, and annealed at 823 K for 48 K. A secondary grind and anneal (723 K, 12 h) was utilized to ensure best superconducting fractions and Sn homogenity. The resulting powder is dark grey and air stable.

High–resolution synchrotron powder X–ray data were acquired at Argonne National Laboratory (APS, 11-BM) with an average wavelength of $\lambda = 0.458$ Å. Powders

were diluted with ground silica before packing in 0.8 mm kapton capillaries to reduce X–ray absorption. Additional powder X–ray (pXRD) data were collected on a Panalytical Empyrean powder diffractometer equipped with a PIXcel 1D detector. Topas Academic[85] was used to refine the patterns with Pawley and Rietveld fitting,[86] and crystal structures were visualized using VESTA.[87] A Hitachi TM4000Plus scanning electron microscope (SEM) was used to perform energy–dispersive X–ray spectroscopy (EDS). The AztecOne software was used to analyze and obtain the chemical composition in higher Sn content samples.

A Quantum Design Magnetic Property Measurement System (MPMS) with a vibrating sample magnetometer (VSM) was used to take magnetization data. Approximately 15 mg of powder was packed in a plastic VSM capsule and loaded in a brass rod sample holder. Superconductivity measurements utilized an applied field of 5 Oe. Due to the intrinsically low moment of CsV_3Sb_5, temperature–depenedent CDW measurements utilized a higher field of $H = 10000$ Oe. A Quantum Design Physical Property Measurement System (PPMS) Dynacool was used for resistivity measurements. Resistivity measurements were performed using a standard 4–point contact geometry. Silver paint and gold wire were used to make electrical contact to sintered, pressed bars of Sn-doped AV_3Sb_5. The electrical transport option was used with a constant frequency of $\sim$15 Hz and a current of 1 mA.

The room temperature ^{121}Sb zero field nuclear quadrupolar resonance (NQR) measurements were done at Brown University and conducted by Jonathan Frassinetti, Erick Garcia, and Rong Cong. The NQR data was recorded using a state of the art laboratory–made NMR spectrometer. The spectra were obtained, at each given value of frequency, from Fourier transforms of the spin–echo. A standard spin echo sequence $(\pi/2 - \tau - \pi)$ and $\pi/2$ pulse that optimized signal intensity of 3.4 μs were used. The shape of the

spectra presented in the manuscript are independent of the duration of time interval τ. The NQR relaxation rate T_1^{-1} was measured using a Spin Stimulated Echo 3-pulse sequence $(\pi/2 - \tau - \pi/2 - \tau_d - \pi/2)$ to obtain magnetization recovery curves $M(\tau_d)$. The resulting value of the rate was obtained by fitting the magnetization to a single exponential function of time $M(\tau_d) \propto \exp(-t/T_1)$. Since the nuclear spin I of ^{121}Sb equals to $5/2$ and both Sb sites (Sb1 and Sb2) are in non–cubic environments, two distinct quadrupolar lines are observed per site [108]. The shift was obtained from the frequency of the first moment of spectral distribution.

For electronic state calculations, first–principles calculations based on density functional theory (DFT) within the Vienna ab initio Simulation Package (VASP) were performed.[96, 109] The projector augmented wave (PAW) method [97, 98] was employed and relaxations of the ionic positions were conducted using an energy cutoff of 520 eV. Reciprocal space k-point meshes were automatically generated at a density of 55 Å^{-1} along each reciprocal lattice vector. The band structure was calculated across the main paths along the high symmetry points as defined by Setyawan and Curtarolo.[110] Density of states (DOS) and band structures were visualized using the sumo package.[111] The CsV_3Sb_5 structure has 5 sites for Sb atoms. Two sites are unique and symmetrically distinct: within the kagome plane (Sb1), and out of the kagome plane (Sb2). In this study we calculated both cases of when Sn substitutes in the Sb1 site and when Sn is in one of the Sb2 sites.

4.4 Results and discussion of $CsV_3Sb_{5-x}Sn_x$

Here the effect of hole–doping on the CDW and SC states in $CsV_3Sb_{5-x}Sn_x$ with $0 \leq x \leq 1.5$ is presented. Hole–doping is achieved *via* substitution of Sn onto the Sb

sites, and, because Sn and Sb are very similar in size, this drives negligible coincident steric effects in the band structure. As holes are introduced, the CDW state is rapidly suppressed, and three–dimensional CDW order vanishes near $x = 0.06$. In parallel, SC is enhanced and reaches a maximum $T_C = 3.6\,\mathrm{K}$ at $x = 0.03$ within the CDW state before decreasing as the CDW is fully suppressed. Continued hole doping beyond the suppression of CDW order results in a second maximum in $T_C = 4.1\,\mathrm{K}$ at $x = 0.35$ prior to bulk SC weakening and vanishing beyond $x = 0.5$. Density functional theory (DFT) calculations and nuclear quadrupolar resonance measurements establish a strong preference for Sn to occupy Sb sites within the kagome plane (Sb1), and DFT models predict that Sn substitution on this site lifts the Sb p_z electron–like band at Γ above E_F coincident with the vanishing of bulk SC. Furthermore, only small changes in the energies of the vHs are predicted for doping levels sufficient to suppress signatures of CDW order, suggesting the importance of Sb-states in the stabilization of both phases.

At room temperature, $CsV_3Sb_{5-x}Sn_x$ with $0 \leq x \leq 1$ all adopt the same hexagonal $P6/mmm$ structure as CsV_3Sb_5 with an ideal kagome network of V atoms, shown in Fig. 4.1(a). For $0 \leq x \leq 1$, polycrystalline samples were found to be single phase, while a secondary phase appears for $x = 1.5$, indicating the termination of the solid solution. The emergence of the secondary phase is clear in powder X–ray diffraction as seen in Figure 4.2, where the extra peaks in $CsV_3Sb_{3.5}Sn_{1.5}$ are marked by asterisks. The secondary phase was not determined, as it was present in only very small quantities with minimal peaks. Pawley fits of powder diffraction data were used to determine changes to the unit cell as a function of Sn content. Figures 4.1(b–c) show the normalized c/a ratio and the cell volume as a function of Sn content. With increasing Sn, a increases and c decreases in near perfect compensation, yielding a cell volume which is virtually

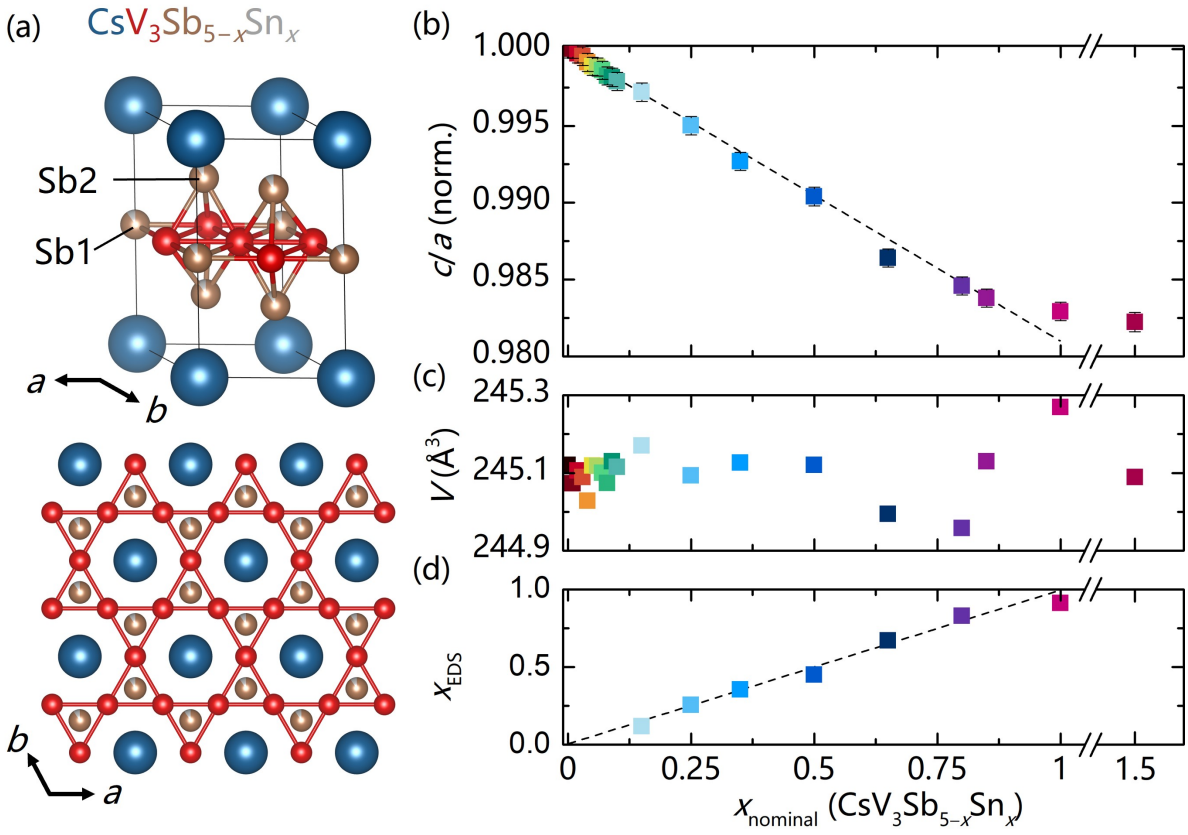

Figure 4.1: (a) $CsV_3Sb_{5-x}Sn_x$ crystallizes in the parent CsV_3Sb_5 ($P6/mmm$) structure. Sn can substitute on either the Sb1 or Sb2 sublattices, and at low doping we establish a preference for the Sb1 site in the V kagome plane. (b-c) Sn integration into $CsV_3Sb_{5-x}Sn_x$ causes the c/a ratio to steadily decrease until the termination of solid solubility at $x = 1$. (d) For samples with concentrations above EDS sensitivity threshold, nominal Sn tracks measured Sn. Error bars are shown unless they are smaller than associated point size. The different colors correspond to sample composition and are consistent throughout the figures.

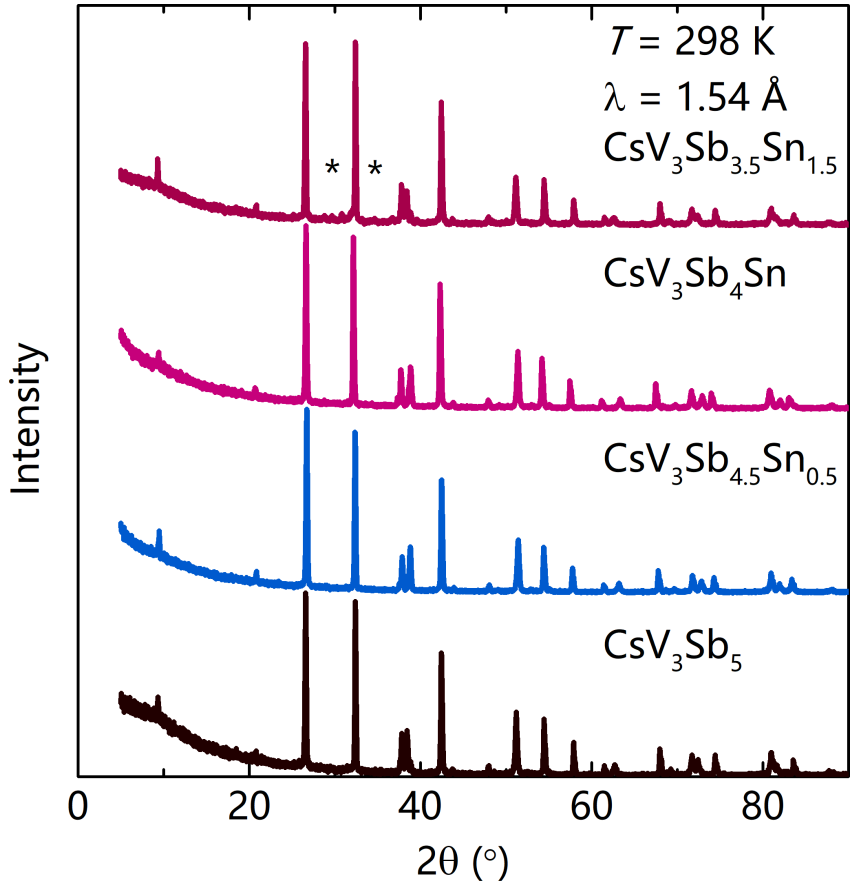

Figure 4.2: As Sn content is increased in $CsV_3Sb_{5-x}Sn_x$, a secondary phase emerges after $x = 1$. The secondary phase is marked by asterisks for $x = 1.5$.

independent of Sn content. Small fluctuations in volume of less than 0.16% can be explained by uncertainties in chemical composition and in the structural refinement.

The linear trend in c/a is reminiscent of a Vegard's Law–type trend, suggesting that Sn is incorporated into the parent structure as a solid solution up to approximately $x = 1$, at which point the c/a ratio plateaus. Figure 4.1(d) indicates that the measured Sn content (*via* EDS) tracks the nominal Sn content. While Rietveld refinements of X–ray data confirm that powders are single phase, poor scattering contrast between Sb and Sn impedes the ability to refine whether Sn is uniformly distributed on both the Sb1 and Sb2 sites, or whether there is preferential occupation of a particular sublattice.

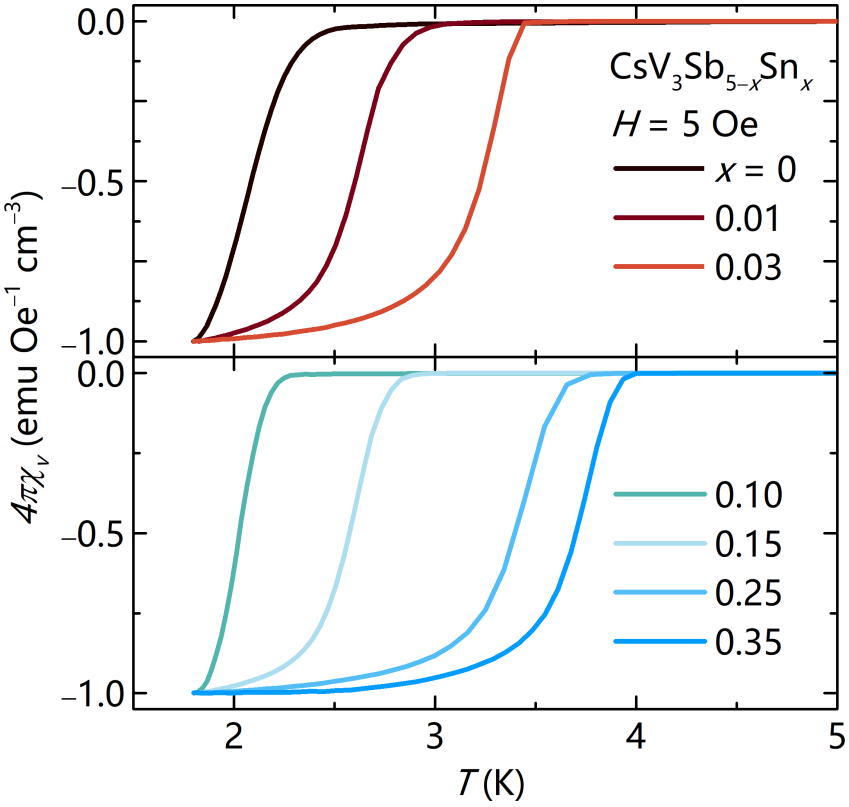

Figure 4.3: (a) The superconducting T_C measured under a field of $H = 5$ Oe shows a systematic shift to higher temperature in the compositions leading to the two T_C maximums. The superconducting fraction is normalized to account for errors in mass and packing fraction so all data have a minimum of -1, the theoretical minimum. (c) Resistivity data also show this enhancement in T_C, and the low–T, normal state resistivity for $x = 0.35$ is about 4 times higher than $x = 0.03$.

DFT calculations suggest a preference ≈ 10 meV/atom for Sn to substitute preferentially on the Sb1 (in the kagome plane) and nuclear quadropole resonance (NQR) measurements (discussed later) confirm that Sn atoms preferentially occupy this site.

Undoped CsV_3Sb_5 single crystals have a superconducting $T_C = 2.5$ K [42, 58] and a charge density wave transition temperature $T^* = 94$ K.[41, 44] Polycrystalline samples show identical transition temperatures, although both transitions are broader compared to single crystals [42]. This is largely due to powders being very sensitive to exact synthesis conditions and strain effects. Pure CsV_3Sb_5 powder synthesized here

has an onset T_C of 2.70 K and a midpoint T_C of 2.07 K. As Sn is added within the matrix, Figure 4.3 shows the evolution of superconductivity, focusing on two different doping regimes (x = 0 to 0.03 and x = 0.1 to 0.35). All superconducting samples show $4\pi\chi_v \approx -1$ in magnetization. Fractions slightly exceeding unity are attributed to errors in the packing density, and data are normalized to -1 for ease of comparison. The effect of Sn on T_C becomes immediately apparent: as the Sn content is increased to x = 0.03, T_C increases to a local maxima of 3.6 K. T_C then decreases with continued hole doping, followed by a second superconducting dome appearing shortly thereafter with a maximum T_C = 4.1 K at x=0.35. Superconductivity assumes only a partial volume fraction for $x > 0.5$, and the SC state completely disappears by x = 0.85. This decrease in superconducting state is clear in temperature dependent susceptibility as shown in Figure 4.4.

As Sn is introduced into the CsV_3Sb_5 lattice, the CDW transition as observed *via* M *vs.* T measurements broadens and decreases in temperature (Figure 4.5(a)). The transition is observed as a clear inflection in CsV_3Sb_5 as marked by the arrow, but is quickly suppressed until an inflection is not clearly observed by $CsV_3Sb_{4.94}Sn_{0.06}$. The evolution of CDW order upon hole doping can be monitored *via* this inflection point in magnetization that appears at the CDW onset. Using the peak in dM/dT as a metric for the onset of three–dimensional CDW order, Fig. 4.5(b) shows that light hole substitution causes the CDW transition to rapidly broaden and shift to lower temperatures. The peak in dM/dT is 98.01 K in undoped CsV_3Sb_5 and this peak decreases to less than 80 K at x = 0.04. For $x > 0.05$, signatures of the CDW transition in magnetization cannot be resolved, although it is possible that a highly broadened CDW anomaly smoothly continues its rapid suppression with higher Sn doping. Despite the ambiguity in the precise position of CDW phase boundary near x = 0.05, the superconducting

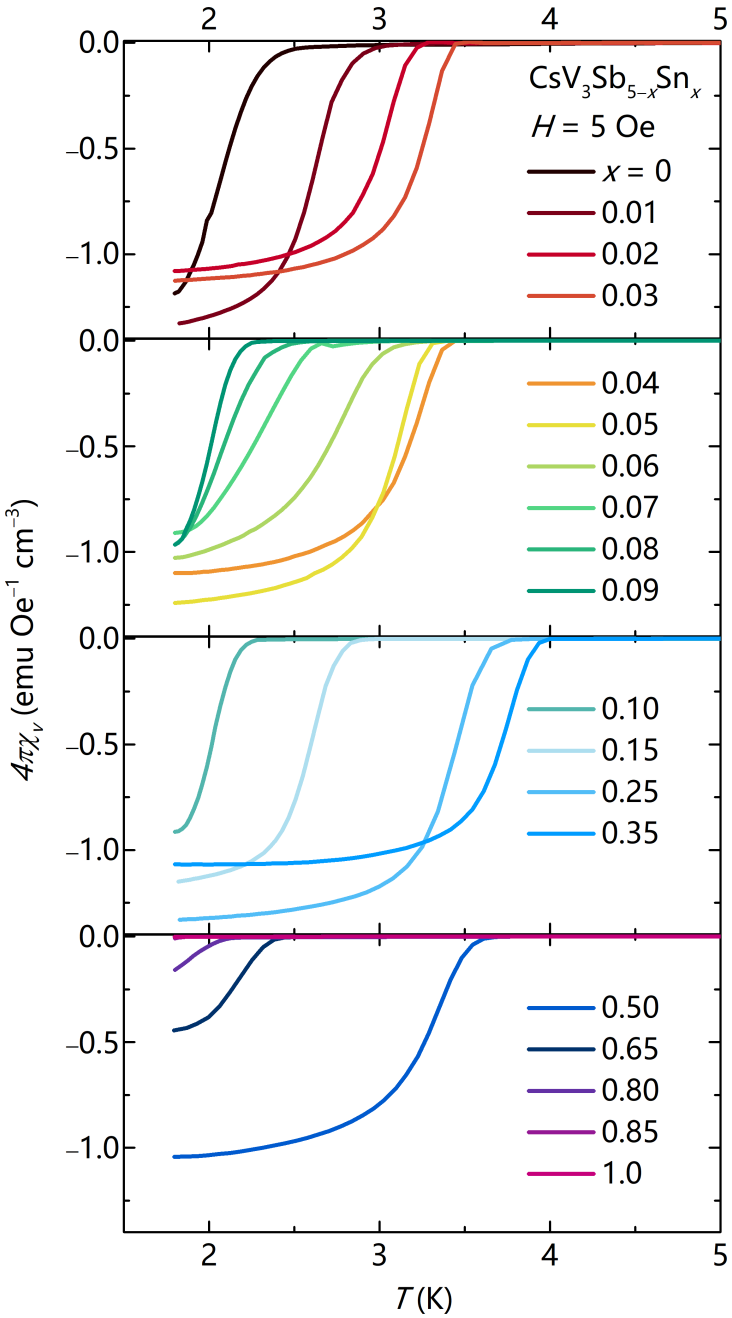

Figure 4.4: Susceptibility measurements ($H = 5$ Oe) on powders of $CsV_3Sb_{5-x}Sn_x$ for $0 \leq x \leq 1.0$ show that the superconducting fractions, calculated as $4\pi\chi_v$, are ≈ 1 for $x \leq 0.50$ (data are not normalized in this figure). From $x \geq 0.65$, the superconducting fraction decreases, and superconductivity is fully suppressed by $x = 1$.

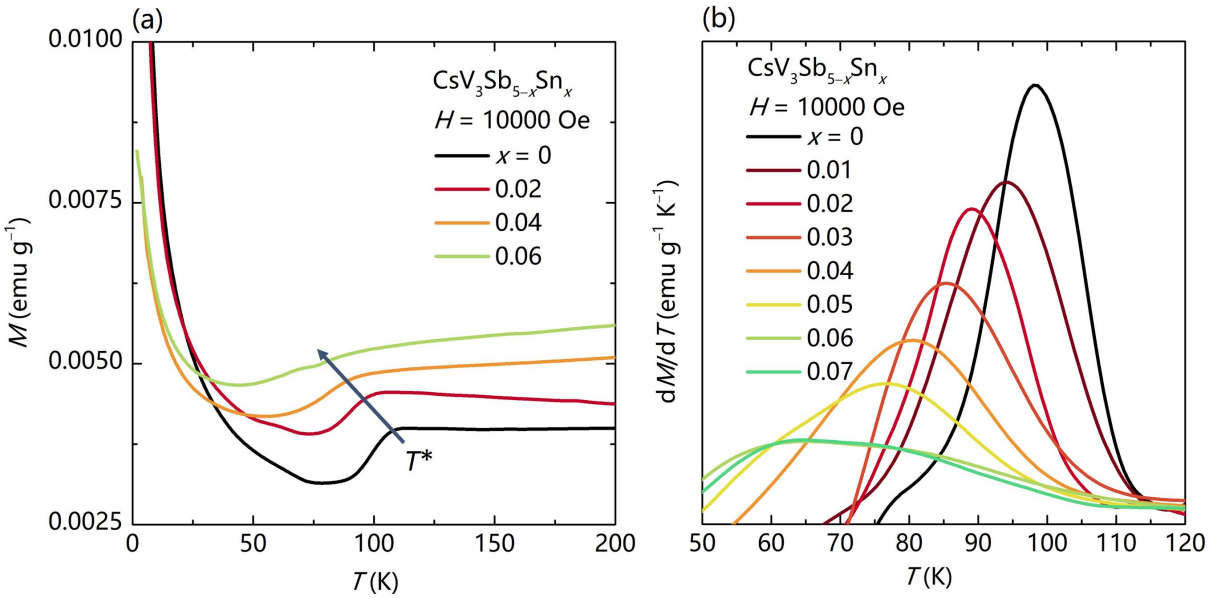

Figure 4.5: (a) Magnetization measurements on powders of $CsV_3Sb_{5-x}Sn_x$ (H = 10000 Oe) show the suppression of the CDW order by x = 0.06. Although there is a clear inflection point for $0 \leq x \leq 0.04$, the magnitude of the CDW order significantly decreases and T^* shifts to lower temperature. The additional slight inflection for x = 0.06 at around 55 K can be attributed to oxygen contamination in the chamber of the instrument. The CDW transition is indicated by the arrow. (b) dM/dT for compositions $x \leq 0.06$ show a decrease in CDW T^*, and this transition disappears for greater Sn compositions.

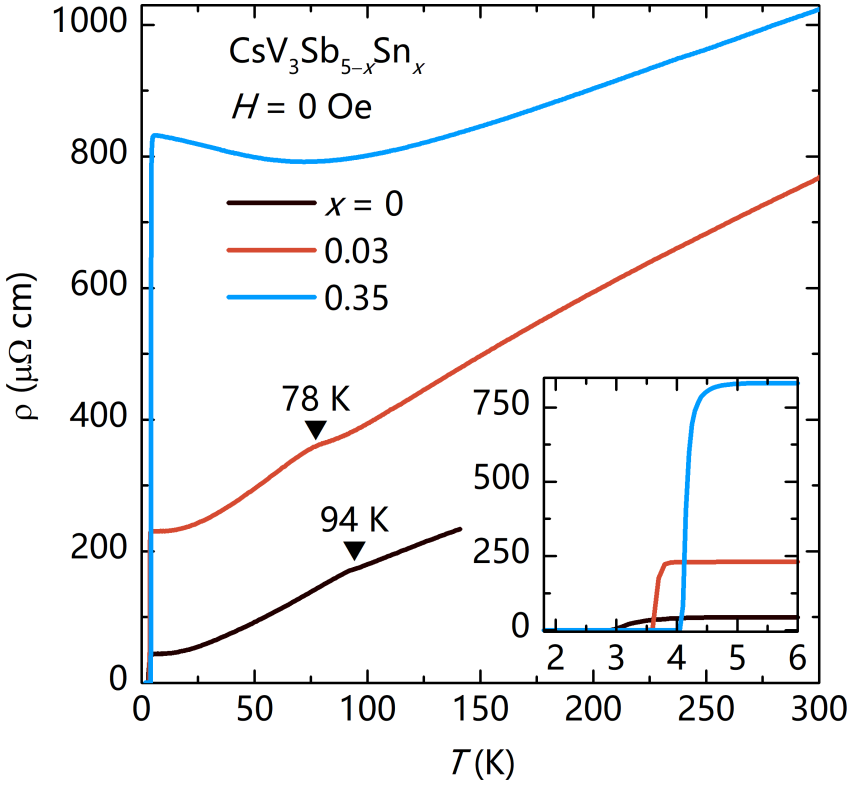

Figure 4.6: Resistivity data also show this enhancement in T_C, and the low–T, normal state resistivity for $x = 0.35$ is about 4 times higher than $x = 0.03$.

and CDW states clearly coexist at the first maximum of the first superconducting dome ($x = 0.03$). This is distinct from the second maximum in T_C at higher Sn content ($x = 0.35$), which occurs far beyond the apparent suppression of CDW order. Future work studying single crystals will be required to fully map if the suppression of the CDW state is a first or second order phase boundary and to fully explore whether CDW order is becoming short–ranged at larger Sn–doping levels.

Figure 4.6 shows electrical resistivity measurements performed on samples at both peak T_C values ($x = 0.03$ and $x = 0.35$). Zero–resistivity conditions agree well with the T_C obtained *via* magnetization measurements, and the CDW onset temperature is further marked for the sample with $x = 0.03$. The resistance immediately prior to the onset of SC increases quite dramatically upon Sn substitution, from 50 $\mu\Omega$–cm (x

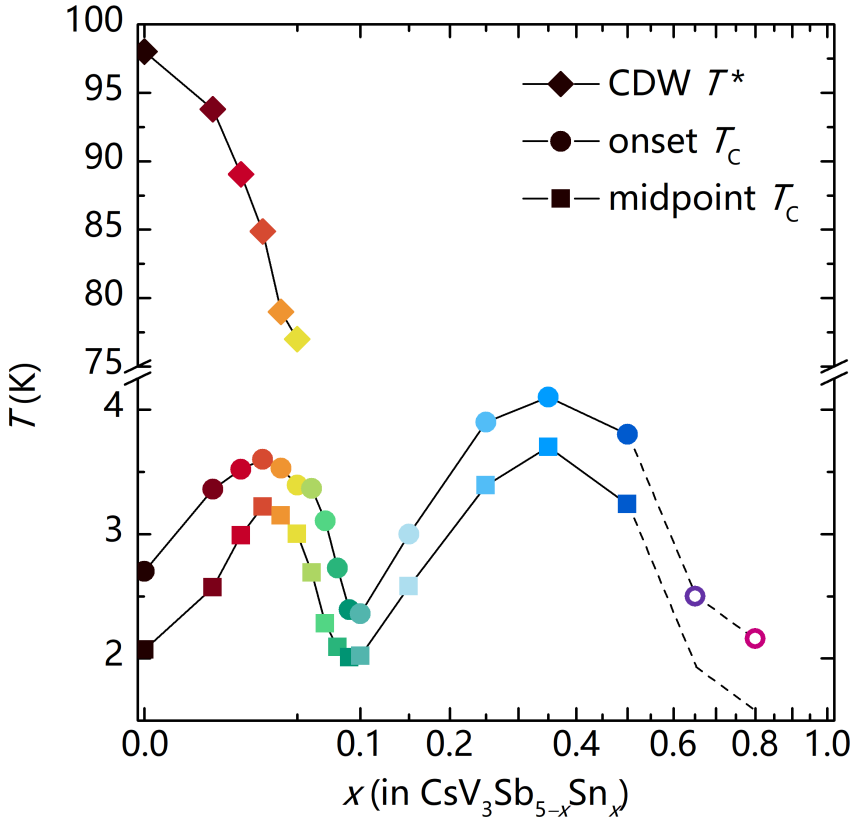

Figure 4.7: Hole–doping phase diagram for $CsV_3Sb_{5-x}Sn_x$. The double-dome structure is clearly evident, as is the depression of the CDW ordering temperature. T_C shows two maxima at x = 0.03 and at x = 0.35 and the CDW state disappears by x = 0.06. We note that the first T_C maximum occurs while the CDW is still present, and the CDW vanishes once T_C is already declining again $x > 0.03$. For $x \geq 0.65$, the volume fraction of superconductivity decreases and the onset T_Cs are represented with open circles.

= 0), to 250 $\mu\Omega$-cm (x = 0.03, first T_C peak), to 800 $\mu\Omega$–cm (x = 0.35, second T_C peak), and the temperature dependence of the resistivity, particularly near the CDW temperature, changes dramatically with Sn doping. As a summary, Figure 4.7 plots a phase diagram showing the effect of Sn–substitution on both SC and CDW orders. A two–dome structure is immediately evident in T_C, as is the relatively rapid suppression of CDW order with the introduction of Sn.

The CsV_3Sb_5 lattice supports nearly 1/5 of the total Sb being replaced by Sn. To

give a rough sense of the range over which E_F can be tuned, Figure 4.8(a) shows the electronic structure of pure CsV_3Sb_5 along with the range of Fermi levels achievable with a loss of 1 electron per unit cell (gray shaded region). In a rigid band shift approximation, substitution of Sn should allow E_F to be tuned across multiple vHs and Dirac points near the M– and K–points, respectively. However, reconstruction of the bands associated with the Sb orbitals and orbital selective doping effects are expected, and Figure 4.8(c) shows one hypothetical structure with Sn substituted on the Sb2 sublattice (out of the kagome plane). Here, in addition to the expected shift of the Fermi level (note the position of the M–point vHs crossing now ≈ 0.2 eV *above* E_F), a significant reconstruction is also resolved around the K, L, and H points. Notably, the electron–like band at Γ is preserved in this $x = 1$ structure. Alternatively, if Sn substitution instead occupies the Sb1 sublattice within the kagome plane, the overall electronic structure relative to CsV_3Sb_5 is largely preserved and mimics a rigid band shift model (Fig. 4.8(b)). [1]

To clarify the impact of Sn–doping on the band structure, NQR measurements were performed and establish that Sn preferentially occupies the Sb1 sites in the kagome plane.[2] This is consistent with DFT calculations that show a small energy preference for Sn occupying the Sb1 site. Colorized orbital contributions to the band structure structures shown in Fig. 4.8 are presented in Figure 4.9. The Γ pocket in CsV_3Sb_5 arises from the Sb p_z orbitals, which vanishes and is replaced with an electron-like Sn-band far above E_F in the fully Sb1-site substituted CsV_3Sb_4Sn (Fig. 4.9(b)). Moreover, supercell calculations with fractional in–plane Sb substitution (Sb1 sites) as shown in Figure 4.10 show that as Sn content is increased, the band at Γ lifts above E_F near $x = 0.5$ in tandem with the disappearance of bulk superconductivity. This suggests that

[1] All of the DFT calculations presented in this chapter were performed by Farnaz Kaboudvand.
[2] NQR was done at Brown University by Jonathan Frassineti, Erick Garcia, and Rong Cong.

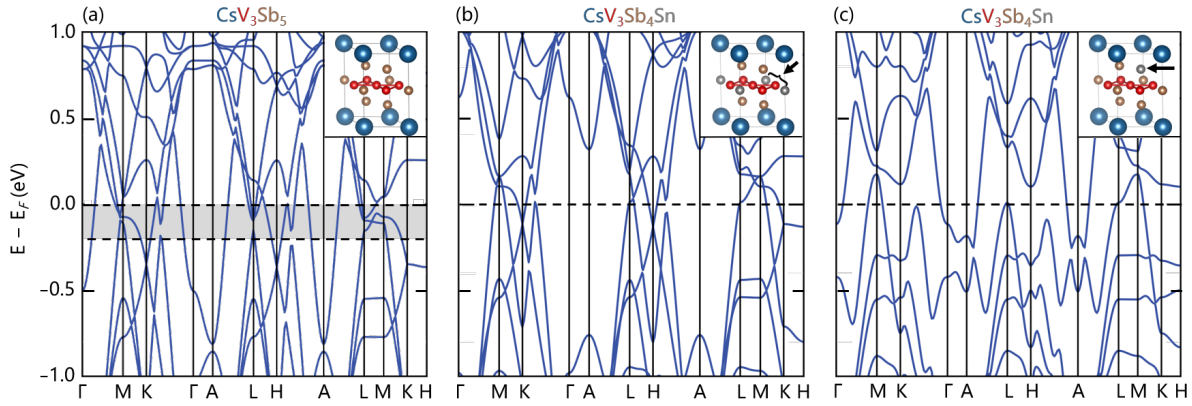

Figure 4.8: (a) DFT calculations for CsV_3Sb_5 highlighting the allowable range of Fermi levels under the rigid band approximation for substitution of one Sn atom per formula unit. (b) Calculation of the band structure of CsV_3Sb_4Sn where one Sn has been substituted within the kagome plane (Sb1). Here the majority of the electronic structure is preserved with the exception of the Γ pocket, where the occupied Sb band is replaced with an unoccupied Sn band above E_F. (c) Calculation of the band structure of CsV_3Sb_4Sn where one Sn has been substituted at a Sb site outside of the kagome plane (Sb2). A strong reconstruction of many bands can be observed, in particular near K, H, and $K - \Gamma$.

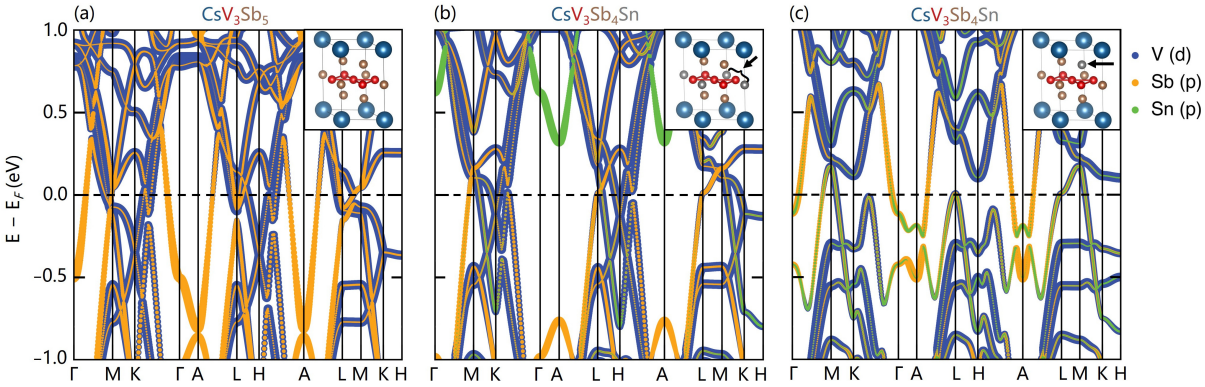

Figure 4.9: Colorized bands from DFT calculations show the orbital contributions from V, Sb, and Sn. (a) The Γ pocket in CsV_3Sb_5 is from the Sb p_z orbitals. (b) However, the fully substituted structure with Sn in the Sb1 kagome plane site arises from the Sn p_z orbitals. (c) Calculations of Sn substituted in the Sb2 out of plane site show a mix of Sb and Sn contribution to the Γ pocket.

superconductivity in CsV_3Sb_5 at least partially relies on the Sb p_z–derived orbitals, and aligns with results of earlier pressure studies. [112]

At smaller Sn-doping levels, the observation of an intermediate peak in T_C demon-

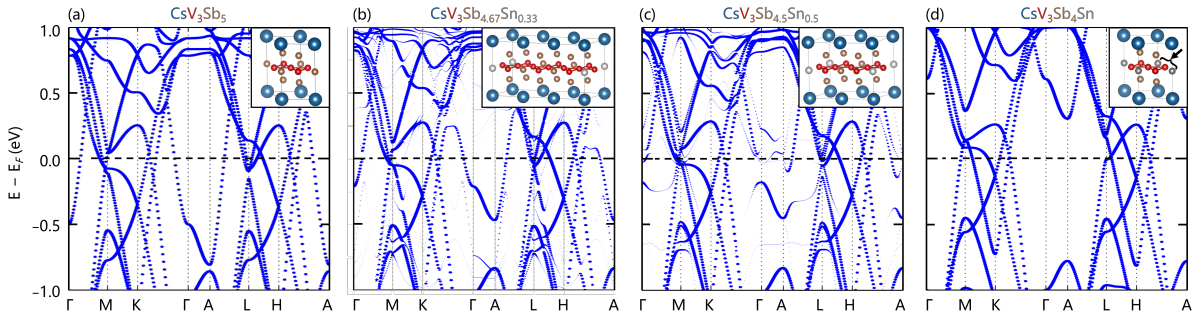

Figure 4.10: Supercell DFT calculations for $x = 0.33$ and 0.5 show the evolution of bands as Sn content is increased. The Γ pocket lifts through E_F by $x = 0.5$ while the van Hove singularity at the M–point crosses E_F by $x = 1$.

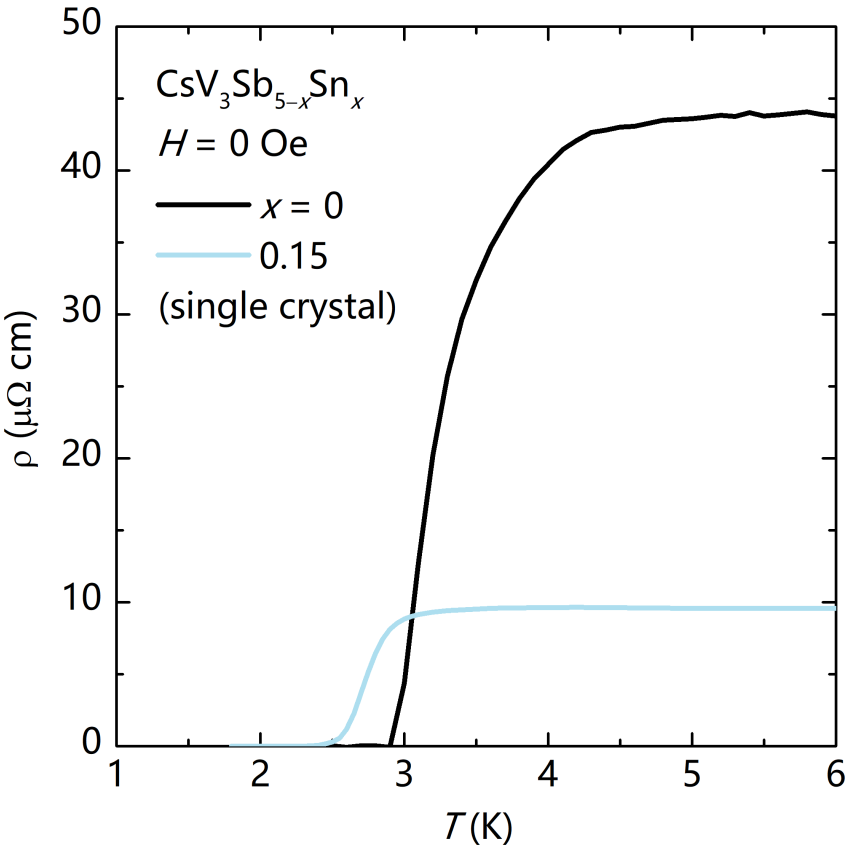

Figure 4.11: Resistivity data on single crystal $CsV_3Sb_{4.85}Sn_{0.15}$ complements powder resistivity data and shows no broadening in the superconducting transition.

strates a complex interplay between the Sb-states at Γ and the V d–states driving the CDW order. Supercell calculations show a rather mild shift in the M–point vHs from roughly -0.072 eV below E_F for $x = 0$ to -0.047 eV for $x = 0.33$ and -0.042 eV for

$x = 0.5$, prior to shifting 0.083 eV above E_F in $x = 1$. The small shift in the expected energies of the vHs toward E_F under mild $x = 0.05$ substitution fails to explain the rapid suppression of the CDW state at this doping, suggesting a complicated balance of energy scales underpinning the CDW state. This is consistent with the rapid suppression of the CDW state under hydrostatic pressure;[54, 55] however the two SC domes apparent under hole doping seem distinct from those realized under pressure. Superconductivity in crystals nominally doped between the SC domes retains a sharp transition as seen in Figure 4.11, unlike the weak SC observed in pressure studies. Further work exploring the distinctions between pressure (pushing vHs away from E_F) and hole doping (pulling vHs toward E_F) is required to fully explore the parallels between the hole doping and pressure driven phase diagrams.

4.5 Results and discussion of $KV_3Sb_{5-x}Sn_x$ and $RbV_3Sb_{5-x}Sn_x$

$AV_3Sb_{5-x}Sn_x$ all adopt the parent hexagonal $P6/mmm$ structure at room temperature, with the V atoms making up an ideal kagome network. As discussed in the previous section, ^{121}Sb nuclear quadrupole resonance (NQR) studies on $CsV_3Sb_{5-x}Sn_x$ have shown that the Sn atoms preferentially occupy the Sb1 sublattice site in the kagome plane [106]. Due to the similarity in structure in all of the AV_3Sb_5 compounds, we assume that the Sn atoms occupy the Sb1 sublattice for A = K, Rb as well. For $KV_3Sb_{5-x}Sn_x$, polycrystalline samples were found to be single phase for $x \leq 0.25$, while for $RbV_3Sb_{5-x}Sn_x$, polycrystalline samples were single phase for $x \leq 0.7$, at which point the limit of the solid solution was reached and secondary phases were observed in both families (Fig. 4.12 and Fig. 4.13).

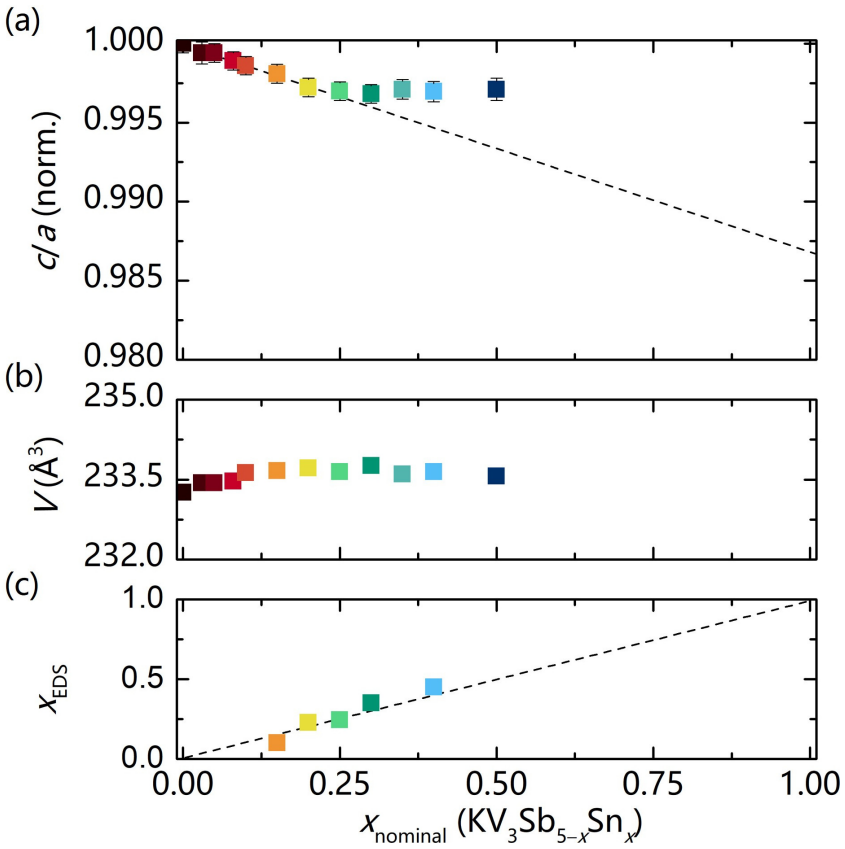

Figure 4.12: (a) Sn integration into $KV_3Sb_{5-x}Sn_x$ causes the c/a ratio to decrease, and the solubility limit of Sn is $x \approx 0.25$, at which point the c/a ratio deviates from the linear trend. (b) The volume does not change with the integration of Sn. (c) For samples with concentrations above the EDS sensitivity threshold, nominal Sn and measured Sn content in $KV_3Sb_{5-x}Sn_x$ agree. Error bars are shown unless they are smaller than associated point size; different colors correspond to sample composition and are consistent throughout the figures.

Powder diffraction data were fitted using the Pawley method to study changes in unit cell as a function of Sn content. Similar to the changes observed in $CsV_3Sb_{5-x}Sn_x$, a increases as c decreases with increasing Sn content in both A = K, Rb as seen in Figures 4.12(a) and 4.13(a), while the volume is independent of Sn content (Fig. 4.12(b) and 4.13(b)). The solubility limit of Sn is clearly reached once the c/a ratio deviates from its linear trend ($x \approx 0.30$ for $KV_3Sb_{5-x}Sn_x$ and $x \approx 0.70$ for $RbV_3Sb_{5-x}Sn_x$), and a secondary phase emerges in the powder diffraction data. These secondary phases can

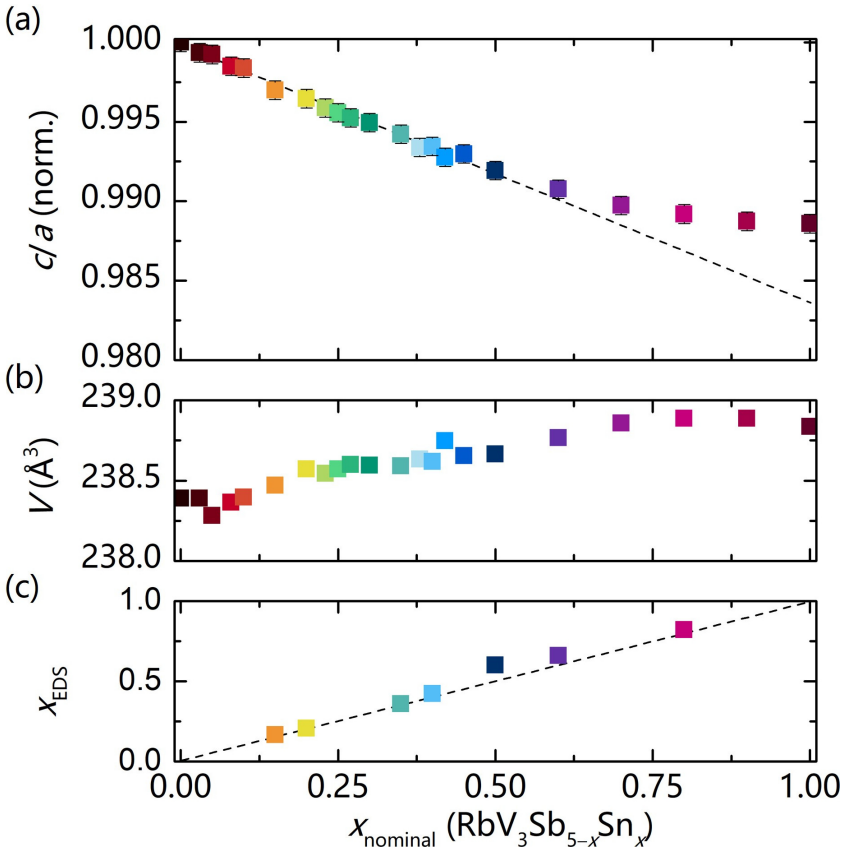

Figure 4.13: (a) The solubility limit of Sn in $RbV_3Sb_{5-x}Sn_x$ is a bit higher than for A = K, at $x \approx 0.70$. (b) The volume does not change with increased Sn content. (c) Nominal Sn and measured Sn content *via* EDS agree. Error bars are shown unless they are smaller than associated point size; different colors correspond to sample composition and are consistent throughout the figures.

be seen in Figure 4.14, but could not identified due to the small amount present. EDS was performed on samples with a critical Sn content to confirm the nominal Sn content (Fig. 4.12(c) and 4.13(c)).

Single crystal KV_3Sb_5 has a superconducting T_C of 0.93 K.[43] Here, the T_C of polycrystalline KV_3Sb_5 is lower than 1.8 K, the lowest achievable temperature on the MPMS, but as Sn was incorporated, the superconducting transition temperature increases and can be detected by $x = 0.03$. Figure 4.15(a) shows the evolution of the superconducting transition up to $x = 0.25$, where T_C is at a maximum of 4.37 K. Beyond this Sn content,

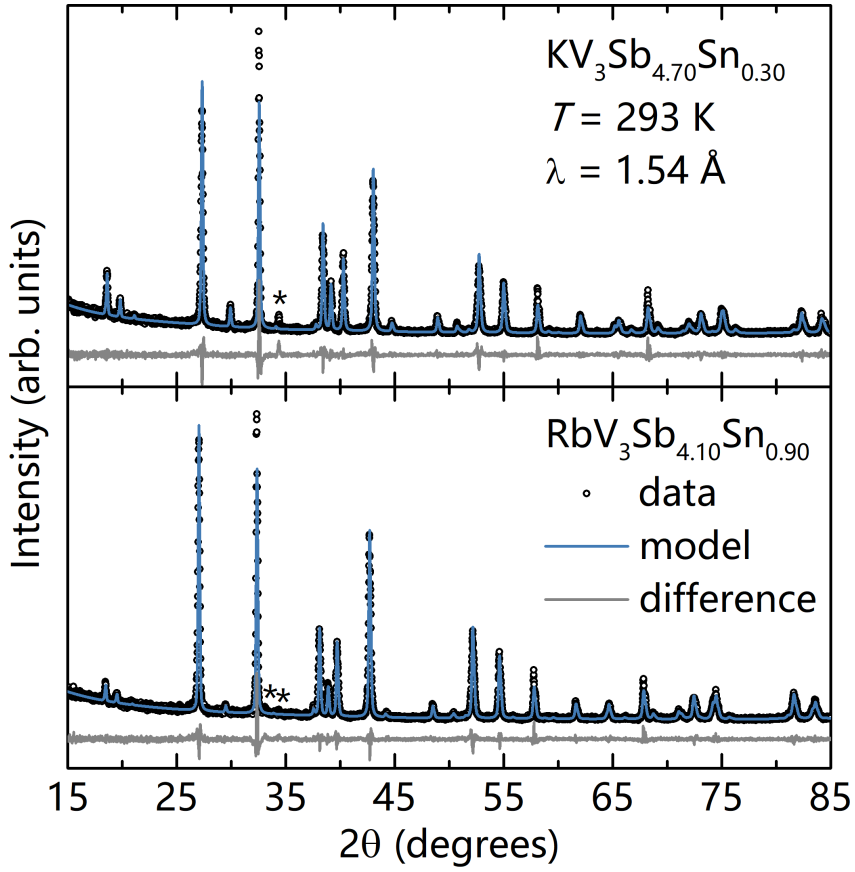

Figure 4.14: Pawley fits of powder XRD data taken at 293 K with a wavelength of 1.54 Åof $KV_3Sb_{4.70}Sn_{0.30}$ and $RbV_3Sb_{4.10}Sn_{0.90}$ are shown, with the secondary phases marked with asterisks (*). A secondary phase appears at around 34° 2θ for $KV_3Sb_{5-x}Sn_x$. In $RbV_3Sb_{5-x}Sn_x$, the secondary phase appears with two smaller peaks at around 33° and 34° 2θ.

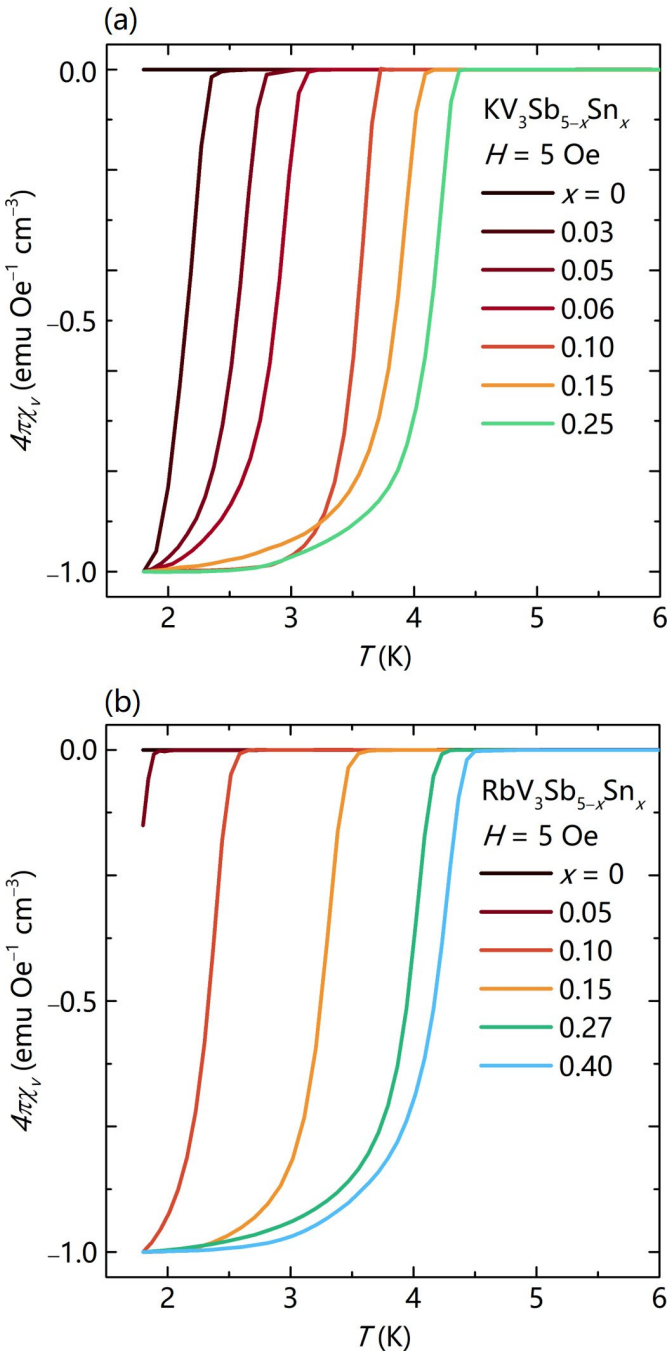

Figure 4.15: (a) The superconducting T_C of $KV_3Sb_{5-x}Sn_x$ measured under a field of $H = 5$ Oe systematically shifts to higher temperature in compositions up to $x = 0.25$. The superconducting fraction is normalized to account for errors in mass and packing fraction so all data have a minimum of -1, the theoretical minimum. (b) These transition temperatures can be compared to the superconducting T_Cs of $RbV_3Sb_{5-x}Sn_x$ measured under a field of $H = 5$ Oe, which also systematically shift to higher temperature in compositions up to $x = 0.40$.

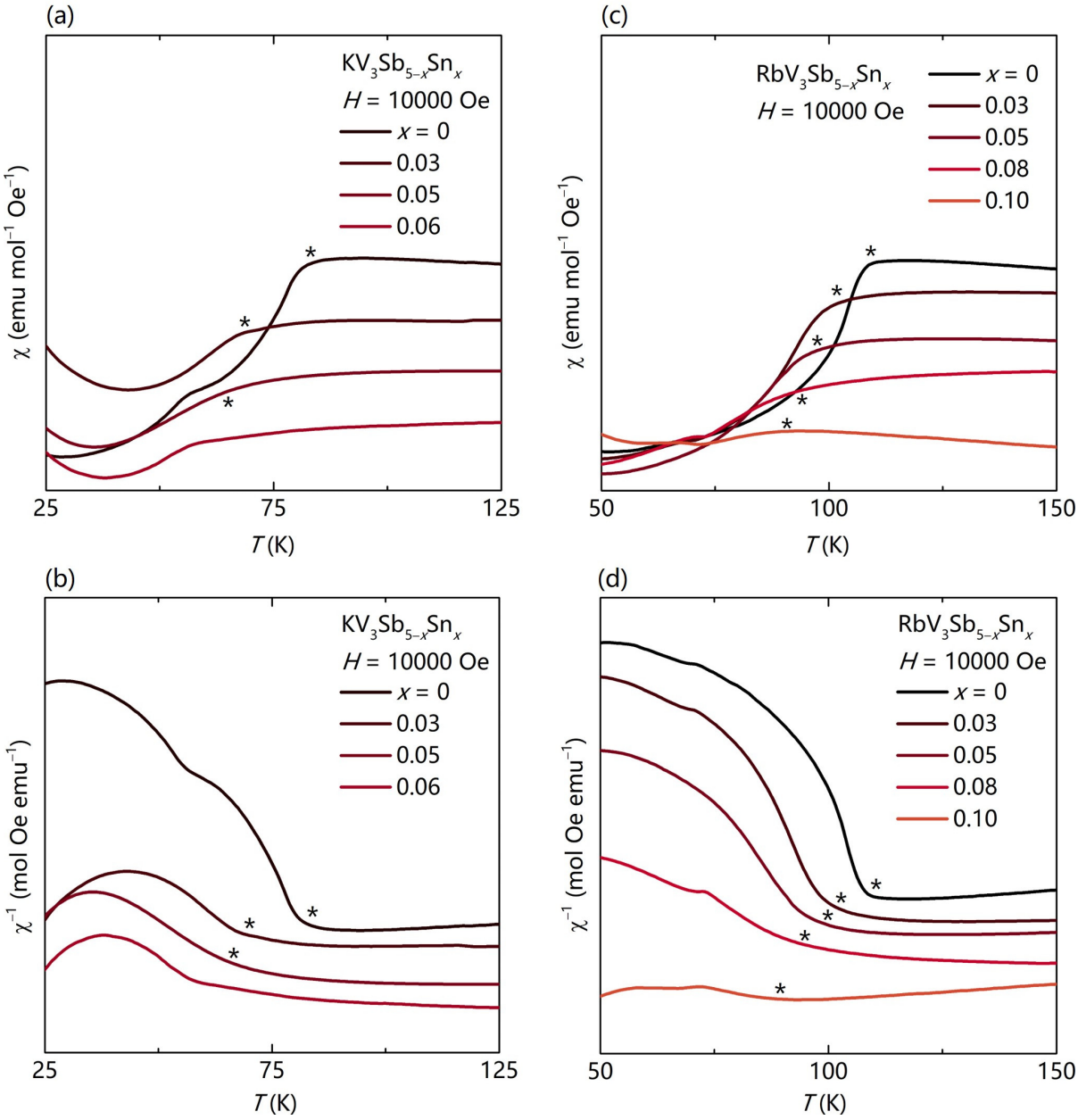

Figure 4.16: (a) Temperature dependent susceptibility of $KV_3Sb_{5-x}Sn_x$ shows the CDW transition decreasing in temperature and intensity with increasing Sn content. The transition in $x = 0.06$ around 60 K is a feature from the instrument, and is present in all samples with a low susceptibility signal. (b) $1/\chi$ *vs.* T for compositions $x \leq 0.05$ in $KV_3Sb_{5-x}Sn_x$ show the CDW T^* decreases from 84 K to 65 K and disappears for $x > 0.05$. (c) Temperature dependent susceptibility of $RbV_3Sb_{5-x}Sn_x$ shows the evolution of the CDW transition with increasing Sn content. (d) $1/\chi$ for compositions $x \leq 0.10$ in $RbV_3Sb_{5-x}Sn_x$ show the CDW T^* decreases and eventually disappears for $x > 0.10$. All CDW transitions are marked with an asterisk (*) and all magnetic data were collected under zero field cooled conditions.

a secondary phase appears, so an eventual suppression of superconductivity is not observed within the solid solution of $KV_3Sb_{5-x}Sn_x$. RbV_3Sb_5 shows similar behavior, with undoped crystals showing a T_C of 0.92 K.[46] Again, although the superconducting transition for RbV_3Sb_5 cannot be detected with an MPMS, by $x = 0.05$ the transition appears at 1.93 K and increases to a maximum of 4.5 K for $x = 0.40$, as seen in Figure 4.15(b). For $x > 0.40$, T_C decreases to 3.55 K until a clear secondary phase appears. All of the superconducting volume fractions are approximately $4\pi\chi_v \approx -1$ and are normalized to -1 for ease of comparison; fractions that deviate slightly from this ideal value can be attributed to errors in packing density. Measurements were taken in zero field cooled conditions.

The CDW T^* was determined by looking at the inflection point of χ^{-1} *vs.* T, as marked by asterisks (*) in Figure 4.16. Polycrystalline KV_3Sb_5 as observed here has a T^* of 84 K, which is in good agreement with reported CDW transition temperatures of $\approx$ 80 K in crystals.[40] Using this metric, the CDW transition is quickly suppressed with increasing hole doping, decreases to 65 K by $x = 0.05$, and is fully suppressed by $x = 0.06$ (Fig. 4.16(a,b)). In RbV_3Sb_5, the CDW T^* using the same metric is $\approx$ 109 K, similar to the literature reported value.[39] The CDW is quickly suppressed to 90 K for $x = 0.10$, and additional Sn incorporation causes the CDW to be fully suppressed and undetectable *via* magnetization (Fig. 4.16(c,d)). In both systems, the CDW transition is fully suppressed with much less Sn content than that required to reach the peak of the superconductivity dome, suggesting that the interplay between superconductivity and CDW is different in A = K, Rb than in CsV_3Sb_5, where the CDW persists through the peak of the first superconducting dome.

Electrical resistivity measurements of samples near the superconducting peak concentrations are shown in Figure 4.17. The superconducting states are clearly observed

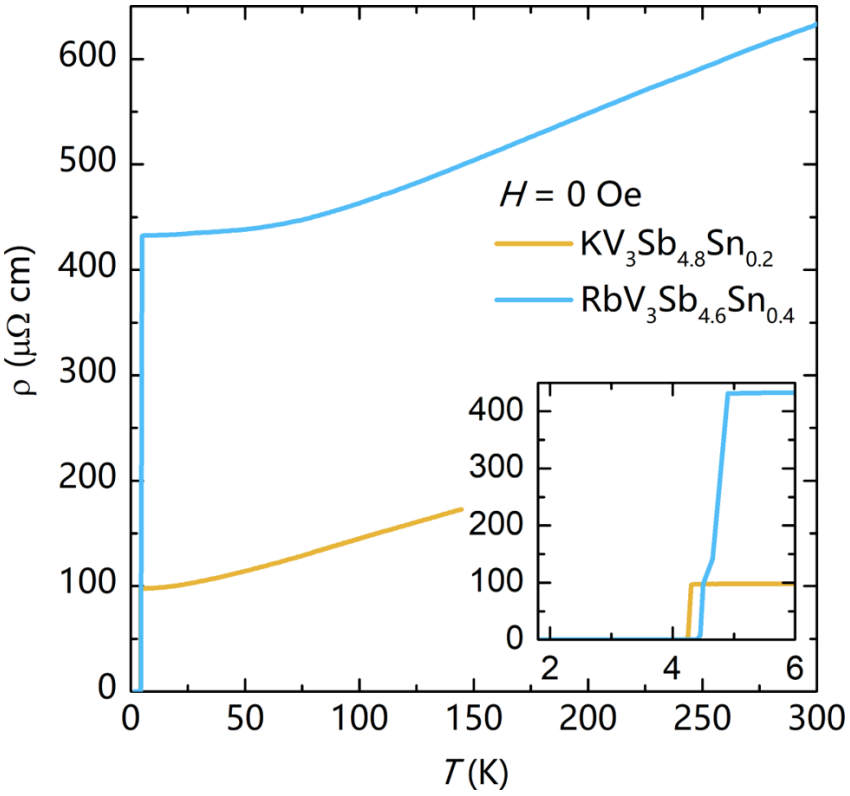

Figure 4.17: Temperature–dependent resistivity data taken on pressed and sintered pellets of polycrystalline $KV_3Sb_{4.8}Sn_{0.2}$ and $RbV_3Sb_{4.6}Sn_{0.4}$ confirm the T_C transitions and lack of CDW transitions for these higher Sn content samples.

as zero–resistivity conditions and the transitions at 4.25 K for $KV_3Sb_{4.80}Sn_{0.20}$ and 4.4 K for $RbV_3Sb_{4.60}Sn_{0.40}$ agree well with those seen in the magnetization data, while signatures of CDW transitions are also not present. Consistent with $CsV_3Sb_{5-x}Sn_x$, the residual resistance increases in $RbV_3Sb_{5-x}Sn_x$ and $KV_3Sb_{5-x}Sn_x$ under Sn–substitution while T_C increases.

The effects of Sn substitution on SC and CDW orders in $KV_3Sb_{5-x}Sn_x$ and $RbV_3Sb_{5-x}Sn_x$ are summarized in Figure 4.18. In both systems, the CDW ordering temperature is rapidly suppressed with small levels of hole doping and fully disappears before the maximum superconducting transition temperatures. With the exception of the solubility limit of Sn in each structure, the two phase diagrams are qualitatively similar.

Due to size considerations, the solubility limits of Sn in KV_3Sb_5 and RbV_3Sb_5 are much lower than in CsV_3Sb_5. However in all of these systems, the changes in electronic structure for the compositions of interest can be extrapolated by computing band structures of substitution one Sb atom for an Sn atom within the kagome plane and out of the kagome plane. Figure 4.19(a) and (d) shows the band structure of undoped KV_3Sb_5 and RbV_3Sb_5, respectively, with the range of achievable Fermi levels with the loss of 1 electron per unit cell indicated in gray. Figure 4.19(b) and (e) show a hypothetical structure where the Sb1 lattice is fully substituted for Sn. The shifts in band structure are similar to those seen in CsV_3Sb_4Sn, with the Γ pocket and M–point vHs lifted above the Fermi level. Band structures for Sn substituted within the Sb2 sublattice are plotted in Figure 4.19(c) and (f) and show significant reconstructions at multiple points, including K, L, and H.

Given the close structural and electronic properties across the AV_3Sb_5 series, the difference in the hole doping phase diagrams of KV_3Sb_5 and RbV_3Sb_5 relative to CsV_3Sb_5

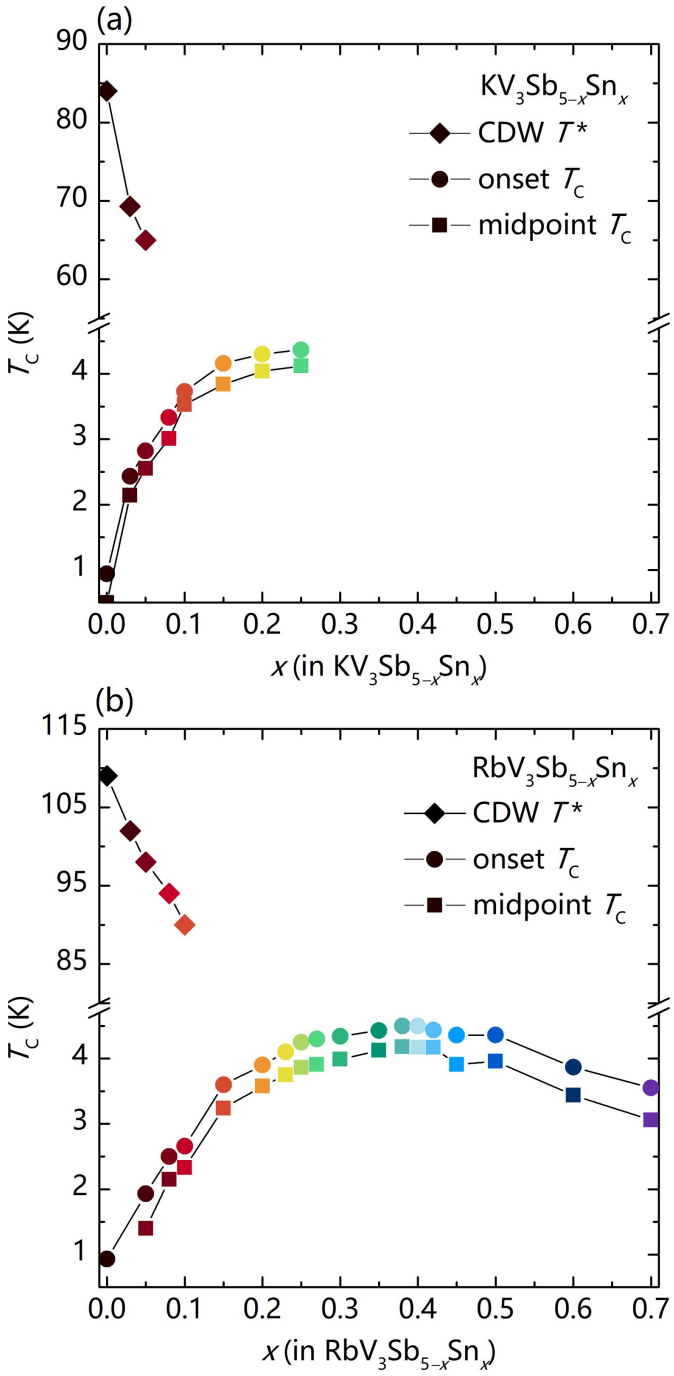

Figure 4.18: The progression of superconducting T_C and CDW order T^* is plotted as a function of Sn composition for $KV_3Sb_{5-x}Sn_x$ and $RbV_3Sb_{5-x}Sn_x$. (a) In $KV_3Sb_{5-x}Sn_x$, the solubility limit of Sn is reached before a full superconducting dome is achieved, but the suppression of CDW T^* is still fully realized. (b) $RbV_3Sb_{5-x}Sn_x$ shows a single superconducting dome before the solubility limit is reached, with an accompanying suppression of CDW order by $x = 0.1$.

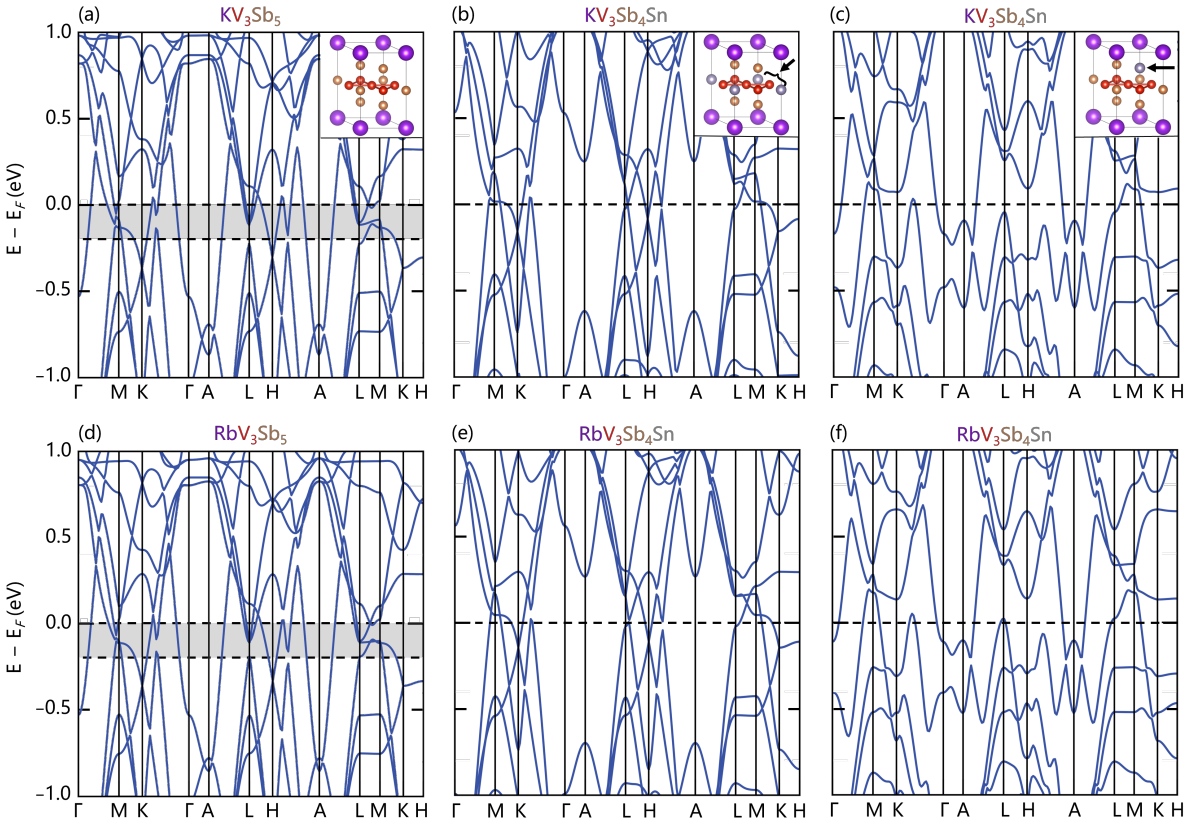

Figure 4.19: (a,d) DFT calculations for KV_3Sb_5 and RbV_3Sb_5 highlighting the allowable range of Fermi levels under the rigid band approximation for substitution of one Sn atom per formula unit (one electron less Fermi energy). (b,e) Calculation for a hypothetical structure where one Sn has been substituted within the kagome plan (Sb1 sublattice). The majority of the electronic structure is preserved as KV_3Sb_5 and RbV_3Sb_5, except the Γ pocket and M–point van Hove singularities which have been shifted far above and may contribute to the changing observable properties. (c,f) Calculation for a hypothetical structure where one Sn has been substituted out of the kagome plane (Sb2 sublattice). Here a strong reconstruction of many bands can be observed, in particular near K, H, and $K - \Gamma$.

is anomalous. The changes in band structure for Sn substitution on the Sb1 sublattice in KV_3Sb_4Sn and RbV_3Sb_4Sn at first sight, appear to be very similar to those in CsV_3Sb_4Sn. However, subtle differences are nevertheless present and potentially lead to distinct electronic phase diagrams. A closer examination of the saddle points around M reveals that the irreducible representations of the two points are not the same for A = K, Rb and Cs.[105, 113] As a consequence of the saddle point inversions, bands cross near E_F in CsV_3Sb_5 but not in KV_3Sb_5. This may play a role in the nature of the CDW states stabilized, whose proximity to one another may modify SC in unique ways.

One unifying theme between doping and pressure studies of AV_3Sb_5 is the similarity of two SC domes present uniquely in CsV_3Sb_5. If one envisions either pressure/doping empirically as a perturbation that simply destabilizes CDW order, then the data suggest that CsV_3Sb_5 hosts a CDW state distinct from the other two variants. In this scenario, there is a transition between CDW states within the phase diagram of CsV_3Sb_5 that is naively absent in KV_3Sb_5 and RbV_3Sb_5.

While the details of the intermediate states differ between pressure and hole doping studies, investigations of the parent CDW order in AV_3Sb_5 have shown differences between A = Cs and A = Rb/K. The out–of–plane modulation for Cs is four times that of K,[40, 48] and the in–plane structure of the CDW state in CsV_3Sb_5 hosts both star-of-David and tri–hexagonal character,[48, 50, 114] a pattern seemingly not present in the other variants. Given these differences, one possibility is a doping–induced transition from an (L, L, L)–type order to an (M, L, L)–type of order upon doping CsV_3Sb_5 [115] that is not present in the other two compounds. Future scattering studies across the carrier-tuned phase diagrams of these systems will be required to fully explore any potential crossover.

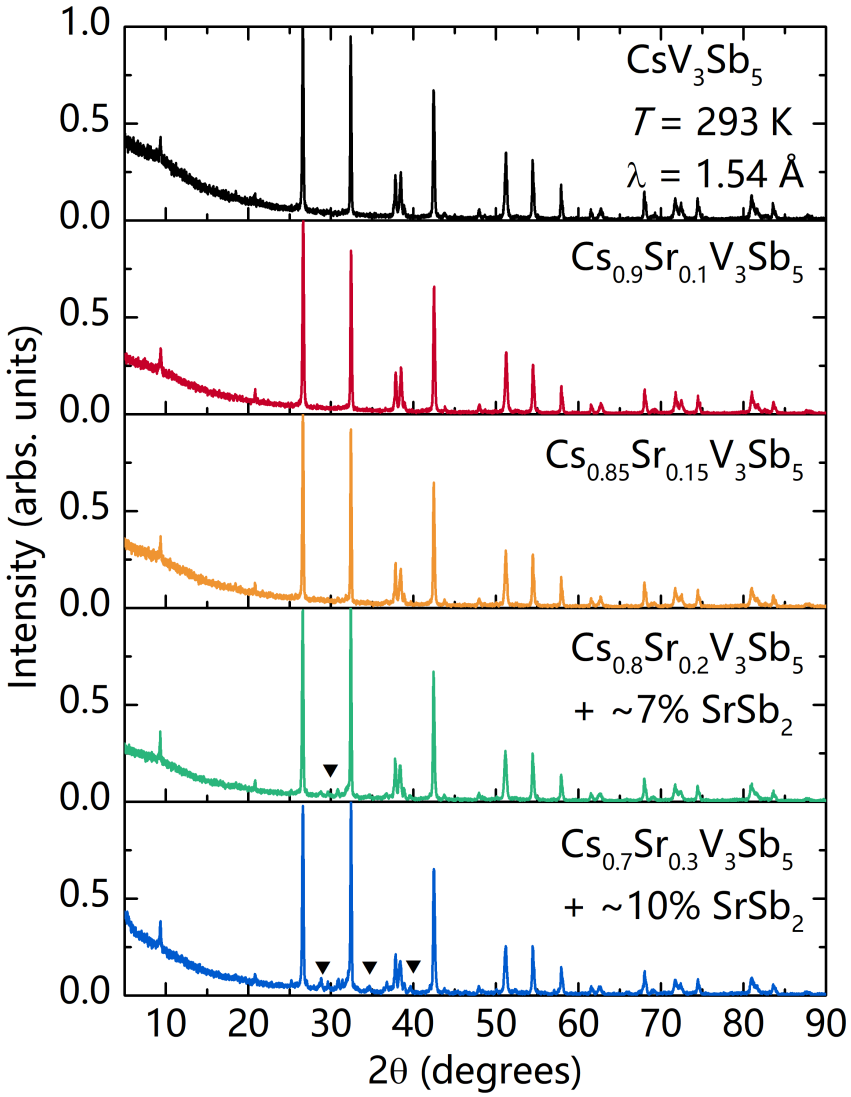

Figure 4.20: Powder X–ray diffraction data acquired at $T = 293\,\mathrm{K}$ of $Cs_{1-x}Sr_xV_3Sb_5$ shows a secondary phase identified as $SrSb_2$ emerging by $x = 0.2$.

4.6 Additional doping synthesis

In addition to Sn–substitution in CsV_3Sb_5, other substitutions were attempted, including Pb in the Sb site and Sr in the Cs site, both of which should hole dope the structure. The syntheses of these potential dopants followed closely to the Sn–doped polycrystalline synthesis. To make the screening process for dopants efficient, a sequential synthesis was performed. Initial batches of powder with small amounts of dopant were first ball milled, and stoichiometric amounts of dopant were added to some of the ball milled powder to produce higher doped samples (for example, Sr was added to ball milled $Cs_{0.9}Sr_{0.1}V_3Sb_5$), and then all samples were annealed in a two–step process.

Powder X–ray diffraction showed that by $CsV_3Sb_{4.9}Pb_{0.1}$, a secondary phase was present, while up to 20% of Cs sites could be replaced by Sr ($Cs_{0.8}Sr_{0.2}V_3Sb_5$), at which point a secondary phase of $SrSb_2$ appeared (Figure 4.20). However, the volume and lattice parameters of all Pb and Sr doped samples remained constant, suggesting that very little, if any, Pb and Sr were entering the crystal structures.

The superconducting and CDW transitions were determined for these doped samples *via* temperature dependent magnetization. In both doping instances, the superconducting T_C appeared to shift to lower temperatures with the inclusion of more Sr or Pb, while the CDW transition did not change in temperature or magnitude. However, different superconducting T_C's of CsV_3Sb_5 have been reported, so it is possible that the slight shifts in T_C observed in these doping studies arose strictly from disorder induced by Sr or Pb. Some sample SC and CDW data for Sr doped CsV_3Sb_5 is shown in Figure 4.21.

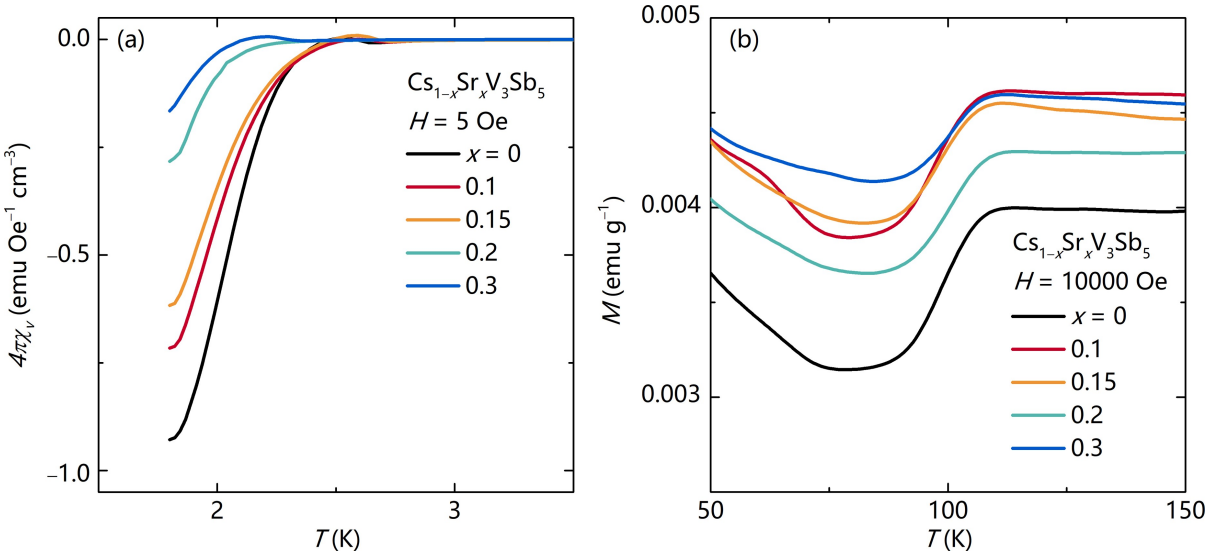

Figure 4.21: Temperature–dependent magnetization of $Cs_{1-x}Sr_xV_3Sb_5$ shows (a) the decreasing superconducting fraction with increasing Sr content and (b) no change in the CDW transition.

4.7 Conclusion

Here, the hole doping phase diagrams of AV_3Sb_5 for A = K, Rb, and Cs *via* Sn–substitution were explored. Hole doping realized *via* chemical substitution of Sn into CsV_3Sb_5 results in a complex electronic phase diagram featuring two SC domes, one that coexists with CDW order and a second that appears following the suppression of the CDW state. Unconventional superconductivity has been predicted for fillings slightly away from the vHs [36]. The peak in T_C prior to the suppression of CDW order and the subsequent, second peak in T_C following the complete suppression of the CDW state motivates deeper theoretical studies into how the Sb p_z states intertwine with both CDW order SC in these materials.

The solubility of Sn within the AV_3Sb_5 structure varies with A–site cation size with A = K having the smallest solubility and A = Cs having the largest. Prior to reaching the solubility limit, hole doping achieved *via* substitution of Sn on Sb sites in KV_3Sb_5 and

RbV_3Sb_5 reveals similar phase diagrams consisting of a single SC dome and rapidly suppressed CDW order. This contrasts the double dome observed in CsV_3Sb_5 and suggests a distinct parent CDW state for the latter. Our results demonstrate that small changes in the electronic structure achieved through carrier doping can have dramatic impacts on SC and CDW orders in CsV_3Sb_5 and provide a elegant chemical means to tune the competition between these states in the new AV_3Sb_5 class of kagome superconductors.

Chapter 5

Summary

In this dissertation we explore the effects that subtle changes in structure can have on magnetic and electronic properties. $AlFe_2B_2$ exhibits clear strong magnetostructural coupling, where the subtle but significant structural changes through the magnetic transition temperature causes a strong magnetocaloric effect. Understanding the role of magnetostructural coupling in second order transition magnetocalorics like $AlFe_2B_2$ is important to discover other potential magnetocaloric materials that can be used in large scale solid state refrigeration applications.

Meanwhile, the magnetostructural coupling was not explored in MnPdGa, but a distinction in DFT calculated structures of MnPdGa *vs.* MnPtGa hint at the differences in magnetocaloric performance between the two compounds. While both adopt the same crystal structure, MnPdGa shows an enhanced MCE compared to MnPtGa. DFT calculations suggest that a canted AFM phase is more favorable in MnPtGa, creating AFM domain walls that decrease its low temperature moment compared to MnPdGa. Near both materials' T_Cs, MnPdGa has a lower energy FM state, leading to an enhanced moment and a larger MCE. Understanding and identifying these subtle differences be-

tween materials that adopt the same crystal structure and contain similar atoms can allow us to modify other materials to exhibit certain properties or be comprised of more desirable elements.

The AV_3Sb_5 kagomes are sensitive to electron count and element substitutions. This structure does not form with *A* sites other than K, Rb, and Cs and is resistant to having all of its V or Sb sites replaced with another element. The reason for this is still unclear, since in terms of size and electron count, there should be many ways to modify the composition of the 135 kagome structure. Modifying the elements of this kagome structure was explored using different stoichiometries of K, Ca, Ba, V, and Te. Te compounds usually have very similar phase diagrams to Sb analogues and is therefore an excellent candidate to try when partially or fully substituting Sb. Since the 135 kagomes are metals, charge balancing should not matter, so Ca and Ba were both attempted as potential *A* site cations.

Another reason ternaries of $K_xV_yTe_z$, $Ca_xV_yTe_z$, and $Ba_xV_yTe_z$ were explored was due to the existence of binaries of (K, Ca, Ba)$_x$Te$_z$ and V$_y$Te$_z$,[116–119] and because ternaries of these elements had not been reported before according to the Materials Project. Representative binary phase diagrams of V–Te and K–Te are shown in Figure 5.1; many binaries of both exist within reasonable synthesis temperatures. Perhaps most importantly is that many known ternaries are composed of known binaries, so ternaries with the composition (K, Ca, Ba)$_x$V$_y$Te$_z$ should be reasonably stable.

Syntheses of K_2VTe_2, K_2VTe_3, $K_2V_3Te_5$, $CaVTe_2$, and $BaVTe_2$ were attempted in an argon glove box by weighing out stoichiometric quantities of elemental starting materials, ball milling in a tungsten carbide vial for 60 minutes, and annealing in an alumina crucible in a sealed silica tube. K_2VTe_2, K_2VTe_3 and $K_2V_3Te_5$ were annealed at 550 °C for 36 hours and all five samples were also annealed at 450 °C for 48 hours. The sam-

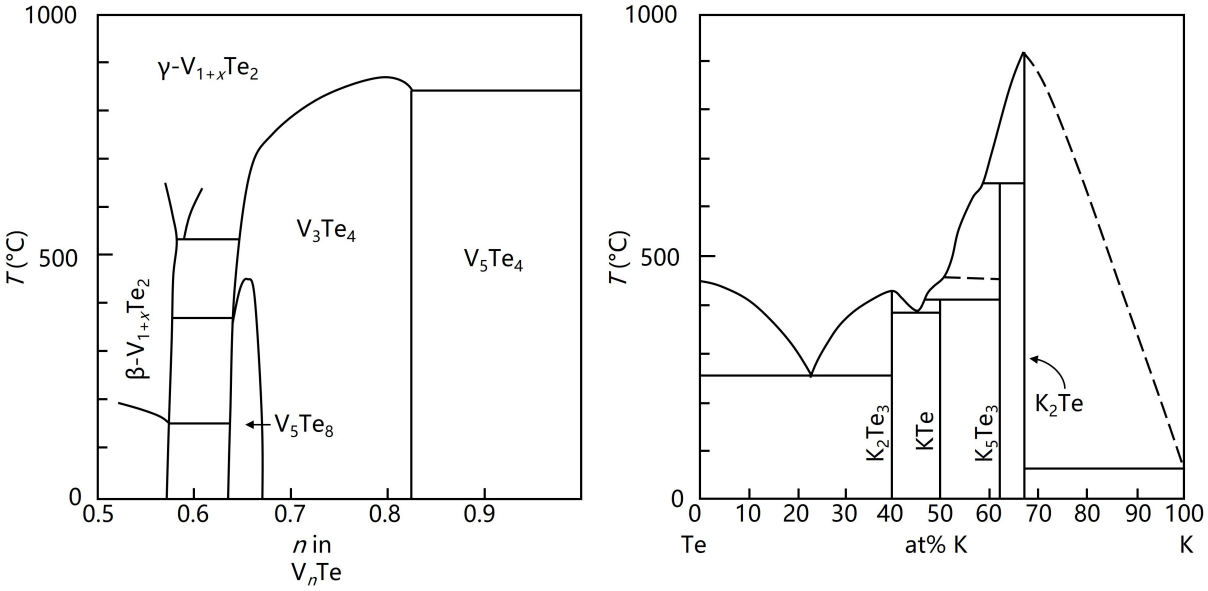

Figure 5.1: V_nTe binary figure adapted from [116]; KTe binary figure adapted from [117]. These phase diagrams show that several stable binaries of V–Te and K–Te exist at ambient pressure below 1000 °C.

ples were then gently ground with an agate mortar and pestle in an argon glove box and then powder X–ray (pXRD) data were collected on a Panalytical Empyrean powder diffractometer equipped with a PIXcel 1D detector.

All K samples were either moisture or air sensitive with both annealing temperatures. For the 550 °C anneal, the samples were very difficult to take out of the crucibles and grind. Within the time the samples were exposed to air for the pXRD, they clearly absorbed some moisture and turned from black to a lighter gray (or black mixed with white). The resulting pXRD patterns most closely matched a mixture of V_3Te_4 and Te. The sensitivity to moisture in air suggested that the samples also had some form of unreacted K. The 450 °C anneal presented more difficulties, with K_2VTe_2 spontaneously lighting on fire upon contact with air during the pXRD prep and $K_2V_3Te_5$ popping the silica tube. Lastly, K_2VTe_3 did not show a difference with the 550 °C anneal; the sample was still moisture or air sensitive and seemed like a mix of V_3Te_4, Te, and K. The

$CaVTe_2$ and $BaVTe_2$ were only annealed at 450 °C for 48 hours. The samples were not air or moisture sensitive but seemed to only make binaries of V_yTe_z (possibly V_3Te_4) and CaTe or BaTe.

Regardless, the successful inclusion of Sn on the in–plane Sb site allows for new insight into the electronic structures of AV_3Sb_5 and the subtle differences between A = Cs *vs.* K and Rb. For example, with the Sn doping studies, it is even more clear now that the saddle points at the M–point in CsV_3Sb_5 are inverted compared to those in KV_3Sb_5 and RbV_3Sb_5. Slightly hole doping AV_3Sb_5 has pronounced effects on the ordering temperatures and resultant structures (discussed more in Appendix B), emphasizing the importance of even naively minor structural and compositional changes to magnetic and electronic properties. Studies like these that carefully tune the electron count of a model system allow us to gain valuable insight about competing ordering phases and how to achieve a desired phase for further study.

Appendix A

$AlFe_2B_2$ refinement parameters from synchrotron X–ray diffraction data

Source	Advanced Photon Source 11-BM, Argonne National Laboratory
Temperature (K)	350.0
Wavelength (Å)	0.414581
Chemical formula	$AlFe_2B_2$
Crystal system	Orthorhombic
Space group (no.)	$Cmmm$ (65)
a (Å)	2.933883(5)
b (Å)	11.053024(18)
c (Å)	2.874618(5)
Volume (Å^3)	93.2189(3)
R_{wp}	9.243
R_{exp}	5.267

Table A.1: Conditions of synchrotron X–ray diffraction and refined crystal structure parameters.

	Wyckoff site	x	y	z	Occupancy
Al	$2a$	0	0	0	1.0063(12)
Fe	$4j$	0	0.353976(12)	0.5	1
B	41	0	0.20638(8)	0	1

Table A.2: Refined Wyckoff sites and atom positions of $AlFe_2B_2$.

	U_{11}	U_{22}	U_{33}	U_{12}	U_{13}	U_{23}
Al	0.0075(2)	0.00212(19)	0.00213(18)	0	0	0
Fe	0.00843(7)	0.00327(6)	0.00227(6)	0	0	0
B	0.0031(5)	0.0044(5)	0.0086(5)	0	0	0

Table A.3: Atomic displacement parameters (ADPs) of $AlFe_2B_2$ indicate that the obtained refinement parameters are within reason.

Appendix B

Preliminary single crystal growth and data of $CsV_3Sb_{5-x}Sn_x$

Chapter 4 explored the various changes observed in polycrystalline (powder) AV_3Sb_5 with partial Sn substitution on the Sb site. While polycrystalline samples are easier than single crystals to synthesize, single crystals can often give more insight into various properties. Single crystals allow more sophisticated measurements on homogeneous sample regions, such as single crystal X–ray, ARPES, and microscopy. Appendix A will give details about preliminary single crystal growth attempts as well as data about these crystals from collaborative projects.[114, 120]

B.1 Single crystal growth of $CsV_3Sb_{5-x}Sn_x$

Single crystal growth conditions of CsV_3Sb_5 were first reported by Ortiz *et al.*[39] $CsV_3Sb_{5-x}Sn_x$ crystal growth was attempted by a similar method and crystals with $x \leq 0.30$ were successfully synthesized, although with varying consistency. Elemental

Cs (liquid, Alfa 99.98%), V (powder, Sigma 99.9%), Sb (shot, Alfa 99.999%), and Sn (shot, Alfa 99.9999%) were weighed in stoichiometric quantities of $Cs_{20}V_{15}Sb_ySn_z$ and ball milled for 60 mins. The flux was packed into alumina crucibles and sealed under inert atmosphere in stainless steel tubes, then heated to 1000 °C at 200 °C per hour. The flux was kept at 1000 °C for 12 hours then cooled to 900 °C at 10 °C per hour, then slowly cooled to 500 °C at 2 °C per hour. The samples were then cooled to room temperature and crystals were extracted using isopropyl alcohol to remove the flux.[120] Crystals of varying Sn content and size were synthesized, although increased Sn incorporation correlated to smaller and thinner crystals.

In attempt to quantify the Sn content in the single crystals, a variety of techniques were used. The magnetic properties of the single crystals were first verified by mounting them onto a quartz paddle using GE varnish and measuring their temperature–dependent magnetization on the Quantum Design MPMS. The superconducting T_C and CDW T^* were matched with the phase diagram generated from the polycrystalline samples. EDS and X–ray photoelectron spectroscopy (XPS) were also performed on the crystals. However, since the spectra of Sb *vs.* Sn is hard to resolve in an EDS, it proved to not be a reliable technique, especially when trying to determine the differences between a few percent of Sn. These overlapping signals are not a problem in XPS, but there were some issues with the measured Cs and V content. Other reports of XPS on undoped CsV_3Sb_5 note that the Cs, V, and Sb peaks are present, but none of the spectra are clearly scaled and the stoichiometry determined from the XPS measurements are not reported.[58, 121] Therefore, to determine the Sn content, only the Sb:Sn ratio was considered for these XPS measurements. A combination of higher resolution EDS, counting defects *via* microscopy, and other techniques such as inductively coupled plasma (ICP) spectroscopy can be used in the future to more accurately quantify the

Sn content in single crystals.

B.2 High–resolution ARPES studies on $CsV_3Sb_{5-x}Sn_x$ single crystals

[1] Recently, Kang *et al.* performed an in–depth study on the microscopic 3–D charge order (CO) of single crystal AV_3Sb_5 using high–resolution angle–resolved photoemission spectroscopy (ARPES). By looking at the unusual splitting of kagome bands that occurs with 3–D CO, this study was able to show that the CDW order in CsV_3Sb_5 is distinct from that in KV_3Sb_5, RbV_3Sb_5, and Sn-doped CsV_3Sb_5. CDW ordered CsV_3Sb_5 is comprised of alternating SoD and TrH kagome layers (known as the *LLL* + *MMM* phase). Meanwhile, KV_3Sb_5, RbV_3Sb_5, and $CsV_3Sb_{5-x}Sn_x$ orders in the staggered TrH structure (*MLL* phase).[114] These results contrast with those reported before which claim that KV_3Sb_5 also adopts a SoD and TrH alternating structure.[49]

These difference found in CO further illustrates the distinction in electronic structures between CsV_3Sb_5 and other members in this kagome family. By understanding the exact structure of 3–D CO, other effects such as double–dome superconductivity in $CsV_3Sb_{5-x}Sn_x$ or the suppression of T_C in KV_3Sb_5 and RbV_3Sb_5 may be better understood. The additional understanding gained by studying single crystal $CsV_3Sb_{5-x}Sn_x$ cannot be underestimated: prior to these doped single crystals, it was assumed that CsV_3Sb_5 and its derivatives were intrinsically distinct to A = K, Rb. However, now with the successful growths of $CsV_3Sb_{5-x}Sn_x$ single crystals, additional insight of the

[1] The contents of this section first appeared in M. Kang, S. Fang, J. Yoo, B. R. Ortiz, Y. M. Oey, J. Choi, S. H. Ryu, J. Kim, C. Jozwiak, A. Bostwick, E. Rotenberg, E. Kaxiras, J. G. Checkelsky, S. D. Wilson, J. Park, and R. Comin, "Charge order landscape and competition with superconductivity in kagome metals," *accepted to Nature Materials*.

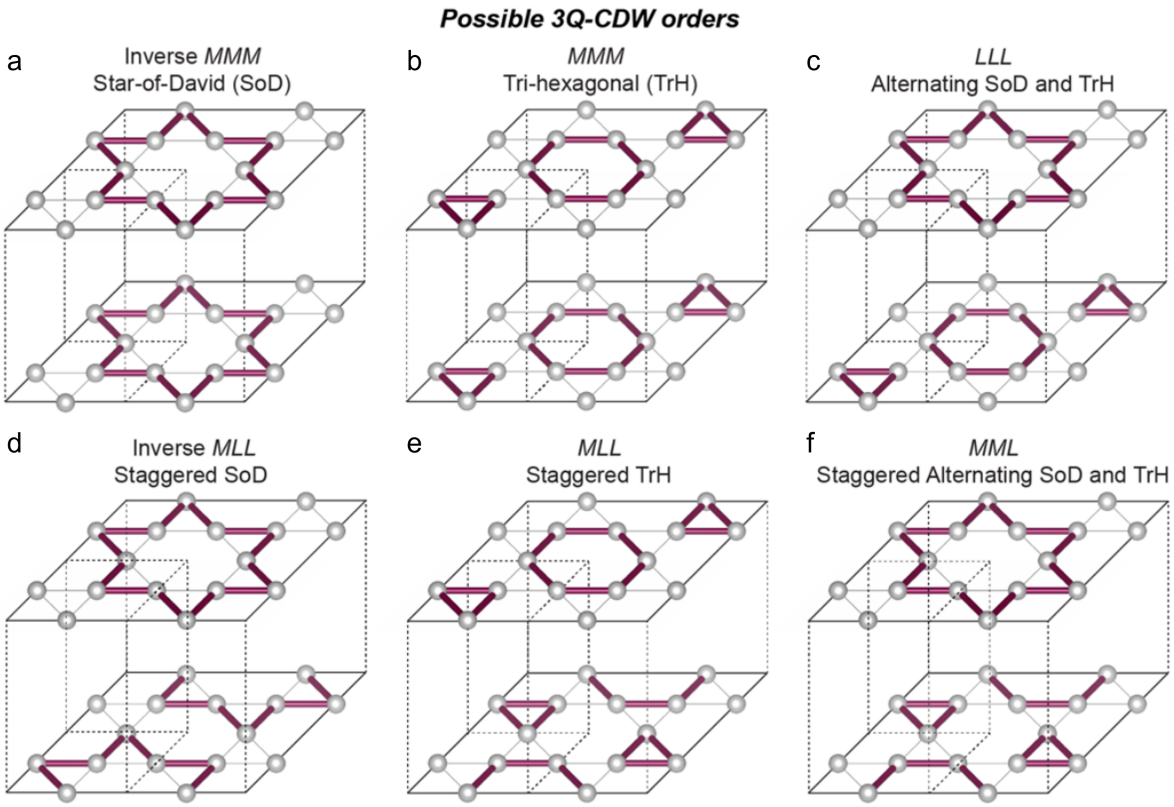

Figure B.1: Figure from [114]. Possible 3–D charge order structures are shown. CsV_3Sb_5 charge orders in the (a) inverse *MMM* and (b) *MMM* structures, which leads to the (c) *LLL* structure. KV_3Sb_5, RbV_3Sb_5, and $CsV_3Sb_{5-x}Sn_x$ orders in the (e) staggered TrH structure (*MLL* phase).

fragility of electronic structure with respect to doping and other compositional changes can be gained.

B.3 Single crystal X–ray diffraction of $CsV_3Sb_{5-x}Sn_x$

[2] Temperature–dependent synchrotron X–ray data of $CsV_3Sb_{5-x}Sn_x$ with $x = 0.025$ and $x = 0.15$ were collected at the ID4B (QM2) beamline at CHESS. The temperature was controlled by flowing cold helium gas across the sample and an incident X–ray with energy 26 keV was used. Data were taken in collaboration with Brenden Ortiz and Jacob Ruff. Data were analyzed by Linus Kautzsch.[120]

Parent CsV_3Sb_5 undergoes a $2 \times 2 \times 4$ supercell reconstruction of a modulation between SoD and TrH distortion modes below the CDW transition.[48, 50, 114] However, single crystal diffraction reveals that with even a small amount of Sn incorporation, the CDW transition changes from the parent structure. For $x = 0.025$, the in–plane 2×2 CDW order present in the parent compound is still present, but the interlayer correlations along the c–axis is dramatically shortened. The supercell for the doped CDW state is now $2 \times 2 \times 2$, with **q** vectors reminiscent of the CDW states in KV_3Sb_5 and RbV_3Sb_5 rather than CsV_3Sb_5. Upon further Sn incorporation past the first superconducting dome ($x = 0.15$), 3D CDW order disappears and incommensurate quasi–1D charge correlations form. These quasi–1D correlations suggest that the electronic rotational symmetry is broken as more holes are introduced to the structure.

Single crystal diffraction suggest that the charge correlations in $CsV_3Sb_{5-x}Sn_x$ are complex. These studies cannot be done with polycrystalline measurements, and grow-

[2] The contents of this section first appeared in L. Kautzsch, Y. M. Oey, H. Li, Z. Ren, B. R. Ortiz, R. Seshadri, J. Ruff, Z. Wang, I. Zeljkovic, and S. D. Wilson, "Incommensurate charge-stripe correlations in the kagome superconductor $CsV_3Sb_{5-x}Sn_x$," arXiv.

ing high–quality single crystals of hole–doped CsV_3Sb_5 is crucial to better understand the electronic structure and properties of these materials.

Bibliography

[1] A. Fert, V. Cros, and J. Sampaio. Skyrmions on the track. *Nat. Nanotechnol.* **8** (2013) 152–156. doi:10.1038/nnano.2013.29

[2] C. Hammond. *The basics of crystallography and diffraction*, volume 21. International Union of Crystal (2015).

[3] J. Hastings, W. Thomlinson, and D. Cox. Synchrotron X-ray powder diffraction. *J. Appl. Crystallogr.* **17** (1984) 85–95. doi:10.1107/S0021889884011043

[4] A. K. Cheetham and A. P. Wilkinson. Synchrotron X-ray and Neutron Diffraction Studies in Solid-State Chemistry. *Angew. Chem. Int. Ed.* **31** (1992) 1557–1570. doi:10.1002/anie.199215571

[5] H. M. Rietveld. A profile refinement method for nuclear and magnetic structures. *J. Appl. Crystallogr.* **2** (1969) 65–71. doi:10.1107/S0021889869006558

[6] G. Pawley. Unit-cell refinement from powder diffraction scans. *Journal of Applied Crystallography* **14** (1981) 357–361. doi:10.1107/S0021889881009618

[7] H. Meyers. *Introductory solid state physics*. CRC press, 2 edition (1997).

[8] S. Blundell. Magnetism in condensed matter (2003).

[9] N. Ashcroft and N. Mermin. *Solid State Physics*. Saunders College, 1 edition (1976).

[10] M. Dresselhaus. Solid State Physics part III Magnetic Properties of Solids. *Lecture Notes (Massachusetts Institute of Technology, Cambridge, MA)* (1999).

[11] A. Lichtenstein. Magnetism: From Stoner to Hubbard. *Emergent Phenomena in Correlated Matter* (2013).

[12] L. J. de Jongh. *Magnetic properties of layered transition metal compounds*, volume 9. Springer Science (2012).

[13] G. Brown. Magnetic heat pumping near room temperature. *J. Appl. Phys.* **47** (1976) 3673–3680. doi:10.1063/1.323176

[14] V. K. Pecharsky and K. A. Gschneidner, Jr. Giant Magnetocaloric Effect in $Gd_5(Si_2Ge_2)$. *Phys. Rev. Lett.* **78** (1997) 4494–4497. doi:10.1103/PhysRevLett.78.4494

[15] V. Franco, J. Blázquez, J. Ipus, J. Law, L. Moreno-Ramírez, and A. Conde. Magnetocaloric effect: From materials research to refrigeration devices. *Prog. Mater. Sci.* **93** (2018) 112–232. doi:10.1016/j.pmatsci.2017.10.005

[16] W. Giauque and D. MacDougall. Attainment of Temperatures Below 1° Absolute by Demagnetization of $Gd_2(SO_4)_3$ $8H_2O$. *Phys. Rev.* **43** (1933) 768. doi:10.1103/PhysRev.43.768

[17] C. Zimm, A. Jastrab, A. Sternberg, V. Pecharsky, K. Gschneidner, M. Osborne, and I. Anderson. Description and performance of a near-room temperature magnetic refrigerator. In *Advances in Cryogenic Engineering*, pages 1759–1766. Springer (1998) .

[18] A. Kitanovski. Energy applications of magnetocaloric materials. *Adv. Energy Mater.* **10** (2020) 1903741. doi:10.1002/aenm.201903741

[19] V. Franco, J. M. Borrego, C. Conde, A. Conde, M. Stoica, and S. Roth. Refrigerant capacity of FeCrMoCuGaPCB amorphous alloys. *J. App. Phys.* **100** (2006) 083903. doi:10.1063/1.2358311

[20] J. D. Bocarsly, E. E. Levin, C. A. Garcia, K. Schwennicke, S. D. Wilson, and R. Seshadri. A simple computational proxy for screening magnetocaloric compounds. *Chem. Mater.* **29** (2017) 1613–1622. doi:10.1021/acs.chemmater.6b04729

[21] C. A. C. Garcia, J. D. Bocarsly, and R. Seshadri. Computational screening of magnetocaloric alloys. *Phys. Rev. Mater.* **4** (2020) 024402. doi:10.1103/PhysRevMaterials.4.024402

[22] Y. M. Oey, J. D. Bocarsly, D. Mann, E. E. Levin, M. Shatruk, and R. Seshadri. Structural changes upon magnetic ordering in magnetocaloric $AlFe_2B_2$. *Appl. Phys. Lett.* **116** (2020) 212403. doi:10.1063/5.0007266

[23] J. D. Bocarsly, E. E. Levin, S. A. Humphrey, T. Faske, W. Donner, S. D. Wilson, and R. Seshadri. Magnetostructural coupling drives magnetocaloric behavior: The case of MnB versus FeB. *Chem. Mater.* **31** (2019) 4873–4881. doi:10.1021/acs.chemmater.9b01476

[24] Y. M. Oey, D. A. Kitchaev, J. D. Bocarsly, E. C. Schueller, J. A. Cooley, and R. Seshadri. Magnetocaloric behavior and magnetic ordering in MnPdGa. *Phys. Rev. Mater.* **5** (2021) 014414. doi:10.1103/PhysRevMaterials.5.014414

[25] A. Chikina, A. Fedorov, D. Bhoi, V. Voroshnin, E. Haubold, Y. Kushnirenko, K. H. Kim, and S. Borisenko. Turning charge-density waves into Cooper pairs. *Quantum Mater.* **5** (2020) 1–5. doi:10.1038/s41535-020-0225-5

[26] M. Takano, T. Shinjo, and T. Takada. On the spin arrangement in "kagome" lattice of antiferromagnetic $KFe_3(OH)_6(SO_4)_2$. *J. Phys. Soc. Japan* **30** (1971) 1049–1053. doi:10.1143/JPSJ.30.1049

[27] K. Lin and D. Tang. Residual entropy of two-dimensional ice on a Kagome lattice. *J. Phys. A Math. Gen.* **9** (1976) 1101. doi:10.1088/0305-4470/9/7/013

[28] W.-S. Wang, Z.-Z. Li, Y.-Y. Xiang, and Q.-H. Wang. Competing electronic orders on kagome lattices at van Hove filling. *Phys. Rev. B* **87** (2013) 115135. doi:10.1103/PhysRevB.87.115135

[29] S. V. Isakov, S. Wessel, R. G. Melko, K. Sengupta, and Y. B. Kim. Hard-Core Bosons on the Kagome Lattice: Valence-Bond Solids and Their Quantum Melting. *Phys. Rev. Lett.* **97** (2006) 147202. doi:10.1103/PhysRevLett.97.147202

[30] A. O'Brien, F. Pollmann, and P. Fulde. Strongly correlated fermions on a kagome lattice. *Phys. Rev. B* **81** (2010) 235115. doi:10.1103/PhysRevB.81.235115

[31] A. Rüegg and G. A. Fiete. Fractionally charged topological point defects on the kagome lattice. *Phys. Rev. B* **83** (2011) 165118. doi:10.1103/PhysRevB.83.165118

[32] S. Yan, D. A. Huse, and S. R. White. Spin-liquid ground state of the S = 1/2 kagome Heisenberg antiferromagnet. *Science* **332** (2011) 1173–1176. doi:10.1126/science.1201080

[33] H.-M. Guo and M. Franz. Topological insulator on the kagome lattice. *Phys. Rev. B* **80** (2009) 113102. doi:10.1103/PhysRevB.80.113102

[34] W.-H. Ko, P. A. Lee, and X.-G. Wen. Doped kagome system as exotic superconductor. *Phys. Rev. B* **79** (2009) 214502. doi:10.1103/PhysRevB.79.214502

[35] S.-L. Yu and J.-X. Li. Chiral superconducting phase and chiral spin–density–wave phase in a Hubbard model on the kagome lattice. *Phys. Rev. B* **85** (2012) 144402. doi:10.1103/PhysRevB.85.144402

[36] M. L. Kiesel, C. Platt, and R. Thomale. Unconventional Fermi surface instabilities in the kagome Hubbard model. *Phys. Rev. Lett.* **110** (2013) 126405. doi:10.1103/PhysRevLett.110.126405

[37] K. Barros, J. W. Venderbos, G.-W. Chern, and C. Batista. Exotic magnetic orderings in the kagome Kondo-lattice model. *Phys. Rev. B* **90** (2014) 245119. doi:10.1103/PhysRevB.90.245119

[38] X. Feng, K. Jiang, Z. Wang, and J. Hu. Chiral flux phase in the Kagome superconductor AV_3Sb_5. *Sci. Bull.* (2021). doi:10.1016/j.scib.2021.04.043

[39] B. R. Ortiz, L. C. Gomes, J. R. Morey, M. Winiarski, M. Bordelon, J. S. Mangum, I. W. Oswald, J. A. Rodriguez-Rivera, J. R. Neilson, S. D. Wilson, , E. Ertekin, T. M. McQueen, and E. S. Toberer. New kagome prototype materials: discovery of KV_3Sb_5, RbV_3Sb_5, and CsV_3Sb_5. *Phys. Rev. Mater.* **3** (2019) 094407. doi:10.1103/PhysRevMaterials.3.094407

[40] Y.-X. Jiang, J.-X. Yin, M. M. Denner, N. Shumiya, B. R. Ortiz, G. Xu, Z. Guguchia, J. He, M. S. Hossain, X. Liu, *et al.* Unconventional chiral charge order in kagome superconductor KV_3Sb_5. *Nat. Mater.* (2021) 1–5. doi:10.1038/s41563-021-01034-y

[41] H. Zhao, H. Li, B. R. Ortiz, S. M. Teicher, T. Park, M. Ye, Z. Wang, L. Balents, S. D. Wilson, and I. Zeljkovic. Cascade of correlated electron states in the kagome superconductor CsV_3Sb_5. *Nature* **599** (2021) 216–221. doi:10.1038/s41586-021-03946-w

[42] B. R. Ortiz, S. M. Teicher, Y. Hu, J. L. Zuo, P. M. Sarte, E. C. Schueller, A. M. Abeykoon, M. J. Krogstad, S. Rosenkranz, R. Osborn, R. Seshadri, L. Balents, J. He, and S. D. Wilson. CsV_3Sb_5: A $\mathbb{Z}_2$ topological kagome metal with a superconducting ground state. *Phys. Rev, Lett.* **125** (2020) 247002. doi:10.1103/PhysRevLett.125.247002

[43] B. R. Ortiz, P. M. Sarte, E. M. Kenney, M. J. Graf, S. M. Teicher, R. Seshadri, and S. D. Wilson. Superconductivity in the $\mathbb{Z}_2$ kagome metal KV_3Sb_5. *Phys. Rev. Mater.* **5** (2021) 034801. doi:10.1103/PhysRevMaterials.5.034801

[44] Z. Liang, X. Hou, F. Zhang, W. Ma, P. Wu, Z. Zhang, F. Yu, J.-J. Ying, K. Jiang, L. Shan, *et al.* Three-dimensional charge density wave and surface-dependent vortex-core states in a kagome superconductor CsV_3Sb_5. *Phys. Rev. X* **11** (2021) 031026. doi:10.1103/PhysRevX.11.031026

[45] H. Chen, H. Yang, B. Hu, Z. Zhao, J. Yuan, Y. Xing, G. Qian, Z. Huang, G. Li, Y. Ye, *et al.* Roton pair density wave in a strong-coupling kagome superconductor. *Nature* **599** (2021) 222–228. doi:10.1038/s41586-021-03983-5

[46] Q. Yin, Z. Tu, C. Gong, Y. Fu, S. Yan, and H. Lei. Superconductivity and normal–state properties of kagome metal RbV_3Sb_5 single crystals. *Chin. Phys. Lett.* **38** (2021) 037403. doi:10.1088/0256-307X/38/3/037403

[47] Y. Fu, N. Zhao, Z. Chen, Q. Yin, Z. Tu, C. Gong, C. Xi, X. Zhu, Y. Sun, K. Liu, *et al.* Quantum transport evidence of topological band structures of kagome superconductor CsV_3Sb_5. *Phys. Rev. Lett.* **127** (2021) 207002. doi:10.1103/PhysRevLett.127.207002

[48] B. R. Ortiz, S. M. Teicher, L. Kautzsch, P. M. Sarte, N. Ratcliff, J. Harter, J. P. Ruff, R. Seshadri, and S. D. Wilson. Fermi surface mapping and the nature of charge density wave order in the kagome superconductor CsV_3Sb_5. *Phys. Rev. X* **11** (2021) 041030. doi:10.1103/PhysRevX.11.041030

[49] E. Uykur, B. R. Ortiz, S. D. Wilson, M. Dressel, and A. A. Tsirlin. Optical detection of the density-wave instability in the kagome metal KV_3Sb_5. *npj Quantum Mater.* **7** (2022) 1–8. doi:10.1038/s41535-021-00420-8

[50] Y. Hu, X. Wu, B. R. Ortiz, X. Han, N. C. Plumb, S. D. Wilson, A. P. Schnyder, and M. Shi. Coexistence of Tri-Hexagonal and Star-of-David pattern in the charge density wave of the kagome superconductor AV_3Sb_5. *arXiv preprint arXiv:2201.06477* (2022).

[51] E. M. Kenney, B. R. Ortiz, C. Wang, S. D. Wilson, and M. J. Graf. Absence of local moments in the kagome metal KV_3Sb_5 as determined by muon spin spectroscopy. *J. Phys. Condens. Matter.* **33** (2021) 235801. doi:10.1088/1361-648X/abe8f9

[52] S.-Y. Yang, Y. Wang, B. R. Ortiz, D. Liu, J. Gayles, E. Derunova, R. Gonzalez-Hernandez, L. Šmejkal, Y. Chen, S. S. Parkin, S. D. Wilson, E. S. Toberer, T. McQueen, and M. N. Ali. Giant, unconventional anomalous Hall effect in the metallic frustrated magnet candidate, KV_3Sb_5. *Sci. Adv.* **6** (2020) abb6003. doi:10.1126/sciadv.abb6003

[53] F. Yu, T. Wu, Z. Wang, B. Lei, W. Zhuo, J. Ying, and X. Chen. Concurrence of anomalous Hall effect and charge density wave in a superconducting topological kagome metal. *Phys. Rev. B* **104** (2021) L041103. doi:10.1103/PhysRevB.104.L041103

[54] F. Du, S. Luo, B. R. Ortiz, Y. Chen, W. Duan, D. Zhang, X. Lu, S. D. Wilson, Y. Song, and H. Yuan. Pressure-induced double superconducting domes and charge instability in the kagome metal KV_3Sb_5. *Phys. Rev. B* **103** (2021) L220504. doi:10.1103/PhysRevB.103.L220504

[55] K. Chen, N. Wang, Q. Yin, Y. Gu, K. Jiang, Z. Tu, C. Gong, Y. Uwatoko, J. Sun, H. Lei, *et al.* Double superconducting dome and triple enhancement of T_C in the kagome superconductor CsV_3Sb_5 under high pressure. *Phys. Rev. Lett.* **126** (2021) 247001. doi:10.1103/PhysRevLett.126.247001

[56] C. Berthier, P. Molinié, and D. Jérome. Evidence for a connection between charge density waves and the pressure enhancement of superconductivity in $2H$-$NbSe_2$. *Solid State Commun.* **18** (1976) 1393–1395. doi:10.1016/0038-1098(76)90986-8

[57] D. Freitas, P. Rodière, M. Osorio, E. Navarro-Moratalla, N. Nemes, V. Tissen, L. Cario, E. Coronado, M. García-Hernández, S. Vieira, *et al.* Strong enhancement of superconductivity at high pressures within the charge-density-wave states of $2H-TaS_2$ and $2H-TaSe_2$. *Phys. Rev. B* **93** (2016) 184512. doi:10.1103/PhysRevB.93.184512

[58] Y. Song, T. Ying, X. Chen, X. Han, X. Wu, A. P. Schnyder, Y. Huang, J.-g. Guo, and X. Chen. Competition of Superconductivity and Charge Density Wave in Selective Oxidized CsV_3Sb_5 Thin Flakes. *Phys. Rev. Lett.* **127** (2021) 237001. doi:10.1103/PhysRevLett.127.237001

[59] E. Morosan, H. W. Zandbergen, B. Dennis, J. Bos, Y. Onose, T. Klimczuk, A. Ramirez, N. Ong, and R. J. Cava. Superconductivity in Cu_xTiSe_2. *Nat. Phys.* **2** (2006) 544–550. doi:10.1038/nphys360

[60] W. Choe, V. K. Pecharsky, A. O. Pecharsky, K. A. Gschneidner, V. G. Young, and G. J. Miller. Making and breaking covalent bonds across the magnetic transition in the giant magnetocaloric material $Ge_5(Si_2Ge_2)$. *Phys. Rev. Lett.* **84** (2000) 4617–4620. doi:10.1103/PhysRevLett.84.4617

[61] M. Annaorazov, K. Asatryan, G. Myalikgulyev, S. Nikitin, A. Tishin, and A. Tyurin. Alloys of the Fe–Rh system as a new class of working material for magnetic refrigerators. *Cryogenics* **32** (1992) 867–872. doi:10.1016/0011-2275(92)90352-B

[62] X. Tan, P. Chai, C. M. Thompson, and M. Shatruk. Magnetocaloric effect in $AlFe_2B_2$: toward magnetic refrigerants from earth-abundant elements. *J. Am. Chem. Soc.* **135** (2013) 9553–9557. doi:10.1021/ja404107p

[63] P. Chai, S. A. Stoian, X. Tan, P. A. Dube, and M. Shatruk. Investigation of magnetic properties and electronic structure of layered-structure borides AlT_2B_2 (T = Fe, Mn, Cr) and $AlFe_{2-x}Mn_xB_2$. *J. Solid State Chem.* **224** (2015) 52–61. doi:10.1016/j.jssc.2014.04.027

[64] S. Hirt, F. Yuan, Y. Mozharivskyj, and H. Hillebrecht. $AlFe_{2-x}Co_xB_2$ (x = 0–0.30): T_C Tuning through Co substitution for a promising magnetocaloric material realized by spark plasma sintering. *Inorg. Chem.* **55** (2016) 9677–9684. doi:10.1021/acs.inorgchem.6b01467

[65] R. Barua, B. Lejeune, B. Jensen, L. Ke, R. McCallum, M. Kramer, and L. Lewis. Enhanced room-temperature magnetocaloric effect and tunable magnetic response in Ga-and Ge-substituted $AlFe_2B_2$. *J. Alloys Compd.* **777** (2019) 1030–1038. doi:10.1016/j.jallcom.2018.10.206

[66] M. Fries, Z. Gercsi, S. Ener, K. P. Skokov, and O. Gutfleisch. Magnetic, magnetocaloric and structural properties of manganese based monoborides doped with iron and cobalt– A candidate for thermomagnetic generators. *Acta Mater.* **113** (2016) 213–220. doi:10.1016/j.actamat.2016.05.005

[67] E. E. Levin, J. D. Bocarsly, K. E. Wyckoff, T. M. Pollock, and R. Seshadri. Tuning the magnetocaloric response in half-Heusler/Heusler $MnNi_{1+x}Sb$ solid solutions. *Phys. Rev. Mater.* **1** (2017) 075003. doi:10.1103/PhysRevMaterials.1.075003

[68] E. E. Levin, J. D. Bocarsly, J. H. Grebenkemper, R. Issa, S. D. Wilson, T. M. Pollock, and R. Seshadri. Structural coupling and magnetic tuning in $Mn_{2-x}Co_xP$ magnetocalorics for thermomagnetic power generation. *APL Mater.* **8** (2020) 041106. doi:10.1063/1.5142000

[69] J. A. Cooley, M. K. Horton, E. E. Levin, S. H. Lapidus, K. A. Persson, and R. Seshadri. From waste-heat recovery to refrigeration: Compositional tuning of magnetocaloric $Mn_{1+x}Sb$. *Chem. Mater.* **32** (2020) 1243–1249. doi:10.1021/acs.chemmater.9b04643

[70] C. P. Bean and D. S. Rodbell. Magnetic disorder as a first-order phase transformation. *Phys. Rev.* **126** (1962) 104–115. doi:10.1103/PhysRev.126.104

[71] A. Davarpanah, J. H. Belo, V. S. Amaral, and J. S. Amaral. On the optimization of magneto-volume coupling for practical applied field magnetic refrigeration. *Phys. status solidi* **256** (2019) 1800419. doi:10.1002/pssb.201800419

[72] V. Franco, J. Y. Law, A. Conde, V. Brabander, D. Y. Karpenkov, I. Radulov, K. Skokov, and O. Gutfleisch. Predicting the tricritical point composition of a series of LaFeSi magnetocaloric alloys via universal scaling. *J. Phys. D. Appl. Phys.* **50** (2017) 414004. doi:10.1088/1361-6463/aa8792

[73] N. H. Dung, L. Zhang, Z. Ou, and E. Brück. From first-order magneto-elastic to magneto-structural transition in $(Mn,Fe)_{1.95}P_{0.50}Si_{0.50}$ compounds. *App. Phys. Lett.* **99** (2011) 092511. doi:10.1063/1.3634016

[74] I. Takeuchi and K. Sandeman. Solid-state cooling with caloric materials. *Phys. Today* **68** (2015) 48. doi:10.1063/PT.3.3022

[75] W. Jeitschko. The crystal structure of Fe_2AlB_2. *Acta Crystallogr. B* **25** (1969) 163–165. doi:10.1107/S0567740869001944

[76] B. Lejeune, D. L. Schlagel, B. Jensen, T. A. Lograsso, M. J. Kramer, and L. Lewis. Effects of Al and Fe solubility on the magnetofunctional properties of $AlFe_2B_2$. *Phys. Rev. Mater.* **3** (2019) 094411. doi:10.1103/PhysRevMaterials.3.094411

[77] A. El Boukili, N. Tahiri, E. Salmani, H. Ez-Zahraouy, M. Hamedoun, A. Benyoussef, M. Balli, and O. Mounkachi. Magnetocaloric and cooling properties of the intermetallic compound $AlFe_2B_2$ in an AMR cycle system. *Intermetallics* **104** (2019) 84–89. doi:10.1016/j.intermet.2018.10.025

[78] J. Elliott, S. Legvold, and F. Spedding. Some magnetic properties of gadolinium metal. *Phys. Rev.* **91** (1953) 28. doi:10.1103/PhysRev.91.28

[79] L. Lewis, R. Barua, and B. Lejeune. Developing magnetofunctionality: Coupled structural and magnetic phase transition in $AlFe_2B_2$. *J. Alloys Compd.* **650** (2015) 482–488. doi:10.1016/j.jallcom.2015.07.255

[80] J. Cedervall, M. S. Andersson, T. Sarkar, E. K. Delczeg-Czirjak, L. Bergqvist, T. C. Hansen, P. Beran, P. Nordblad, and M. Sahlberg. Magnetic structure of the magnetocaloric compound $AlFe_2B_2$. *J. Alloys Compd.* **664** (2016) 784–791. doi:10.1016/j.jallcom.2015.12.111

[81] T. N. Lamichhane, L. Xiang, Q. Lin, T. Pandey, D. S. Parker, T.-H. Kim, L. Zhou, M. J. Kramer, S. L. Bud'ko, and P. C. Canfield. Magnetic properties of single crystalline itinerant ferromagnet $AlFe_2B_2$. *Phys. Rev. Mater.* **2** (2018) 084408. doi:10.1103/PhysRevMaterials.2.084408

[82] B. T. Lejeune, X. Du, R. Barua, J.-C. Zhao, and L. H. Lewis. Anisotropic thermal conductivity of magnetocaloric $AlFe_2B_2$. *Acta Mater.* **1** (2018) 150–154. doi:10.1016/j.mtla.2018.05.011

[83] T. Ali, M. Khan, E. Ahmed, and A. Ali. Phase analysis of $AlFe_2B_2$ by synchrotron X-ray diffraction, magnetic and Mössbauer studies. *Prog. Nat. Sci. Mater.* **27** (2017) 251–256. doi:10.1016/j.pnsc.2017.03.007

[84] J. D. Bocarsly, R. F. Need, R. Seshadri, and S. D. Wilson. Magnetoentropic signatures of skyrmionic phase behavior in FeGe. *Phys. Rev. B* **97** (2018) 100404. doi:10.1103/PhysRevB.97.100404

[85] A. A. Coelho. TOPAS and TOPAS-Academic: An optimization program integrating computer algebra and crystallographic objects written in C++. *J. Appl. Crystallogr.* **51** (2018) 210–218. doi:10.1107/S1600576718000183

[86] G. W. Stinton and J. S. Evans. Parametric Rietveld refinement. *J. Appl. Crystallogr.* **40** (2007) 87–95. doi:10.1107/S0021889806043275

[87] K. Momma and F. Izumi. VESTA 3 for three-dimensional visualization of crystal, volumetric and morphology data. *J. Appl. Crystallogr.* **44** (2011) 1272–1276. doi:10.1107/S0021889811038970

[88] R. Barua, B. Lejeune, L. Ke, G. Hadjipanayis, E. M. Levin, R. McCallum, M. Kramer, and L. Lewis. Anisotropic magnetocaloric response in $AlFe_2B_2$. *J. Alloys Compd.* **745** (2018) 505–512. doi:10.1016/j.jallcom.2018.02.205

[89] P. W. Stephens. Phenomenological model of anisotropic peak broadening in powder diffraction. *J. Appl. Crystallogr.* **32** (1999) 281–289. doi:10.1107/S0021889898006001

[90] D. Mondal, C. Kamal, S. Banik, A. Bhakar, A. Kak, G. Das, V. Reddy, A. Chakrabarti, and T. Ganguli. Structural and electronic properties of $Fe(Al_xGa_{1-x})_3$ system. *J. Appl. Phys.* **120** (2016) 165102. doi:10.1063/1.4965718

[91] M. van Schilfgaarde, I. Abrikosov, and B. Johansson. Origin of the Invar effect in iron–nickel alloys. *Nature* **400** (1999) 46–49. doi:10.1038/21848

[92] J. A. Cooley, J. D. Bocarsly, E. C. Schueller, E. E. Levin, E. E. Rodriguez, A. Huq, S. H. Lapidus, S. D. Wilson, and R. Seshadri. Evolution of non-collinear magnetism in magnetocaloric MnPtGa. *Phys. Rev. Mater.* **4** (2020) 044405. doi:10.1103/PhysRevMaterials.4.044405

[93] K. P. Belov, Y. V. Ergin, and A. A. Ped'ko. Magnetostriction of a Gadolinium single crystal. *J. Exptl. Theor. Phys.* **22** (1966) 414–419.

[94] H. Shiraishi, T. Hori, N. Ohkubo, K. Ohoyama, and Y. Yamaguchi. Magnetic and neutron diffraction study on Ni_2In type $(Mn_{1-x}Pd_x)_2Ga$. *J. Appl. Phys.* **93** (2003) 6996–6998. doi:10.1063/1.1556254

[95] X. Xiao, L. Peng, X. Zhao, Y. Zhang, Y. Dai, J. Guo, M. Tong, J. Li, B. Li, W. Liu, J. Cai, B. Shen, and Z. Zhang. Low-field formation of room-temperature biskyrmions in centrosymmetric MnPdGa magnet. *Appl. Phys. Lett.* **114** (2019) 142404. doi:10.1063/1.5089609

[96] G. Kresse and J. Furthmüller. Efficient iterative schemes for ab initio total-energy calculations using a plane-wave basis set. *Phys. Rev. B* **54** (1996) 11169. doi:10.1103/PhysRevB.54.11169

[97] P. E. Blöchl. Projector augmented-wave method. *Phys. Rev. B* **50** (1994) 17953. doi:10.1103/PhysRevB.50.17953

[98] G. Kresse and D. Joubert. From ultrasoft pseudopotentials to the projector augmented-wave method. *Phys. Rev. B* **59** (1999) 1758. doi:10.1103/PhysRevB.59.1758

[99] J. P. Perdew, K. Burke, and M. Ernzerhof. Generalized gradient approximation made simple. *Phys. Rev. Lett.* **77** (1996) 3865–3868.

[100] A. K. Srivastava, P. Devi, A. K. Sharma, T. Ma, H. Deniz, H. L. Meyerheim, C. Felser, and S. S. P. Parkin. Observation of Robust Néel Skyrmions in Metallic PtMnGa. *Adv. Mater.* **32** (2020) 1904327. doi:10.1002/adma.201904327

[101] K. Buschow and P. van Engen. Note on the magnetic and magneto-optical properties of Ni_2In type 3d transition metal compounds. *Phys. Status Solidi A* **76** (1983) 615–620. doi:10.1002/pssa.2210760225

[102] D. A. Kitchaev, I. J. Beyerlein, and A. Van der Ven. Phenomenology of chiral Dzyaloshinskii-Moriya interactions in strained materials. *Phys. Rev. B* **98** (2018) 214414. doi:10.1103/PhysRevB.98.214414

[103] E. C. Schueller, D. A. Kitchaev, J. L. Zuo, J. D. Bocarsly, J. A. Cooley, A. Van der Ven, S. D. Wilson, and R. Seshadri. Structural evolution and skyrmionic phase diagram of the lacunar spinel $GaMo_4Se_8$. *Phys. Rev. Mater.* **4** (2020) 064402. doi:10.1103/PhysRevMaterials.4.064402

[104] I. Mazin and M. Johannes. A key role for unusual spin dynamics in ferropnictides. *Nat. Phys.* **5** (2009) 141–145. doi:10.1038/nphys1160

[105] H. LaBollita and A. S. Botana. Tuning the Van Hove singularities in AV_3Sb_5 (A= K, Rb, Cs) via pressure and doping. *Phys. Rev. B* **104** (2021) 205129. doi:10.1103/PhysRevB.104.205129

[106] Y. M. Oey, B. R. Ortiz, F. Kaboudvand, J. Frassineti, E. Garcia, S. Sanna, V. Mitrović, R. Seshadri, and S. D. Wilson. Fermi level tuning and double-dome superconductivity in the kagome metals $CsV_3Sb_{5-x}Sn_x$. *Phys. Rev. Mater.* **6** (2022). doi:10.1103/PhysRevMaterials.6.L041801

[107] C. Zhu, X. Yang, W. Xia, Q. Yin, L. Wang, C. Zhao, D. Dai, C. Tu, B. Song, Z. Tao, *et al.* Double-dome superconductivity under pressure in the V-based kagome metals AV_3Sb_5 (A = Rb and K). *Phys. Rev. B* **105** (2022) 094507. doi:10.1103/PhysRevB.105.094507

[108] A. Abragam. *The principles of nuclear magnetism*. 32. Oxford University Press (1961).

[109] G. Kresse and J. Furthmüller. Efficiency of ab-initio total energy calculations for metals and semiconductors using a plane-wave basis set. *Comput. Mater. Sci.* **6** (1996) 15–50. doi:10.1016/0927-0256(96)00008-0

[110] W. Setyawan and S. Curtarolo. High-throughput electronic band structure calculations: Challenges and tools. *Comp. Mater. Sci.* **49** (2010) 299–312. doi:10.1016/j.commatsci.2010.05.010

[111] A. M. Ganose, A. J. Jackson, and D. O. Scanlon. sumo: Command-line tools for plotting and analysis of periodic *ab initio* calculations. *J. Open Source Softw.* **3** (2018) 717. doi:10.21105/joss.00717

[112] A. Tsirlin, P. Fertey, B. R. Ortiz, B. Klis, V. Merkl, M. Dressel, S. Wilson, and E. Uykur. Role of Sb in the superconducting kagome metal CsV_3Sb_5 revealed by its anisotropic compression. *SciPost Physics* **12** (2022) 049. doi:10.21468/SciPostPhys.12.2.049

[113] E. Uykur, B. Ortiz, O. Iakutkina, M. Wenzel, S. Wilson, M. Dressel, and A. Tsirlin. Low-energy optical properties of the nonmagnetic kagome metal CsV_3Sb_5. *Phys. Rev. B* **104** (2021) 045130. doi:10.1103/PhysRevB.104.045130

[114] M. Kang, S. Fang, J. Yoo, B. R. Ortiz, Y. M. Oey, J. Choi, S. H. Ryu, J. Kim, C. Jozwiak, A. Bostwick, E. Rotenberg, E. Kaxiras, J. G. Checkelsky, S. D. Wilson, J.-H. Park, and R. Comin. Charge order landscape and competition with superconductivity in kagome metals. *arXiv preprint arXiv:2202.01902* (2022). Accepted to Nat. Mater.

[115] M. H. Christensen, T. Birol, B. M. Andersen, and R. M. Fernandes. Theory of the charge density wave in AV_3Sb_5 kagome metals. *Phys. Rev. B* **104** (2021) 214513. doi:10.1103/PhysRevB.104.214513

[116] T. Ohtani, S. Onoue, and M. Nakahira. Phase relationships and properties in the V–Te system. *Mater. Res. Bull.* **19** (1984) 1367–1375. doi:10.1016/0025-5408(84)90202-2

[117] M. Khabachev and K. Chuntonov. Phase diagram of the system K-Te. *J. Alloys Compd.* **265** (1998) 93–95. doi:10.1016/S0925-8388(97)00314-9

[118] J. Li, H.-Y. Guo, D. M. Proserpio, and A. Sironi. Exploring tellurides: synthesis and characterization of new binary, ternary, and quaternary compounds. *J Solid State Chem.* **117** (1995) 247–255. doi:10.1006/jssc.1995.1270

[119] C.-H. Leung and L. H. Van Vlack. Solubility limits in binary (Ca, Mn) chalcogenides. *J. Am. Ceram.* **62** (1979) 613–616. doi:10.1111/j.1151-2916.1979.tb12743.x

[120] L. Kautzsch, Y. M. Oey, H. Li, Z. Ren, B. R. Ortiz, R. Seshadri, J. Ruff, Z. Wang, I. Zeljkovic, and S. D. Wilson. Incommensurate charge-stripe correlations in the kagome superconductor $CsV_3Sb_{5-x}Sn_x$. *arXiv preprint arXiv:2207.10608* (2022).

[121] Y. Yang, W. Fan, Q. Zhang, Z. Chen, X. Chen, T. Ying, X. Wu, X. Yang, F. Meng, G. Li, S. Li, L. Gu, T. Qian, A. P. Schnyder, J.-g. Guo, and X. Chen. Discovery of two families of VSb–based compounds with V–kagome lattice. *Chin. Phys. Lett.* **38** (2021) 127102. doi:10.1088/0256-307X/38/12/127102